

DISSERTATION

Titel der Dissertation

Strain localization in a calcite marble and its isotopic and mechanical impact. Insights from a natural experiment at varying geological strain rates (Syros, Greece).

Verfasserin

Anna Rogowitz, MSc. BSc.

angestrebter akademischer Grad

Doktorin der Naturwissenschaften (Dr. rer. nat.)

Wien, 2015

Studienkennzahl lt. Studienblatt:

A 796 605 426

Dissertationsgebiet lt. Studienblatt:

Erdwissenschaften

Betreuer:

Univ.-Prof. Dr. Bernhard Grasemann

Summary

The influence of strain localization on mechanical, chemical and isotopic behaviours of monomineralic rocks has been the focus of many experimental and numerical studies in a wide range of strain, strain rate, pressure and temperature conditions. Comparison between the natural and experimental microstructures is used for inferring the conditions of deformation and the localization processes active in natural shear zones. Additionally, calibrations determined at laboratory conditions can be applied to highly strained rocks deformed under natural conditions in order to estimate natural strain rates and stress. Extrapolation from laboratory conditions to natural conditions, however, remains uncertain, because of the large differences between experimental and natural strain rates.

In this Ph.D. thesis, observations from an almost pure calcite marble layer deformed at lower greenschist facies conditions from Syros Island (Cyclades, Greece) are presented. Syros, being part of the Cycladic-Blueschist unit has been affected by two main metamorphic events: Eocene high-pressure—low-temperature imprint in the blueschist and eclogite facies (M1) followed by Miocene reequilibration in the greenschist-facies event (M2). In the investigated outcrop both tectonometamorphic events can be identified. Coarse grained marble and high-temperature deformation of quartz and dolomite layers showing top-to-the-west shearing are the result of M1 metamorphism, while low-temperature deformation of calcite showing dominant top-to-the-east shearing is associated with M2 metamorphism. The study focuses on one flanking structure (i.e. shear zone) that developed due to the rotation of a crack during M2 top-to-the-east shearing at lower greenschist-facies conditions. The shear zone is characterized by a strain gradient from the slightly deformed tips ($\gamma \sim 50$) to the highly strained centre (γ up to 1000) while the host rock is moderately deformed ($\gamma \sim 3$). During the shear zone development, the strain gradient coincided with a strain rate gradient with strain rate varying from 10^{-13} to 10^{-9} s^{-1} . The studied outcrop thus represents the final state of a natural experiment and gives us a great opportunity to get natural constraints on strain rate dependent mechanical behaviour in a calcite marble. Additionally the presence of minor white mica, within the host rock and shear zone,

allows us to study the influence of deformation under various strain rates on the behaviour of the K/Ar isotopic system.

Detailed microstructural analyses have been performed via optical microscopy, electron microscopy and electron backscatter diffraction mapping, on samples from the highly strained shear zone and the host rock. The analyses show that the calcite microfabric varies depending on position within the shear zone, indicating activation of different deformation and recrystallization mechanisms at different strain rates. Up to strain rates of $\sim 10^{-10} \text{ s}^{-1}$ the marble deformed exclusively within the dislocation creep field, showing a change in recrystallization mechanism and dominant active slip system. While the marble preferentially recrystallized by grain boundary migration at relatively low strain rates ($\sim 10^{-13} \text{ s}^{-1}$), subgrain rotation recrystallization seems to be the dominant mechanism at higher strain rates ($\sim 10^{-12}$ to 10^{-10} s^{-1}). At higher strain rates ($\sim 10^{-9} \text{ s}^{-1}$), the recrystallization mechanism is bulging, resulting in the development of an extremely fine grained ultramylonite (average grain size $\sim 3 \text{ }\mu\text{m}$) accompanied by a switch in deformation mechanism from dislocation creep to grain size sensitive grain boundary sliding. Additional transmission electron microscopy analysis on the extremely fine grained ultramylonite revealed high dislocation densities ($\sim 10^{13} \text{ m}^{-2}$) in the calcite grains indicating that deformation by grain boundary sliding was assisted by dislocation activity. Deformation by grain boundary sliding accommodated by dislocation activity resulted in a strain of ~ 1000 and therefore seems to be of great importance for localization by ductile deformation in calcite rocks even at low temperature ($300 \text{ }^{\circ}\text{C}$) and large strain rate. The investigated samples allowed us to test the consistency of experimental and theoretical calibrations (flow laws, paleowattmeter, paleopiezometer, dislocation density-flow stress relations) for marble at lower greenschist-facies conditions up to strain rates of 10^{-9} s^{-1} , closing the gap between experimental and natural geological strain rates.

In order to date the M2 deformation, step-heating $^{40}\text{Ar}/^{39}\text{Ar}$ geochronology was performed on white mica from the host rock and the shear zone. The analyses resulted in indistinguishable ages of ca. 40 Ma consistent with the Eocene high-grade M1 event. The preservation of the older Eocene age indicates that no resetting of the isotopic K/Ar system during high strain rate deformation of the marble occurred. This is consistent

with the observation of strain partitioning, preserving the mica from recrystallization and the identical homogeneous chemical composition of the mica in both the host rock and the shear zone. Strain localization therefore does not necessarily induce significant disturbance of the isotopic K/Ar system in marbles at lower greenschist-facies conditions, even if both strain and strain rate were high.

This study presents new findings on the deformation behaviour of calcite marble resulting in major weakening and strain localization by grain boundary sliding accommodated by dislocation activity, at conditions, at which we would normally expect brittle behaviour. It gives thus important implications on strain localization in calcite bearing rocks, helping to understand large scale processes as major thrusts and detachments above metamorphic core complexes better.

Zusammenfassung

Die Auswirkungen von lokalisierter Deformation auf das mechanische, chemische und Isotopen Verhalten von monomineralischen Gesteinen, waren der Fokus von zahlreichen experimentellen und numerischen Studien. Deformationsbedingungen sowie Prozesse, die zu der Lokalisierung von Deformation in Scherzonen führen, werden oftmals durch den Vergleich zwischen natürlichen und experimentell entstandenen Mikrostrukturen bestimmt. Darüber hinaus können Verformungsraten mit Hilfe von experimentell bestimmten Kalibrierungen ermittelt werden. Aufgrund des extremen Unterschiedes zwischen natürlichen und experimentellen Verformungsraten, ist eine solche Extrapolation jedoch nicht einfach und kann mit Ungenauigkeiten verbunden sein.

In dieser Arbeit werden Beobachtungen von einem, unter grünschieferfaziellen Bedingungen, deformierten reinem Kalzit-Marmor von Syros (Kykladen, Griechenland) vorgestellt. Die Geologie der Kykladen wurde von zwei metamorphen Episoden beeinflusst: einem eozänem blau- bis eklogit-schieferfaziellen Event (M1), gefolgt von einer grünschieferfaziellen Überprägung (M2). In dem untersuchten Aufschluss können beide tektono-metamorphen Episoden eindeutig identifiziert werden. Grobkörniger Marmor sowie Quarz- und Dolomit-Lagen die unter hohen Temperaturen verformt wurden, zeigen bevorzugte top-to-the-west Scherung (M1), während Kalzite, die bei niedrigeren Temperaturen verformt wurden top-to-the-east Scherung aufweisen. Der Fokus dieser Arbeit liegt auf der Untersuchung einer flanking structure (i.e. Scherzone), welche durch die Rotation eines Risses unter top-to-the-east Scherung (M2) entstanden ist. Die Scherzone weist einen Deformationsgradienten von den gering deformierten enden ($\gamma \sim 50$) bis zum stark deformierten Zentrum (γ bis zu 1000) auf, während der Host Rock nur mäßig deformiert wurde ($\gamma \sim 3$). Während der Entstehung der Scherzone, stimmt der Deformationsgradient mit einem Gradienten in der Verformungsrate zwischen 10^{-13} und 10^{-9} s^{-1} überein. Der untersuchte Aufschluss repräsentiert somit das Ergebnis eines natürlichen Experiments und gibt uns die Möglichkeit, das Verformungsraten abhängige Deformationsverhalten von Kalzit-Marmor, unter natürlichen Bedingungen zu studieren. Des Weiteren gibt uns akzessorisch auftretender

Hellglimmer die Möglichkeit Auswirkungen von lokalisierter Deformation auf das K/Ar-System zu testen.

Detaillierte mikrostruktur Analysen wurden mittels optischer Mikroskopie, Elektronenmikroskopie und electron backscatter diffraction mapping an Proben aus der stark deformierten Scherzone sowie dem Host Rock durchgeführt. Die Analysen zeigen dass die Mikrostruktur abhängig von der Lage innerhalb der Scherzone variiert. Dies deutet darauf hin, dass unterschiedliche Deformations- und Rekristallisations-Mechanismen bei unterschiedlichen Verformungsraten aktiv sind. Bis zu Verformungsraten von $\sim 10^{-10} \text{ s}^{-1}$, deformiert der Marmor ausschließlich durch Versetzungskriechen, unter der Aktivierung von unterschiedlichen dominanten Rekristallisations-Mechanismen und Gleitsystemen. Bei eher geringen Verformungsraten von $\sim 10^{-13} \text{ s}^{-1}$ rekristallisiert der Marmor bevorzugt durch grain boundary migration, während bei höheren Verformungsraten ($\sim 10^{-12} \text{ s}^{-1}$ bis 10^{-10} s^{-1}) subgrain rotation der dominante Rekristallisations-Mechanismus zu sein scheint. Bei höheren verformungsraten ist bulging aktiv, was zu der Ausbildung eines extrem feinkörnigen Ultramylonites führt ($\sim 3 \text{ }\mu\text{m}$), begleitet von einem Wechsel im aktiven Deformations-Mechanismus von Versetzungskriechen zu korngößenabhängigen grain boundary sliding. Zusätzlich durchgeführte Analysen mittels transmissions Elektron Mikroskopie, zeigen eine hohe versetzungsdichte (10^{13} m^{-2}) in den Kalzitkörnern an, was darauf hindeutet dass grain boundary sliding durch Versetzungskriechen unterstützt wurde. Deformation durch die Kombination von grain boundary sliding und versetzungskriechen führte zu einer Verformung von bis zu ~ 1000 und scheint somit von großer Bedeutung für die Lokalisierung von Deformation unter duktilen Bedingungen in Kalzit zu sein. Die untersuchten Proben erlaubten uns die Beständigkeit von experimentellen und theoretischen Kalibrierungen für Marmor unter grünschieferfaziellen Bedingungen und Verformungsraten von bis zu 10^{-9} s^{-1} zu testen (flow laws, paleowattmeter, paleopiezometer, Beziehung zwischen Versetzungsdichte-flow stress).

Um M2 Deformation zu datieren wurde step-heated $^{40}\text{Ar}/^{39}\text{Ar}$ Geochronologie an hellglimmern aus dem Host Rock und der Scherzone durchgeführt. Die Analysen resultierten in ununterscheidbaren Altern von ca. 40 Ma, konsistent mit dem eozänem M1 Event. Die Erhaltung des älteren eozänen Alters deutet darauf hin, dass das K/Ar

System während der Verformung des Marmors nicht zurückgesetzt wurde, konsistent mit der Beobachtung von strain partitioning zwischen Kalzit und Glimmer, welche die Glimmer davor bewahrte zu rekristallisieren. Die Lokalisierung von Deformation in Marmor unter grünschieferfaziellen Bedingungen, führt somit nicht notwendigerweise zu signifikanter Beeinträchtigung des K/Ar Systems, sogar wenn die Verformung und die Verformungsraten sehr hoch waren.

Diese Arbeit präsentiert neue Erkenntnisse über das deformationsverhalten von Kalzit-Marmor, resultierend in extremer Schwächung des Gesteins, und somit der Lokalisierung von Deformation durch eine Kombination von grain boundary sliding und Versetzungskriechen, unter Bedingungen bei welchen wir normalerweise spröde Deformation erwarten würden. Diese Beobachtungen helfen somit großräumige Prozesse wie Störungen und Detachements über metamorphen Kernkomplexen zu verstehen.

Contents

1. Introduction	1
1.1. Mechanisms associated with strain localization	1
1.2. The role of calcite in the crust	4
1.3. Importance of natural experiments	6
1.4. Geology of Syros (Cyclades)	8
1.5. Organization of the thesis	9
2. Strain rate dependent calcite microfabric evolution – an experiment carried out by nature	11
2.1. Introduction	13
2.2. Geological setting	15
2.3. Material and Methods	18
2.3.1. Outcrop description	18
2.3.2. Sample preparation	21
2.3.3. Microstructure analysis	21
2.3.4. Texture analysis	22
2.4. Results	23
2.4.1. Marble microfabric in low-strain domain	24
2.4.2. Marble microfabric in intermediate-strain domain	27
2.4.3. Marble microfabric in high-strain domain	30
2.5. Discussion	33
2.5.1. Relative timing of microstructure development	33

2.5.2. Strain-rate dependent calcite deformation and recrystallization mechanisms	34
2.5.3. Comparison with experimental calibrations	38
2.6. Conclusion	41
A2 Appendix	43
3. Strain localization in ultramylonitic marbles by dislocation activity accommodated grain boundary sliding (Syros, Greece)	49
3.1. Introduction	51
3.2. Geological setting and Outcrop description	52
3.3. Methods	53
3.3.1. Sample preparation	53
3.3.2. Microfabric analysis	54
3.3.3. Dislocation density estimation	55
3.3.4. Stress calculation	55
3.4. Results	56
3.4.1. Microfabric	56
3.4.2. Dislocation microstructure	60
3.4.3. Stress and strain rate calculation	63
3.5. Discussion	66
3.5.1. Grain size reduction	66
3.5.2. Deformation mechanism	66
3.5.3. Cavitation process	68

3.5.4. Comparison of different stress calculations	69
3.6. Conclusion	70
A3 Appendix	72
4. $^{40}\text{Ar}/^{39}\text{Ar}$ mica ages from marble mylonites: a cautionary tale	73
4.1. Introduction	75
4.2. Geological setting and Outcrop description	76
4.3. Results	78
4.4. Discussion	83
4.5. Conclusion	86
A4 Appendix	87
5. Synthesis	91
References	93
Acknowledgments	107
Curriculum vitae	109

1. Introduction

1.1 Mechanisms associated with strain localization

Strain localization can be observed to occur through the entire lithosphere ranging in size from micro- to kilo-metres scales. The development of localized zones is essential for plate tectonics, mountain building and subduction zones. In order to understand earth tectonics it is thus extremely important to understand processes resulting in strain localization. Strain can localize in a brittle or ductile manner depending on rheological parameters and strain rates. While brittle deformation is usually caused by failure of the rock and the reduction of the frictional coefficient, ductile deformation occurs on a very small scale by the motion of defects through the crystal. Deformation in the ductile regime is generally assumed to be homogeneous; being more resistant against ductile deformation with increasing strain and strain rate, therefore the localization of strain requires a local structural or rheological change, causing a local drop in strength. This weakening can be caused by various processes which are explained in the following (Fig.1.1; Burlini and Bruhn, 2005).

Shear heating is assumed to be an important weakening mechanism at greater depths and hence higher temperatures. It is caused by the transformation of inelastic deformational work into thermal energy (Thielmann and Kaus, 2012). The high strain rate deformation in narrow zones can thus result in a local change in temperature what can increase the activity of dislocation creep and therefore decreases the strength of the rock, depending on its mineralogy, or cause partial melting resulting in weakening (Brun and Cobbold, 1980; Mair and Marone, 2000; Kaus and Podladchikov, 2006; Hartz and Podladchikov, 2008).

Local fluid infiltration or the release of incorporated hydrogen from mineral structures may result in hydrolytic-weakening (Griggs, 1967; Jones, 1975) or enhance metamorphic reaction processes resulting in the formation of weaker reaction products; and thus reduce the strength of the bulk rock (Fig.1.1a; Brodie and Rutter, 1987; Stünitz and Tullis, 2001; Faulkner et al., 2010; Grasemann and Tschegg, 2012). In fault zones the infiltration of fluids can affect the pore-fluid pressure resulting in a reduced fracture

strength and preferential deformation by brittle deformation (Sibson, 2000; Faulkner et al., 2010).

The strength of polymineralic rocks depends mainly on the strength of the single constituents and the rock fabric. While in a homogeneously distributed fabric the rock strength is dominated by the strongest mineral, the strength of rocks having a layered fabric is dominated by the strength of the weakest mineral (Handy 1990; Montési, 2007). Layer development can occur due to rotation, shearing and dissolution precipitation creep or occur due to a pre-existing sedimentary sequence (Handy, 1990; Ji et al., 2004; Delle Piane et al, 2009). During progressive deformation parallel to the layering strain tends to accommodate in the weaker interconnected layer resulting in localization.

Strain localization is often associated with the presence of heterogeneities, having a different competence than the surrounding matrix like cracks, veins or porphyroclasts. Such heterogeneities influence the stress field in the surrounding area resulting in inhomogeneous plastic flow and possible weakening (Fig.1.1b, c; Kenkmann and Dresen, 1998; Grasemann et al., 2005; Pennacchioni, 2005; Bestmann et al., 2006).

Due to plastic deformation within the dislocation creep field the development of new strain free, softer grains by recrystallization processes can result in minor strain softening (Tullis and Yund, 1985). The development of a crystallographic preferred orientation (CPO) usually results in a preferred alignment of the easy slip system with respect to the stretching lineation and therefore the overall macroscopic shear, causing minor softening (Poirier, 1980; Schmid et al., 1987; Pieri et al., 2001; Barnhoorn et al., 2004).

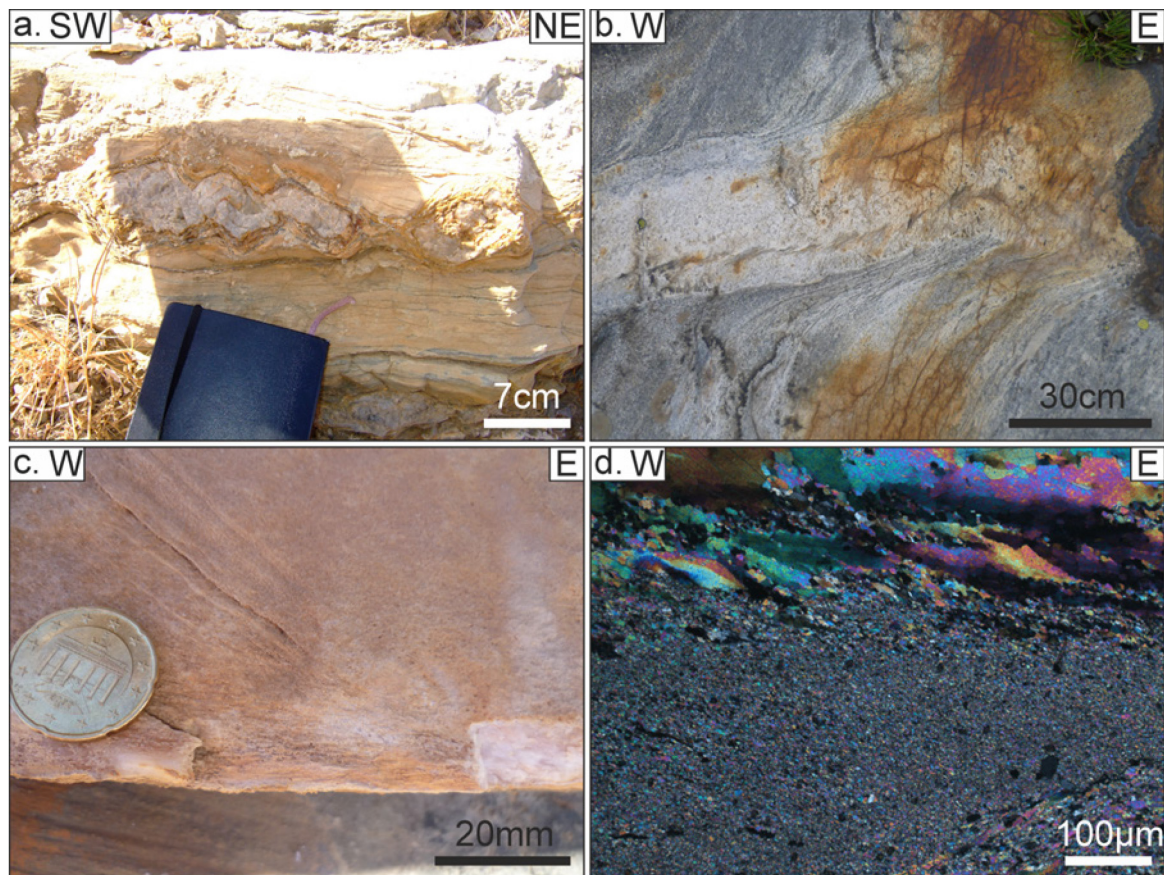


Figure 1.1

Images showing examples of strain localization enhanced by mineral reactions (a), due to the presence of a heterogeneity (b, c), and by grain size reduction resulting in a switch in deformation mechanism (d). a. Quartz boudin in a dolomite-calcite host rock showing a reaction rim of talc (UTM35 4113561N 271865E; Serifos, Cyclades). b. Shear zone bordering an apatite dyke embedded in a weaker orthogneiss (UTM32 713761N 5211747E; Zillertal Alps, South Tyrol) . c. Shear zone in calcite marble localized next to a brittle precursor (UTM35 414840N 313839E; Syros, Cyclades). d. Optical micrograph (crossed polarizer) showing a thin section across the shear zone in c. Note the extreme grain size reduction.

One important observation while looking at shear and fault zones, is the smaller grain size when compared to the surrounding host rock. This leads to the interpretation that one of the most important processes in localizing strain is related to grain size reduction by cataclasis or recrystallization, accompanied by the activation of grain size sensitive deformation mechanisms (Fig.1.1d, Fig.1.2; Schmid et al., 1987; Rutter, 1995; Ulrich et al., 2002; Drury, 2005; Platt and Behr, 2011).

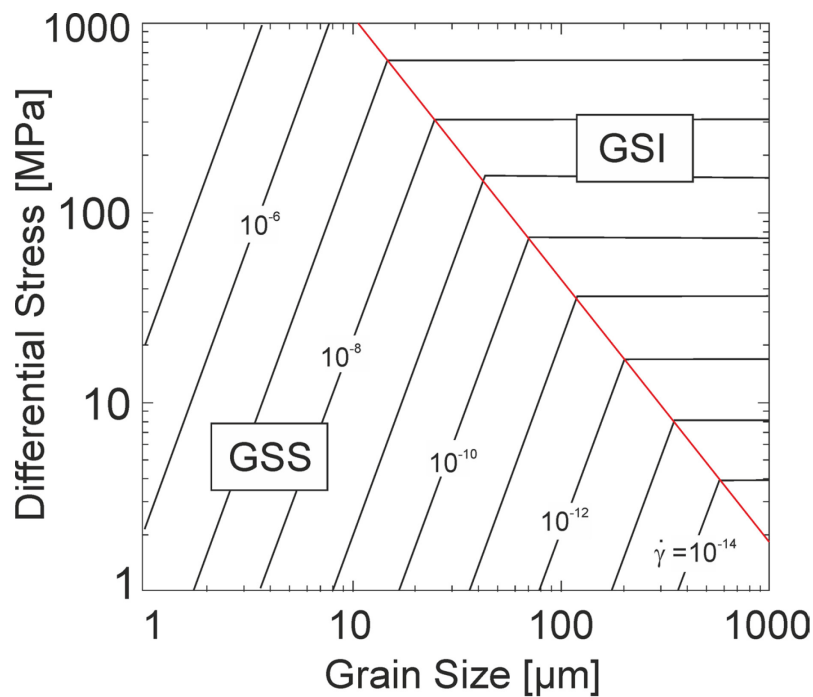


Figure 1.2

Grain-size vs. differential-stress deformation mechanism map for olivine at 1000 °C showing the extreme drop in strength with change in deformation mechanism from grain size insensitive (GSI) to grain size sensitive (GSS) creep due to a decrease in grain size (modified after Platt and Behr, 2011).

This work focuses on a couple of the above mentioned processes. Deformation starts to localize due to the presence of a heterogeneity (i.e. crack), resulting in deformation within the dislocation creep field and the development of a CPO. Due to recrystallization processes smaller grains develop causing a switch in deformation mechanism from grain size insensitive to grain size sensitive creep which is accompanied by extreme strain localization.

1.2 The role of calcite in the crust

Calcite is beside quartz one of the most important minerals in the crust (Fig.1.3). Calcite is an important rock forming mineral, being the principal constituent of carbonitic rocks. Carbonates mainly accumulate by precipitation in marine environment or form from skeletons and housings of marine organisms like snails, shells, sea urchins, sponges or carbonate reefs (Flügel, 2010). Due to the preferred location of precipitation in marine

basins, they are often incorporated into convergence zone (collision and subduction) and metamorphosed to marble which are later on subsequently deformed during orogenic processes.

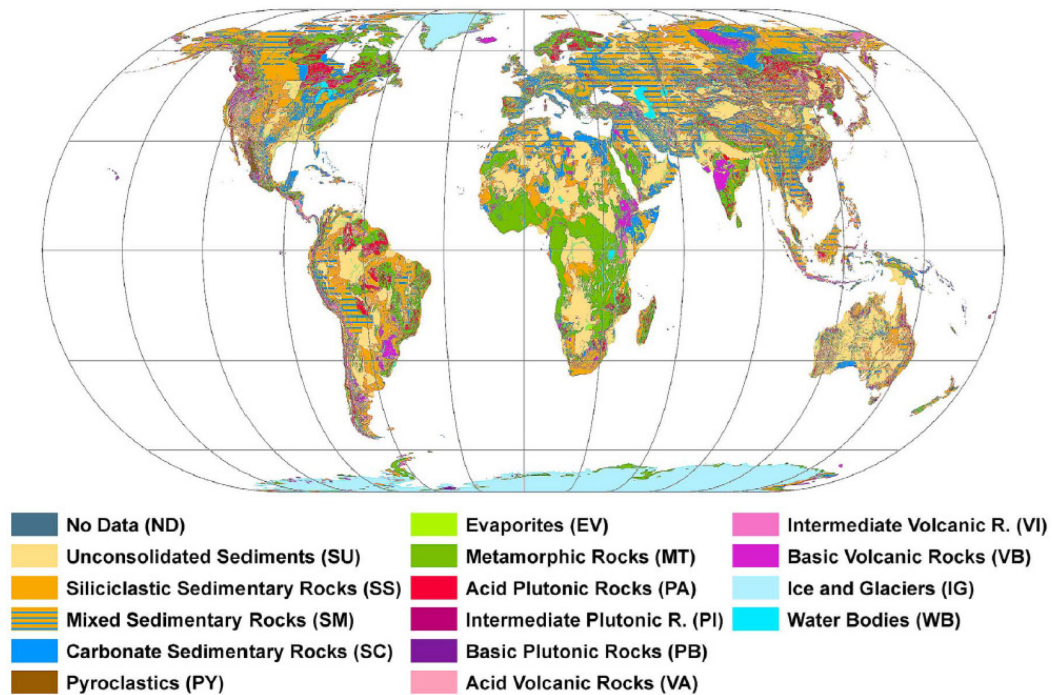


Figure 1.3

Lithological map based on the database GLiM (Hartmann and Moosdorf, 2012).

The relatively low strength of limestone and marble, especially when compared to quartz or feldspar rich lithologies, makes them appropriate for strain localization in orogenic belts. Therefore calcite rich lithologies are often associated with shear zone formation (Van Der Pluum, 1991; Busch and Van Der Pluum, 1995; Fernández et al., 2004; Romeo et al., 2007). The great importance of calcite in orogenic processes is the reason why it is one of the best studied minerals in rock deformation. Due to the low activation temperature for crystal plasticity of around 180 °C (Burkhard, 1990) calcite deforms even at low temperatures ductile, what makes it important to understand the mechanisms resulting in strain localization at low temperatures and geological relevant strain rates (Fig.1.4).

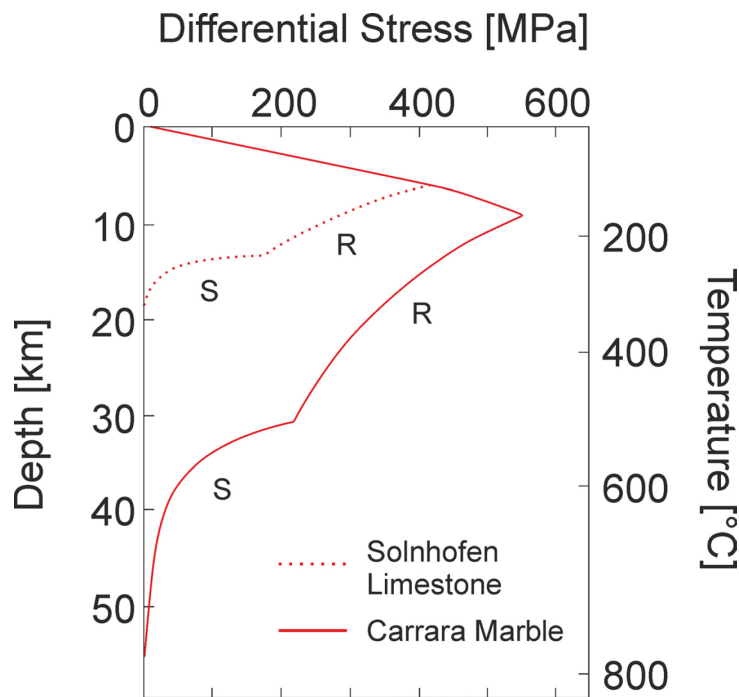


Figure 1.4

Strength-depth diagram for dry calcite deformed at strain rates of 10^{-15} s^{-1} . Used flow laws are by Rutter (R; 1995) for dislocation creep and Schmid et al., (S; 1977) for diffusion creep (modified after Kohlstedt et al., 1995).

1.3 Importance of natural experiments

The mechanical behaviour of calcite single crystals, limestone and marble has been focus of a large number of experimental studies (Schmid et al., 1980, 1987; Rutter, 1995; De Bresser and Spiers, 1990, 1997; Pieri et al., 2001; Barnhoorn et al., 2004; Barber et al., 2007; Liteanu et al., 2012; Rybacki et al., 2013). Paleowatt- and paleopiezometer linking deformation grain size and differential stress have been determined on the base of experimental studies (Schmid, 1980; Rutter, 1995; Austin and Evans, 2009) as well as different flow laws for grain size sensitive and grain size insensitive creep (De Bresser et al., 2002; Renner et al., 2002; Herwegh et al., 2003). The great control of temperature, stress, strain and strain rate conditions in the laboratory gives us the opportunity to link observed microfabrics, resulting from activation of different recrystallization and deformation mechanisms, to certain deformation conditions. Therefore experiments are an essential tool for understanding the rheological behaviour of rocks that allow us to characterize the rheological effect of the above mentioned mechanisms (1.1), associated

with strain localization. Nevertheless experiments are simplified compared to nature. Possible pre-existing fabrics and fluid rock interaction resulting in mineral reactions are usually neglected. Additionally laboratories are restricted in their P-T conditions and the analysing sample size. Especially in terms of strain rate the conditions in laboratories are far from nature (Fig.1.5). It is therefore challenging to understand the mechanisms resulting in complex fault systems and km long, localized shear zones by analysing rock samples in the order of cm in size. In order to get a better understanding of large scale processes associated with strain localization, numerical models are often used. Different to laboratory experiments, numerical modelling allows us to get an idea of how fault and shear zones propagate through different lithologies at a larger scale.

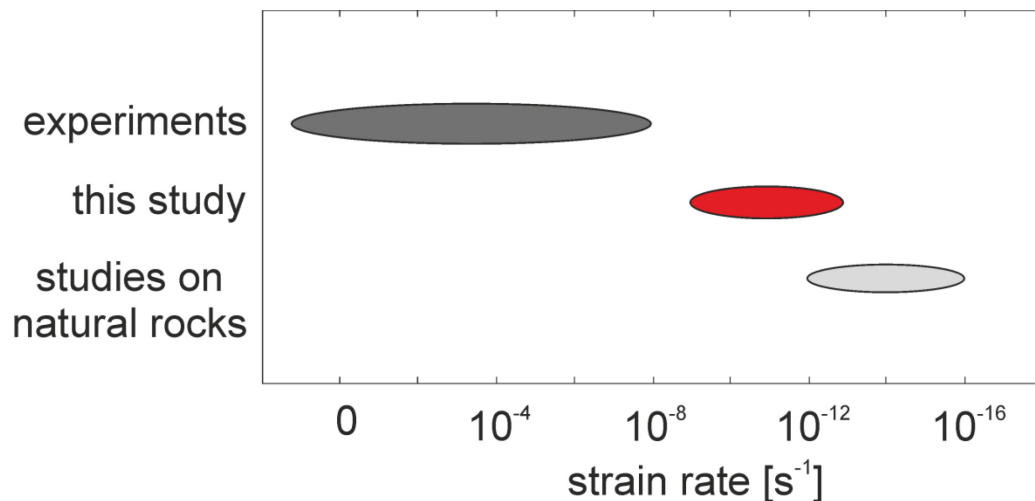


Figure 1.5

Schematic sketch illustrating typical strain rate conditions reported from nature (light grey; Pfiffner and Ramsay, 1982; Oesterling et al., 2007; Bestmann et al., 2000), experimental works (dark grey; De Bresser and Spiers, 1990; 1997; Turner et al., 1954; Griggs et al., 1960; Barnhoorn et al., 2004; Barber et al., 2007; Bruijn et al., 2011) and this study (red).

Summarizing we can say that nature is far more complex than experiments and numerical models. It is thus extremely important to investigate outcrops deformed under well-known P-T, strain and/or strain-rate conditions in detail in order to extrapolate the observations and parameters determined in laboratories to naturally deformed rocks. Examples of such investigated natural laboratories are studies by Stipp

et al. (2002), who analysed naturally deformed quartz and linked the observed microstructure successfully to the experimentally determined dislocation creep regimes of Hirth and Tullis (1992) or Oesterling et al. (2007) who linked microfabrics in naturally deformed marble to varying strain conditions.

1.4 Geology of Syros (Cyclades)

Syros is part of the Cycladic-Blueschist belt, which formed during the Eurasia-Africa subduction (Papanikolaou, 1987; Ring et al., 1993). The Cycladic area can be divided into three main units, separated by tectonic contacts, which are from bottom to top: (1) the para-autochthonous Basement Unit consisting of metasediments and orthogneisses, (2) the Cycladic Blueschist Unit (CBU) composed of metasediments and metabasites, and (3) the Upper Unit made up of ophiolitic rocks, sediments and pre-Eocene metamorphic rocks (Bonneau, 1984; Robertson and Dixon, 1984; Trotet et al., 2001a).

Two major metamorphic events have been recognized and investigated in detail by structural and petrological studies of the Cycladic area (Trotet et al., 2001a; 2001b; Keiter et al., 2004; Schumacher et al., 2008; Huet et al., 2009; Ring et al., 2010; Jolivet and Brun, 2010). An Eocene high-pressure low-temperature metamorphic episode related to burial, stacking and exhumation of the CBU and Basement below the Upper Unit under blueschist- and eclogite-facies conditions (M1); and a younger Oligo-Miocene greenschist- to amphibolite- facies metamorphic episode during crustal extension in the back-arc of the Hellenic subduction zone triggered by the slab-rollback of the African plate (M2). Latter one resulted in the development of several low-angle detachment faults exhuming the CBU from below the Upper Unit. Different shear kinematics have been associated with M2 : On the central islands M2 is mainly associated with top-to-the-north shearing while on the western Cyclades dominant top-to-the-southwest and on the northern islands top-to-the-northeast and –east shearing can be observed (Gautier et al., 1993; Gautier and Brun, 1994; Jolivet et al., 2010; Grasemann et al., 2012).

Syros is dominated by the CBU, only in the southeast of the Island the Upper Unit (i.e. Vari Unit) crops out (Keiter et al., 2011). The rocks belonging to the CBU can be separated into a volcano-sedimentary unit consisting of metapelites, metabasic rocks, quartzites, marbles and schists; and a meta-ophiolitic unit. In both units the two metamorphic events (M1, M2) are well documented by petrological, isotopic and structural work (Maluski et al., 1987; Gautier and Brun, 1994; Trotet et al., 2001a; Trotet et al., 2001b; Schumacher et al., 2008; Philippon et al., 2012; Bröcker et al., 2013). Peak metamorphic conditions are assumed to be around 550 °C and 18 kbar (Trotet et al., 2001b) while the P-T conditions for greenschist-facies overprint are of around 300 – 350 °C and 2 – 4 kbar (Trotet et al., 2001b; Keiter et al., 2004; Schumacher et al., 2008). The two events are linked to different kinematic models, generally an NE-SW to E-W stretching lineation accompanied by a top-to-the-NE to –E shear can be observed for greenschist-facies overprint while M1 deformation is associated with a top-to-the-W sense of shear on the western margin of Syros (Gautier and Brun, 1994; Trotet et al., 2001a; Bond et al., 2007; Keiter et al., 2011; Philippon et al., 2011).

1.5 Organization of the thesis

This thesis is build-up of single chapters based on a published (2), a submitted (4) manuscript and a manuscript in preparation for submission (3). Appendices are attached separately to each chapter.

Chapter 2

In this chapter the investigated outcrop is introduced together with the main idea of this thesis, using a flanking structure developed in almost pure calcite marble as a natural experiment. Detailed microstructure analyses are presented, identifying the active recrystallization and deformation mechanisms in calcite and are further on correlated to deformation strain rates at the given P-T conditions. It is shown that subgrain rotation recrystallization is the dominant recrystallization mechanism in marbles deformed at greenschist facies conditions over a wide range of strain rates.

Chapter 3

In this chapter the deformation of calcite by grain boundary sliding, resulting in major strain weakening at relatively low temperatures (300 °C) and fast strain rates ($\sim 10^{-9} \text{ s}^{-1}$), is characterized in detail using secondary electron microscopy and transmission electron microscopy. Theoretical and experimental determined relationships linking dislocation densities to flow stresses are tested and compared to differential stresses calculated in chapter 2.

Chapter 4

In this chapter the focus is shifted from the rock forming mineral (calcite) to the accessory present white mica. Detailed chemical and isotopic analyses have been made to investigate the influence of host rock deformation on the mineral composition and possible resetting of the K/Ar system. It is shown that at lower greenschist facies conditions the mica is stronger compared to the weak calcite matrix, resulting in only minor brittle deformation of the mica grains.

Chapter 5

This chapter gives a short final conclusion summarizing the main scientific outcome of the thesis and suggestions for further work.

2. Strain rate dependent calcite microfabric evolution – an experiment carried out by nature

Abstract

A flanking structure developed along a secondary shear zone in calcite marbles, on Syros (Cyclades, Greece), provides a natural laboratory for directly studying the effects of strain rate variations on calcite deformation at identical pressure and temperature conditions. The presence and rotation of a fracture during progressive deformation caused extreme variations in finite strain and strain rate, forming a localized ductile shear zone that shows different microstructures and textures. Textures and the degree of intracrystalline deformation were measured by electron backscattered diffraction. Marbles from the host rocks and the shear zone, which deformed at various strain rates, display crystal-preferred orientation, suggesting that the calcite preferentially deformed by intracrystalline-plastic deformation. Increasing strain rate results in a switch from subgrain rotation to bulging recrystallization in the dislocation-creep regime. With increasing strain rate, we observe in fine-grained (3 μm) ultramylonitic zones a change in deformation regime from grain-size insensitive to grain-size sensitive. Paleowattmeter and the paleopiezometer suggest strain rates for the localized shear zone around 10^{-10} s^{-1} and for the marble host rock around 10^{-12} s^{-1} . We conclude that varying natural strain rates can have a first-order effect on the microstructures and textures that developed under the same metamorphic conditions.

Chapter 2. is based on:

Rogowitz, A., Grasemann, B., Huet, B. and Habler, G. (2014). Strain rate dependent calcite microfabric evolution – An experiment carried out by nature. *Journal of Structural Geology* 69, 1-17.

2.1. Introduction

Crystal-plastic deformation of calcite has been the focus of many experimental studies. Different initial grain sizes, strain rates, stresses, temperatures, dry/wet conditions and CO₂ partial pressures have been considered to investigate a wide range of deformation regimes (e.g. Schmid et al., 1980; Schmid et al., 1987; Rutter, 1995; De Bresser and Spiers, 1997; Pieri et al., 2001; Barnhoorn et al., 2004; Barber et al., 2007; Llana-Fúnez and Rutter, 2008; Liteanu et al., 2012; Rybacki et al., 2013). Flow laws for the dislocation and diffusion creep fields have been determined with respect to strain rates, stresses and temperatures (e.g. De Bresser et al., 2002; Renner et al., 2002; Herwegh et al., 2003). Twinning on e-planes seems to be common during deformation of calcite rocks at temperatures below 400 °C (Ferrill et al., 2004). For crystallographic reasons total twinning in calcite would lead to a shear strain of $\gamma = 0.69$, under the simplifying assumption that the twin plane is oriented parallel to the shear-zone boundary (Schmid et al., 1987). Therefore, increasing strain requires the additional activation of intracrystalline slip (Rybacki et al., 2013). Textures developed at small strain ($\gamma < 2$) are similar in a wide temperature range while at greater strain, textures vary with increasing temperature (Barnhoorn et al., 2004). Flow laws and deformation-mechanism maps suggest preferential deformation by grain-size sensitive mechanisms (GSS) at small grain sizes, whereas coarse-grained rocks deform by dislocation creep (Schmid et al., 1987).

Complementary to experimental studies, textural and microstructural investigations of natural calcite marbles characterized shear sense, flow type, deformation mechanisms, and pressure and temperature conditions (Vernon, 1981; Ratschbacher et al., 1991; Kurz et al., 2000; Bestmann et al., 2000; 2003; 2006; Trullenque et al., 2006; Oesterling et al., 2007; Austin et al., 2008). These studies also document a switch from twinning to dislocation creep regime with increasing strain. Recrystallization by subgrain rotation (SGR) and less common bulging (BLG) result in grain size reduction, which is often followed by the activation of GSS creep. However, a direct comparison of experimentally and naturally deformed calcite remains difficult because of the extreme difference between experimental and natural strain rates (Patterson, 1987).

In this study, we investigate deformation mechanisms within and outside the cross cutting element of a flanking structure developed in almost pure calcite marbles on Syros (Cyclades, Greece). Such a structure forms, when a planar inclusion of finite length (i.e. the cross cutting element, CE) deforms within a host rock resulting in the rotation of the CE and slip along it (Grasemann and Stüwe, 2001; Passchier, 2001). Due to the slip gradient along the CE, a heterogeneous strain field in the surrounding area causes marker layers to deform by normal and/or reverse drag (Reches and Eidelman, 1995; Passchier, 2001; Grasemann et al., 2005). Coeval with flanking fold development at low shear strain, deformation within the CE may record shear strain and strain rates, which are much greater than these background values (Grasemann et al., 2011; Fig.2.1). The flanking structure on Syros thus represents a natural experiment, where a specific marble was deformed at relatively small strain-rates in the host rock and at much greater strain rates within the CE under the same metamorphic conditions. The current study documents calcite microfabric evolution for natural geological conditions, providing the opportunity to study deformation and recrystallization mechanisms of calcite as a function of strain and strain rates. The consistency of experimentally determined flow laws, piezometer and paleowattmeter are tested with parameters derived from the calcite samples, which deformed under natural conditions.

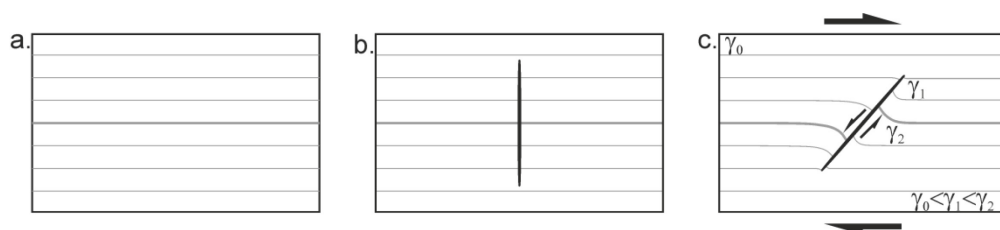


Figure 2.1

Schematic sketch of the development of an a-type flanking structure. a. Foliated host rock. b. A crack develops perpendicular to the host-rock foliation. C. Due to shearing the crack (i.e. CE) rotates, resulting in an antithetic offset along the crack. Note that the displacement of marker lines varies along the cross-cutting element (CE) leading to a spatial variation in strain (γ).

2.2. Geological setting

The island of Syros (Greece) is part of the Cycladic blueschist belt that is situated in the back-arc of the Hellenic subduction zone, where the African plate is subducted northward beneath Eurasia (Papanikolaou, 1987; Wortel et al., 1993; Ring et al., 2003). In the Cycladic area, three main units can be distinguished, separated by tectonic contacts: (1) the para-autochthonous Basement Unit consisting of metasediments and orthogneisses, (2) the Cycladic Blueschist Unit (CBU) composed of metasediments and metabasites, and (3) the Upper Unit made up of ophiolitic rocks, sediments and pre-Eocene metamorphic rocks (Bonneau, 1984; Robertson and Dixon, 1984). Two main metamorphic events affected the Cycladic area (Ring et al., 2010; Jolivet and Brun, 2010 and references therein): An Eocene blueschist- and eclogite-facies metamorphic event related to burial, stacking and exhumation of the CBU and Basement below the Upper Unit; and a younger Oligo-Miocene greenschist-facies event during crustal extension in the back-arc of the Hellenic subduction zone due to the slab-rollback of the African plate. On several Cycladic islands, Oligo-Miocene extension formed low-angle detachment faults exhuming the CBU from below the Upper Unit.

On Syros, both the CBU and the Upper Unit occur (Keiter et al. 2011 and references therein, Fig.2.2). The exposed rocks belonging to the CBU are mainly metagabbros, metabasites, metasediments and schists. The overlying Upper Unit, locally named the Vari Unit, consists of orthogneiss and mylonitic schists, and is considered to be juxtaposed by a brittle detachment fault during late Miocene (Ring et al. 2003).

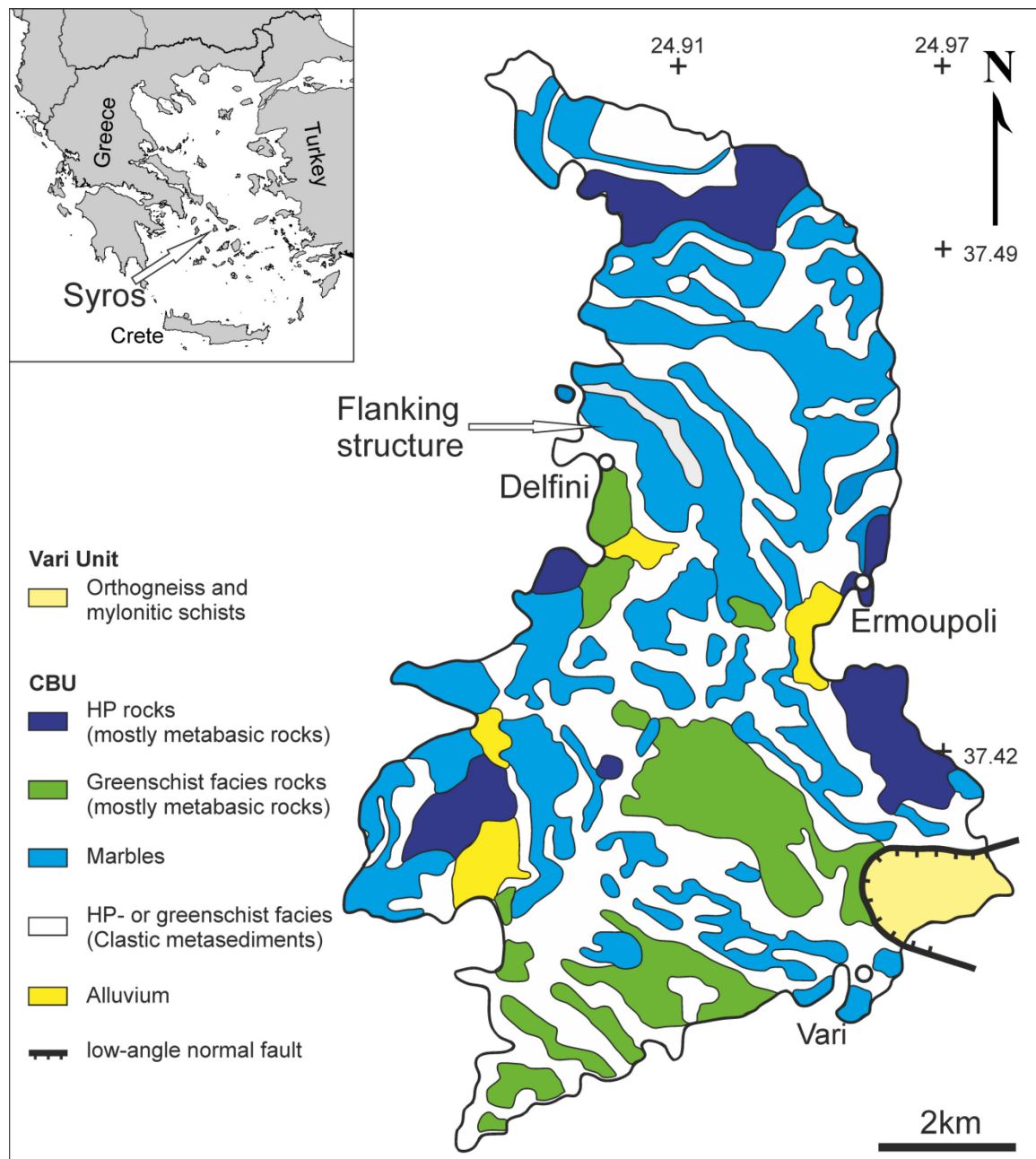


Figure 2.2

Geological map of Syros (modified after Keiter et al. 2004). The arrow points to the location of the outcrop.

New findings however show that the structure of SE Syros is more complex. Detailed mapping by Soukis and Stockli (2013) showed that a third unit composed of chloritic schists, serpentinites and metabasites occurs in a tectonic position between the underlying CBU and the overlying Vari Unit, again juxtaposed by a detachment. Numerous petrological studies constrain the pressure-temperature evolution of the metamorphic rocks (e.g. Trotet et al., 2001b; Schumacher et al., 2008; Philippon et al.,

2012), focusing mainly on the blueschist- and eclogite-facies conditions. The only data for the lower-greenschist-facies metamorphism were reported by Trotet et al. (2001b), suggesting active T-P conditions of 300-350 °C at 2 kbar. In this temperature range, the pressure proposed by other authors in more speculative P-T paths is approximately 4 kbar (Keiter et al., 2004; Schumacher et al., 2008, Fig.2.3). In general an increase in greenschist-facies overprinting toward the SW Syros involves a NE-SW to E-W stretching lineation with a top-to-the-NE and –E sense of shear (Trotet et al., 2001a; Keiter et al., 2004; Philippon et al., 2011).

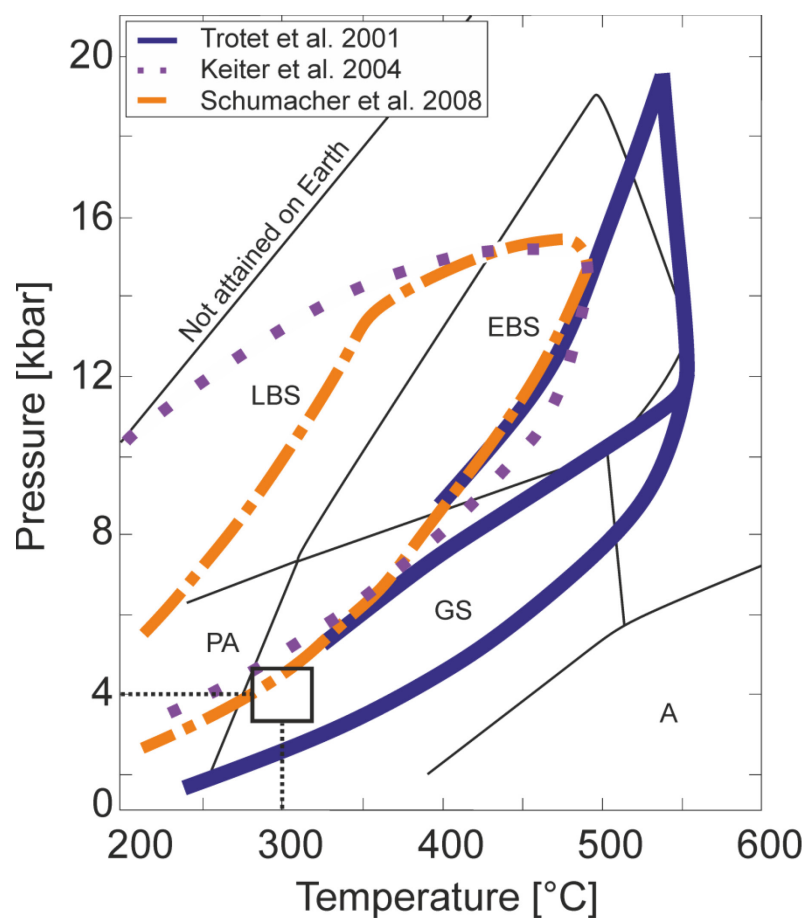


Figure 2.3

P-T paths for Syros determined by Trotet et al. (2001), Keiter et al (2004) and Schumacher et al. (2008). LBS=lawsonite-blueschist. EBS=epidot-blueschist, GS=greenschist, A=amphibolite and PA=pumpellyite-actinolite (after Evans, 1990). The black box represents the P-T range of the deformation stage considered in this study.

2.3. Material and Methods

2.3.1 Outcrop description

The investigated outcrop is located N of Delfini in the western part of Syros island at the base of a several tens of meters marble layer in the CBU (Fig.2.2, UTM35 414840N 313839E, the reader is invited to download a high-resolution 3D-model of the outcrop mapped with an unmanned aerial vehicle, from the electronic supplement). The marble is composed of nearly pure, coarse grained calcite. Minor amounts of white mica are dispersed between the calcite grains and, more rarely, concentrated in thin layers. Slight differences in colour and dolomite content reflect the main foliation (average orientation: 015/38, Fig.2.4a, b). A lineation is defined by the shape preferred orientation of calcite and white mica (Fig.2.4b, average orientation: 090/11). Shear zones and flanking structures indicate top-to-the-E shear consistent with the observations of Trotet et al. (2001a) in this area of Syros.

We focused our study on one large flanking structure (Fig.2.4a) that is dominated by one central CE characterized by a darker colour and a smaller grain size than the host rock marble and orientated 005/50. The CE is 5 m long and its width varies from 1 to 2.5 cm. The angle between the CE and the marble is around 20°. In the vicinity of the CE, the mylonitic foliation of the host rock records a reverse drag in both, the hanging wall and the footwall of the structure and is offset by a top-to-the W shear sense resulting in an angle of around 45° between marble foliation and CE right next to the structure. The trace of the schistosity has an inflection point at the immediate margin of the CE (Fig.2.4d) indicating a change from reverse to normal drag close to the widening CE (Exner and Grasemann, 2011). The displacement along the CE varies from around 20 cm at the lower tip up to 120 cm at the center of the structure (Fig.2.4c).

The orientation of the CE with respect to the background shear direction and the observed drag indicate that the studied flanking structure can be interpreted as an a-type flanking fold (Grasemann and Stüwe, 2001), that formed during top-to-the-E background shearing. Since close to the investigated outcrop, layer-perpendicular fractures are overprinted by ductile shears of various magnitudes, we believe that the studied flanking structured formed along such a crack, which operated as CE, rotated

into the shear direction and led to passive folding of the marble host-rock foliation because of the antithetic slip gradient along the CE.

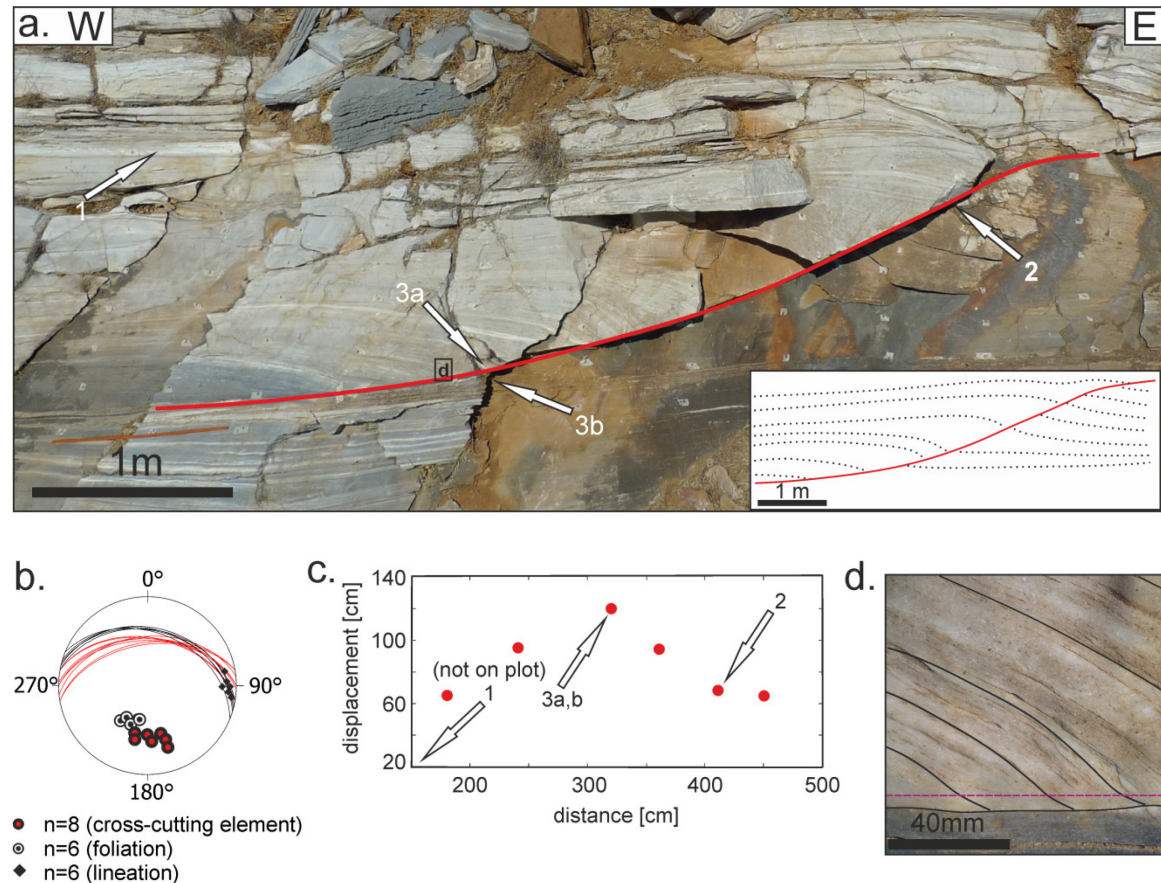


Figure 2.4

a. Sample locations within the outcrop. The inserted sketch shows the deflection of the passive markers (dotted lines). The CE has been retraced by a red line. b. Equal-area, lower hemisphere projection showing the orientation of the cross-cutting element, and the foliation and stretching lineation of the host rock. c. Diagram showing the displacement plotted over the distance along the cross-cutting element with respect to the bottom of the flanking structure. d. Close-up at the boundary of CE and host rock showing a switch from reverse to normal drag at location of the purple line (location shown in Figure 2.4a).

Three samples were collected from three different structural locations in and around the flanking structure (Fig.2.4a, d). Samples 1, 2 and 3 (later separated into 3a and 3b) were collected, respectively, in the host rock at 1.5 m distance from the cross-cutting element, in and around the cross-cutting element in a zone of 60 cm displacement and in and around the cross-cutting element at its location of maximal displacement of 120 cm.

Analogue and numerical models, and analytical solutions have shown that flanking structures form at a small background shear strain of $\gamma < 5$ with a rotation rate of the CE similar to a passive marker line (Exner et al., 2004; Kocher and Mancktelow, 2005; Reber et al., 2012). Flanking structures are therefore kinematic indicators restricted to low strain. Assuming simple shear deformation, it is possible to calculate the shear strain, for the flanking structure from the geometric relationship between the orientation of a passive marker before and after deformation (Ramsay and Huber, 1983):

$$\gamma = \cot(\alpha) - \cot(\alpha'), \quad (\text{Eq. 2.1})$$

where α and α' are respectively the orientation of the passive marker with respect to the simple shear direction before and after deformation. Assuming an initial orientation of the fracture to be perpendicular to the foliation ($\alpha = 90^\circ$) and considering the orientation of the CE after deformation ($\alpha' \approx 20^\circ$), the background shear strain that formed the flanking structure was $\gamma < 3$. This value corresponds to the shear strain recorded by sample 1. Note that γ does not change dramatically, when the flow is not ideal simple shear (further information on the calculation of the overall background-shear strain can be found in the appendix A2.1).

At the position of sample 2, the offset of the marker layers indicates 64 cm displacement along the CE and the CE has a thickness of 1.2 cm. Assuming simple shear the shear strain is $\gamma = 53$. Sample 3 comes from the centre of the CE where the displacement is at its maximum of 120 cm and the CE is 1.5 cm thick. Assuming homogeneous simple shear, the values correspond to a shear strain $\gamma = 80$. At this locality, two very fine-grained, porcelain-like layers flank the CE. If we assume that these fine-grained layers with a total thickness of 0.12-0.48 cm, accommodated most of the displacement, the shear strain is in the range of $250 < \gamma < 1000$. Because of the macroscopic heterogeneous appearance, sample 3 was further split for analysis into coarser grained sample 3a and a sample 3b comprising the fine-grained-localized zones. Based on our microtectonic studies we separate three strain domains: low-strain domain (sample 1 and 3a), intermediate-strain

domain (sample 2) and high-strain domain (sample 3b). Finally, assuming that the microstructures in the three strain domains formed simultaneously, the three shear-strain domains also reflect strain-rate domains. Consequently, when the flanking structure formed, the strain rate in the CE was up to three orders of magnitude greater than in the host rock. Given the model for flanking structures, the strain rate at a given point can be assumed as constant, and therefore, this well-preserved structure can be regarded as a result of a progressive ductile deformation.

2.3.2 Sample preparation

The samples were cut in the inferred local XZ plane of finite strain. Sample 1 was cut perpendicular to the main foliation and parallel to the stretching lineation. Samples 2, 3a and 3b were cut perpendicular to the CE boundary and parallel to the stretching lineation of the CE. It must therefore be emphasized that the sample reference frames are different. They are all cut along an approximately vertical plane striking E-W but differ by an up to 45° rotation around a horizontal N-S axis.

Mechanically polished thin-sections with a thickness of about 20 to 30 μm were prepared for microstructure analysis. Thin sections selected for scanning electron microscopy and electron backscatter diffraction analysis (EBSD) were additionally chemomechanically polished with an alkaline colloidal silica suspension (Köstrosol 3530; pH 9.2-10). These samples were coated with a thin carbon film to establish electric conductivity.

2.3.3 Microstructure analysis

Microstructure and modal composition of the samples were analysed with a Leica DM4500 P optical microscope. Optical micrographs were taken with plane and crossed polarized light (Fig.2.5, 2.6).

Digitized optical micrographs and EBSD data were used for grain shape analysis. The grain parameters were automatically measured by using the DiAna V3 software (© J.

Duyster). The 2D-orientation of the grain long axes are presented in rose diagrams to show shape preferred orientation (SPO) within the fabric (Fig.2.5, insets). The orientations are given in degrees, anticlockwise with respect to the reference frame. The grain size is characterized by the equivalent diameter d that is calculated as follows:

$$d = 2\sqrt{A/\pi}, \quad (\text{Eq. 2. 2})$$

where A is the grain area. For the different samples and microstructural areas, the distribution of grain size is represented in histograms and the mean grain sizes and standard deviation are reported (Fig.2.7).

2.3.4 Texture analysis

Crystallographic preferred orientations (CPOs), grain-shape parameters and the grade of intracrystalline deformation in terms of misorientation were measured by combined EBSD mapping and EDX-spectrometry on a FEI Quanta 3D FEG instrument. The FIB-SEM is equipped with a field-emission electron source and an EDAX Pegasus Apex 4 system consisting of a Digiview IV EBSD camera and an Apollo XV silicon drift detector for EDX-spectrometry. The instrument was operated with a 10 or 15 kV accelerating voltage, a 4 nA probe current and at working distances ranging between 10 and 14 mm and a sample tilt angle of 70°. Different calcite microfabric areas were mapped by beam scanning in square or hexagonal grid mode using a fixed step size in a range between 0.25 and 3.7 μm specifically chosen depending on the grain size. During data collection, the EBSD camera was set to an exposure time of 47 - 103 ms using a camera binning of 4x4 (348x260 pixel) or 8x8 (174x130 pixel). The Hough space resolution was set to a binned pattern size of 140-160 and a Theta step size of 1°. A Rho fraction of 80-85 % was used for band detection and indexing in order to exclude weak marginal portions of the EBSD pattern. For all data, a 9x9 convolution mask was applied to determine 6-10 or 6-12

peaks at a minimum peak distance of 10-15 pixels in Hough space. With the given settings, indexing rates of 10-21 points per second were achieved.

The OIM Data Collection and Analysis software were used for indexing and processing the EBSD data. Indexing of Kikuchi patterns was based on EDX intensity ranges for specific elements to identify the phases by composition. Grain boundaries were set at a misorientation angle greater than 15° between adjacent points. For detailed texture analysis, host grains and recrystallized grains were separated according to their size and shape. Orientation distribution functions (ODFs) were calculated after Bunge (1982). The orientation of the *c* (0001), *-a* <11-20>, *a* <-1-120> axes and *r* planes {10-14} were derived from the ODF by use of the MATLAB toolbox for quantitative texture analysis MTEX (<https://code.google.com/p/mtex>, Bachmann et al., 2010). The data are plotted as equal area upper hemisphere projections (Fig.2.8).

The misorientation-angle distributions of neighbouring grains (correlated) and for every grain related to every other grain, belonging to one grain population (uncorrelated, see for example Halfpenny et al, 2012), was detected by the OIM Data Analysis software and are represented together with the calculated theoretical, random misorientation-distribution curve for trigonal crystal symmetry (Fig.2.9, Mackenzie and Thomson, 1957).

2.4. Results

Microfabrics for the different strain domains are described in terms of grain size distribution, SPO, texture and misorientation-angle distribution. Using the terminology of Sibson (1977) the marble microstructures are distinguished based on the fraction of recrystallized grains:

protomylonites, mylonites and ultramylonites have less than 50% fractions, 50% to 90% fractions and more than 90% fractions recrystallized grains, respectively. Additionally, fine grained ultramylonites are ultramylonites having an average grain size less than 9 µm.

2.4.1 Marble microfabric in the low-strain domain

The microstructure of the low-strain domain marble is characterized by coarse calcite grains with a grain size around 300 μm (Fig.2.5a, b). Within dolomite-rich layers (dolomite fraction larger than 20%), calcite grains are smaller with grain sizes ranging between 25 and 245 μm . The grain-size-distribution plot shows two peaks, one well defined at 150 μm and a second less pronounced at 300 μm (Fig.2.7a). The grains show a strong SPO with the long axes oriented at 40°, consistent with the top-to-the E sense of shear in the host rock. Undulatory extinction and the minor presence of subgrain boundaries indicate intracrystalline deformation. Grain boundaries are slightly curved showing evidence of grain boundary migration (GBM). Conjugate narrow or tabular twins are observed corresponding to Type I and Type II twins respectively (Ferrill et al., 2004).

The texture of the low strain domain is mainly characterized by a strong maximum of c axis perpendicular to the foliation (Fig.2.8a). There is only a weak girdle arrangement of a and -a axes approximately 50 ° inclined to the foliation plane while the r planes do not record a preferred orientation. The observed clusters represent single crystal maxima.

Next to the CE (sample 3a), similar microstructural and textural features are rotated by an angle of 40° to 50°, consistent with the passive rotation of the main foliation due to the reverse drag close to the CE (Fig.2.8b). As a result, the long axes of the grains are parallel to the CE boundary (Fig.2.5b). Misorientation distribution curves for correlated and uncorrelated grains differ radically from the random misorientation distribution. They have a common peak located between 45 and 60° (Fig.2.9a). An additional peak occurs at 80° for the correlated grains and at 30° for uncorrelated grains.

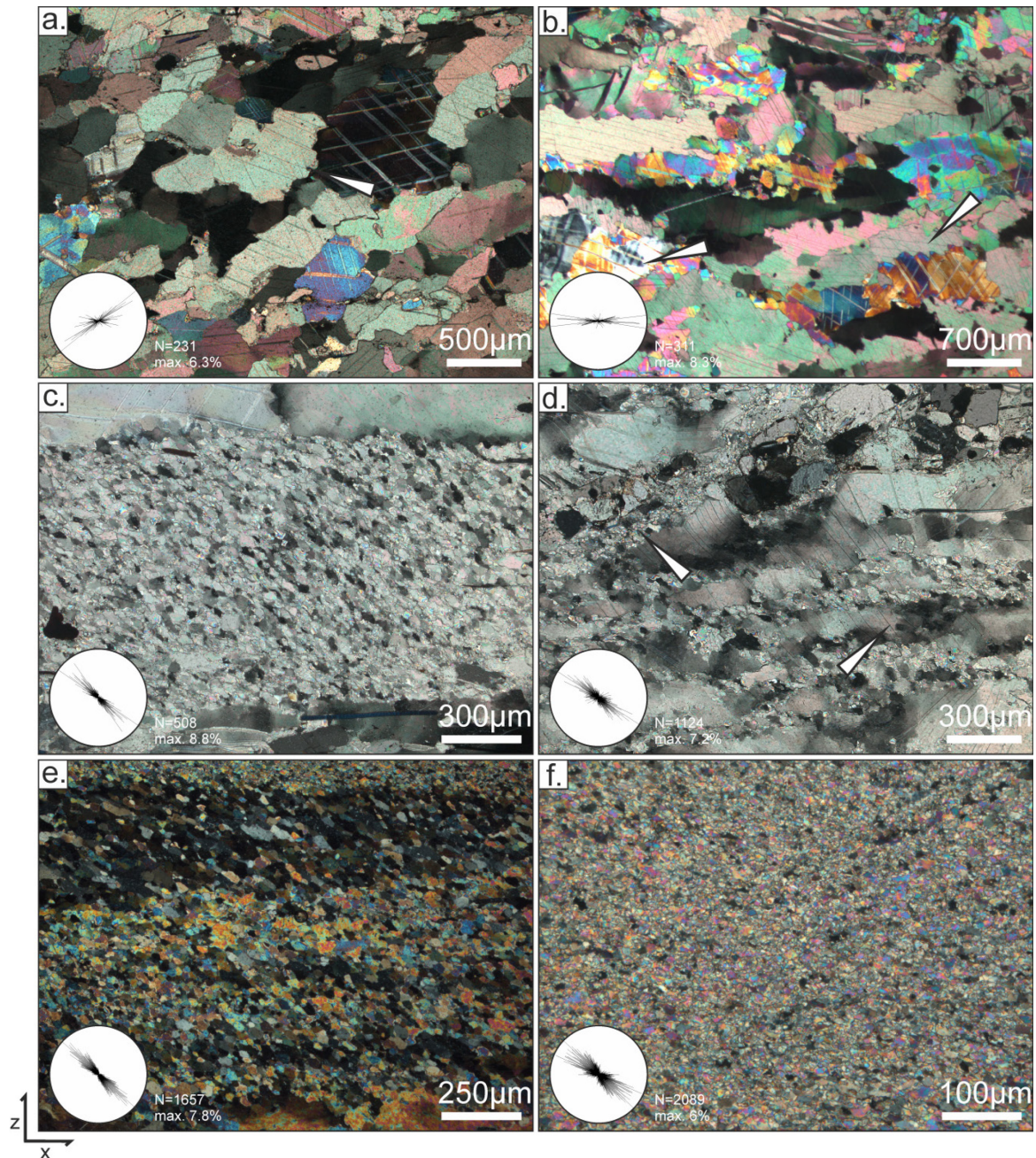


Figure 2.5

Optical micrographs (crossed polarizers). Insets are rose diagrams showing the 2D orientation of the calcite grain long axes. N represents the total number of measured grains and max. the maximal percentage. In all micrographs left side corresponds to W. a. Coarse calcite grains (low-strain domain, sample 1) of the host rock showing a weak undulatory extinction and a SPO with an angle of 40° relative to the foliation. Locally sutured grain boundaries occur whereas twins are preferentially straight and thin. b. Coarse calcite grains of the host rock (low-strain domain, sample 3a) showing undulatory extinction and sutured grain boundaries. Note that the grains have been rotated with respect to the cross-cutting element leading to an alignment parallel to the foliation. c. Equigranular, recrystallized calcite ultramylonite next to protomylonite (intermediate-strain domain, sample 2). d. Protomylonitic calcite showing a core-mantle structure with strongly deformed host grains surrounded by recrystallized grains (intermediate-strain domain, sample 2). e. Equigranular, recrystallized calcite ultramylonite (high-strain domain, sample 3b). f. Fine grained ultramylonite layer (high-strain domain, sample 3b).

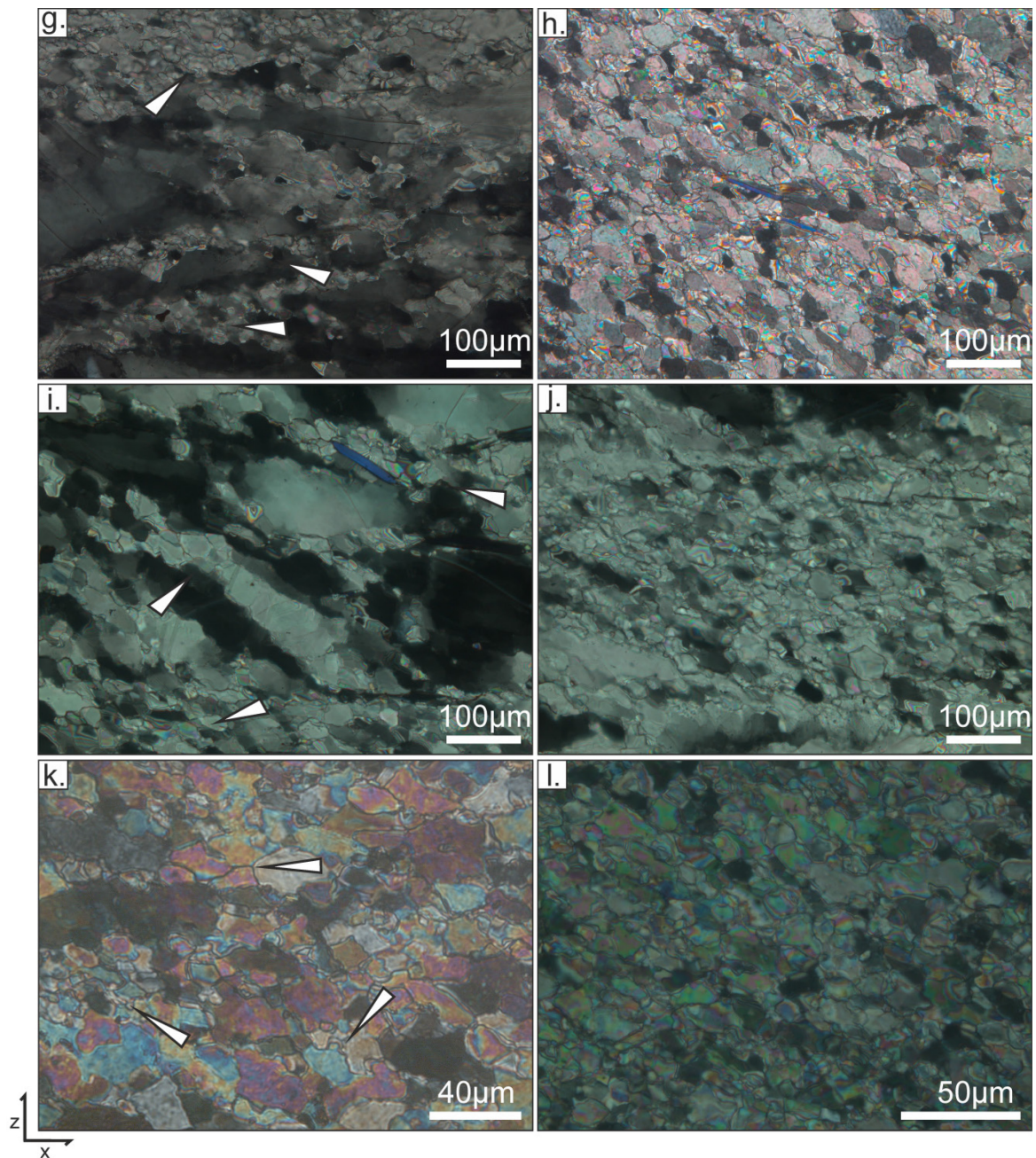


Figure 2.5 (continued)

g. Core-mantle structures showing that subgrains and recrystallized grains have the same size (intermediate-strain domain). White arrows point to location of subgrains and recrystallized grains. h. Close-up of ultramylonitic calcite (intermediate-strain domain). i. Core-mantle structure showing that subgrains and recrystallized have a similar size (high-strain domain). White arrows point to the location of subgrains and recrystallized grains. j. Close-up of ultramylonitic calcite (high-strain domain). k. Boundary between ultramylonitic and fine-grained ultramylonitic calcite. Presence of fine grained ultramylonite layer amongst mylonitic grains. Note the small bulges and triple junctions (arrows). l. Close-up of fine grained ultramylonitic layer.

2.4.2 Marble microfabric in the intermediate-strain domain

The microstructure of the intermediate-strain domain is characterized by a strong foliation (CE plane) defined by alternating protomylonitic and ultramylonitic layers (Fig.2.5c, d, g, h). Thickness measurements in thin sections, reached values up to 4 mm for protomylonitic and up to 800 μm for ultramylonitic layers.

Within protomylonite layers, the calcite grains are elongate and show strong intracrystalline deformation (Fig.2.5d, g). Undulatory extinction and curved twins are common. Locally, sutured twin- and grain-boundaries can be observed. Larger calcite porphyroclasts (average grain size 52 μm , Fig.2.7b) built-up of subgrains (average grain size 13 μm , Fig.2.7c) are surrounded by recrystallized grains with a similar size as the subgrains (average grain size of 9.5 μm , Fig.2.7d), creating a core-mantle structure. The recrystallized grains have a SPO oriented at 150° consistent with the antithetic top-to-the-W sense of shear in the CE (Fig.2.5d). The ultramylonitic layers consist of equigranular calcite (Fig.2.5c, h). The grain size ranges between 5 μm and 40 μm , with an average of 10 μm (Fig.2.7e). The grains show a strong SPO aligned at an angle of around 120° to 150° relative to the CE boundary defining a secondary foliation (Fig.2.5c, h). Notice that the recrystallized grains from the protomylonitic and ultramylonitic layers have similar grain size and SPO characteristics.

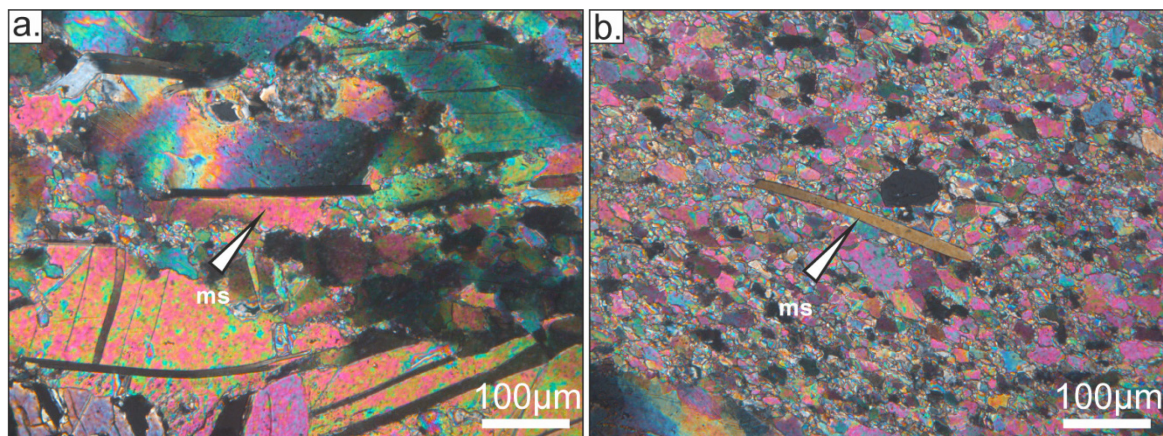


Figure 2.6

Optical micrographs of mica (crossed polarizers). In all micrographs left side corresponds to W. a. Mica in protomylonitic layer aligned parallel to the cross-cutting element boundary. b. Mica in mylonitic layer aligned parallel to long axes of recrystallized grains.

White mica grains within the protomylonitic layers lie parallel to the cross-cutting element boundary consistent with the stretching direction of the calcite grains (Fig.2.6a). Micas within the ultramylonitic layers are aligned with their long axes parallel to the long axes of recrystallized calcite grains (Fig.2.6b). Quartz is present as single grains lacking any evidence for a preferred orientation or intracrystalline deformation like undulatory extinction, bulging or subgrain formation and are therefore essentially behaving as rigid clasts.

The deformed calcite host grains show a strong point maximum of c axis inclined 30 to 40° to the z-axis of the pole figure while the a and –a axes show three maxima aligned on a girdle normal to the c axis (Fig.2.8c). The separated a and –a axes pole figures can be transformed into each other by a rotation of 180° around the crystal c axis. The texture contains a two-fold-symmetry axis parallel to y axis of the sample and records therefore a monoclinic symmetry.

The c axis of recrystallized grains from core-mantle structures within the protomylonitic layers and c axis of grains within the ultramylonitic layers are normal to the CE plane while the a and –a axes form a girdle in the CE plane (Fig.2.8d, e). There is no clear difference of a and –a axis distribution noticeable for the grains in the ultramylonitic layers. The texture corresponds therefore approximately to an orthorhombic symmetry with three two-fold-symmetry axes parallel to the sample z, y, and x axis respectively. The main maximum of the r poles is orientated slightly oblique to the pole of the CE plane.

Host grains, recrystallized grains of protomylonitic layers and grains of ultramylonitic layers within the intermediate strain zone show a clear CPO although an increasing amount of recrystallized grains is associated with a slight decrease in CPO strength (Fig.2.8c, d, e). Disregarding differences in the intensity of the distribution, the texture of recrystallized grains is apparently the result of an anticlockwise rotation of the texture of the host grains around the sample y axis.

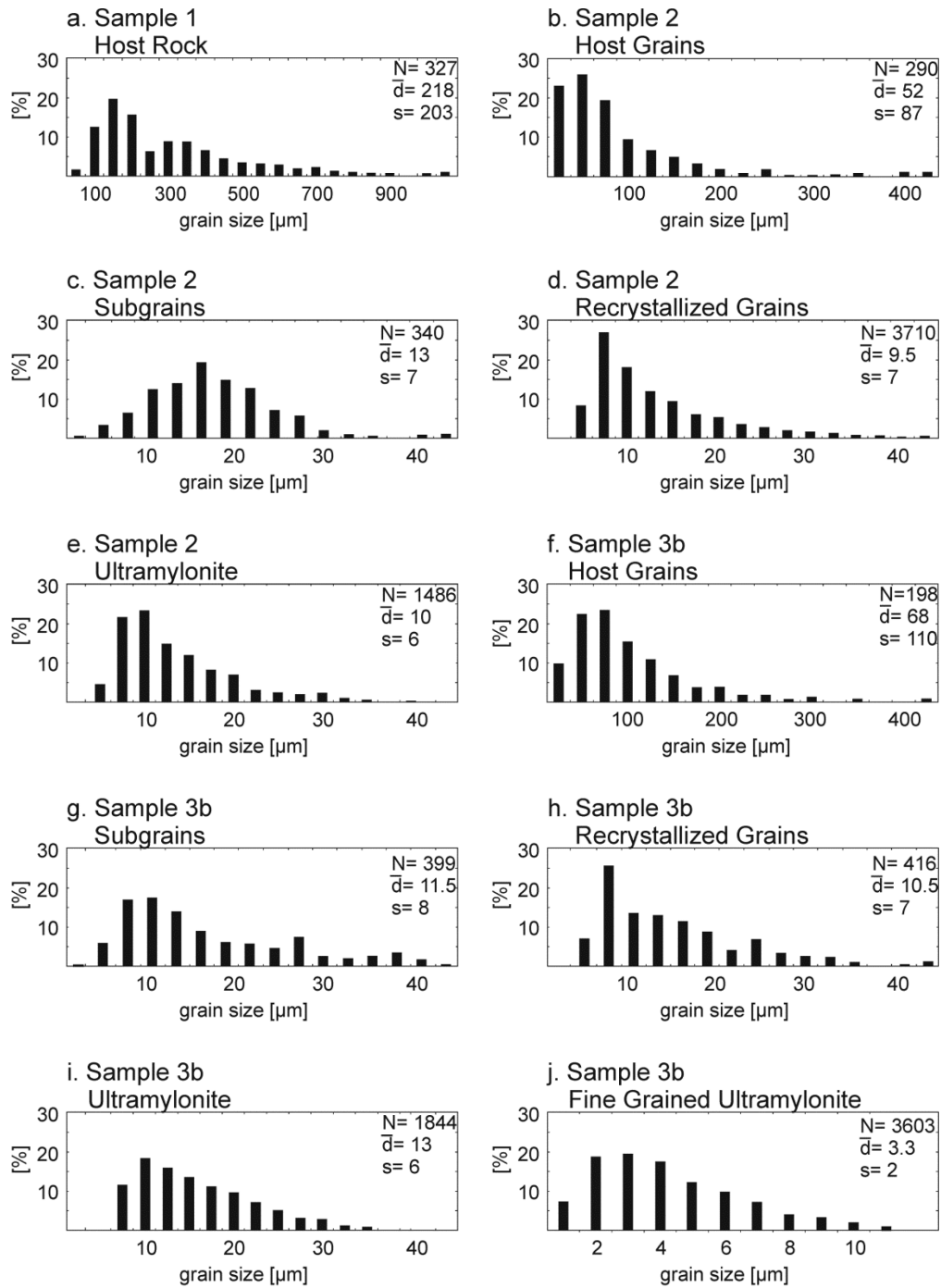


Figure 2.7

Grain-size histograms of dominant microstructures of low-strain (a.), intermediate-strain (b., c., d., e.) and high-strain domains (f., g., h., i., j.). Note that recrystallized grains of protomylonitic layers and ultramylonitic layers have almost the same grain size distribution. N= total number of analysed grains, \bar{d} = mean grain size, s= standard deviation.

In the core-mantle structure, both misorientation-angle-distribution curves for correlated and uncorrelated grains differ from the random misorientation-angle

distribution. Similar to the low-strain domain the curve for uncorrelated grains shows a peak at around 50° while the misorientation-angle-distribution curve for correlated grains shows a peak at 80° and higher frequencies at misorientation angles smaller 20° (Fig.2.9b).

For the ultramylonitic layer, both curves also differ from the random one. The curve for uncorrelated grains is approximately the same as for the protomylonite but with a less distinct peak around 50 to 60° (Fig.2.9d). Except for a small gain at low misorientation angles and slightly smaller frequencies at greater misorientation angles, the curve for correlated grains is similar to the curve for uncorrelated grains.

2.4.3 Marble microfabric in the high-strain domain

The microstructure of the high-strain domain is characterized by protomylonitic, ultramylonitic and fine-grained ultramylonitic layers. Fine grained ultramylonitic layers occur only close to the boundary between the cross-cutting element and the host rock. Thickness measurements in thin section reached values up to $1750\text{ }\mu\text{m}$ for protomylonitic, up to $1500\text{ }\mu\text{m}$ for ultramylonitic and up to $240\text{ }\mu\text{m}$ for fine-grained ultramylonitic layers.

In protomylonitic layers, core-mantle structures compare well to the intermediate-strain domain. They show intensely deformed calcite grains (average grain size $68\text{ }\mu\text{m}$, Fig.2.7f) that partly contain wedge shaped twins preferentially oriented with an angle of 150° with respect to the cross-cutting element boundary. The larger calcite grains contain a high amount of subgrains with an average grain size of $11.5\text{ }\mu\text{m}$ (Fig.2.7g) and are surrounded by recrystallized with a similar average grain size ($10.5\text{ }\mu\text{m}$, Fig.2.7h).

Recrystallized grains of ultramylonitic layers have an average grain size of $13\text{ }\mu\text{m}$ (Fig.2.7i). Their long axes are aligned between 110° and 150° , the SPO is more pronounced than in the other domains (Fig.2.5e). Close at the boundary to the fine grained ultramylonite, a higher amount of small bulges can be observed at boundaries of ultramylonitic grains (Fig.2.5k).

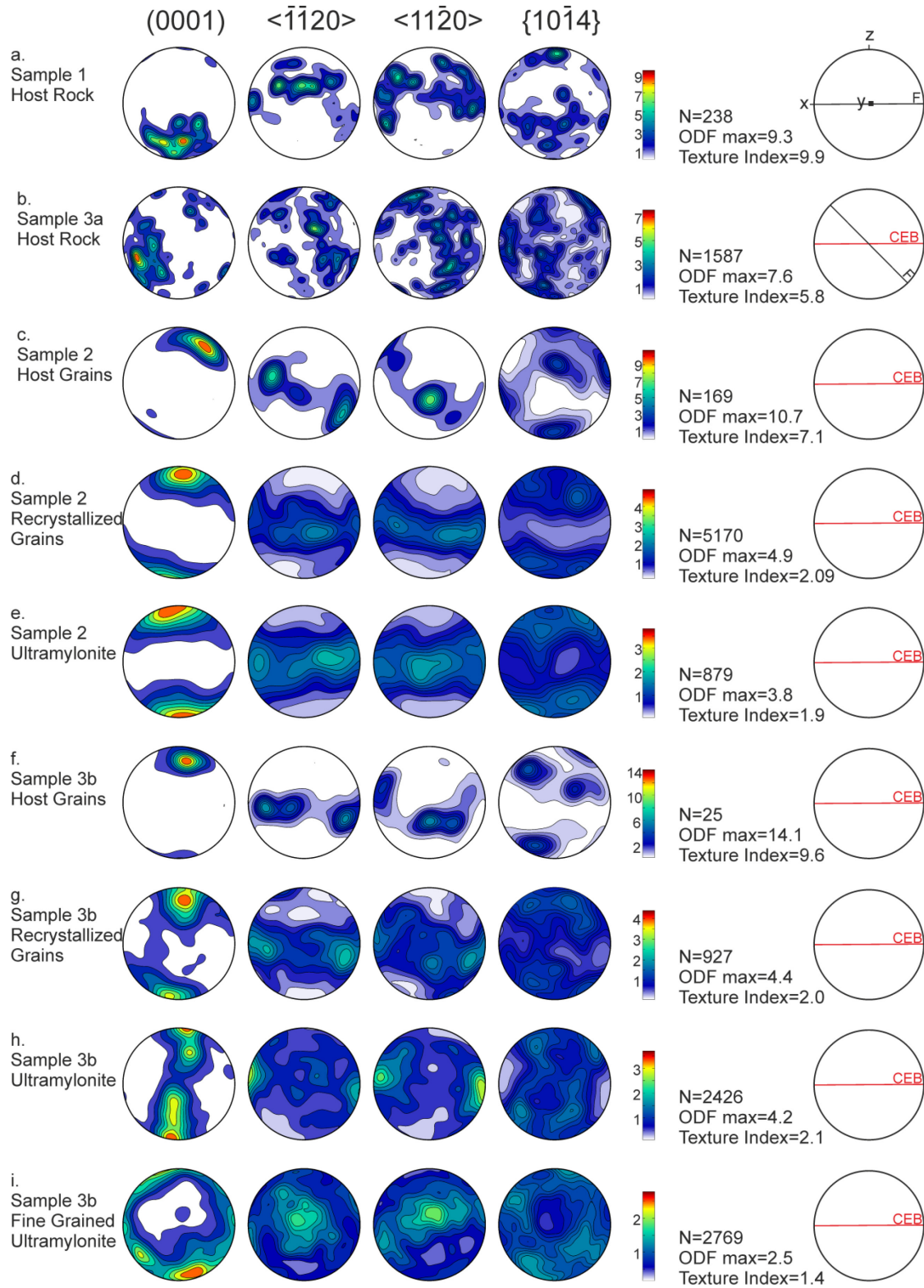


Figure 2.8

Stereographic equal-area upper hemisphere projection of c (0001), -a $\langle \bar{1}1\bar{2}0 \rangle$, a $\langle 11\bar{2}0 \rangle$ axes and r planes $\{10\bar{1}4\}$ of calcite. z, y and x show the sample axes, the black line (F) represents the foliation and the red line (CEB) the cross-cutting element boundary. a. Host rock (low strain domain, sample 1). b. Host rock next to cross-cutting element (low strain domain, sample 3a). c. Host grains of protomylonitic layer (intermediate-strain domain, sample 2). d. Recrystallized grains of protomylonitic layer (intermediate-strain domain, sample 2). e. Recrystallized grains of mylonitic layer (intermediate-strain domain, sample 2).

Fine-grained ultramylonitic layers have an average grain size of $3.3\ \mu\text{m}$ (Fig.2.7j). The grains show a weaker SPO than those in the ultramylonite (Fig.2.5f). Locally triple-junctions with nearly dihedral 120° angles occur (Fig.2.5k, l).

Within the protomylonitic layers, the calcite texture of host grains and surrounding recrystallized grains are similar (Fig.2.8f, g). The c axis of host grains are oriented perpendicular to the CE plane, whereas three separated point maxima of a axes are aligned on a girdle within the CE plane. The recrystallized grains of the core-mantle structure show approximately the same CPO although less pronounced.

The texture of the new recrystallized grains from the ultramylonitic layers differs significantly from that of the intermediate-strain domain (Fig.2.8h). The c axes of calcite grains in the ultramylonitic layers form a girdle normal to the lineation while the a and -a axes form point-maxima parallel to the lineation. The r poles are aligned in a crossed girdle.

The texture of grains from the fine-grained ultramylonitic layers is weak with a texture index of 1.4. It differs from the texture of ultramylonitic grains by a 90° rotation around the sample z axis, leading to a point-maximum of a and -a axes in the centre of the pole figure and c axis arranged at the periphery of the pole figure (Fig.2.8i).

The distribution curve for misorientation angles of the protomylonite lack the peak at around 50 to 60° for uncorrelated grains reflected by all other microstructures so far. Instead, a local minimum around 40 to 50° can be observed for correlated and uncorrelated grains. Both curves show a peak around 80° characteristic for e-twinning in calcite (Fig.2.9c). The misorientation-angle distribution for uncorrelated ultramylonitic grains is bell-shaped with a maximum around 60° . The curve for correlated grains shows a strong peak at 80° (Fig.2.9e). In fine-grained ultramylonitic layers the misorientation curves for correlated and uncorrelated grains are very close to the theoretical curve for random grains (Fig.2.9f).

Figure 2.8 (continued)

f. Host grains of protomylonitic layer (high-strain domain, sample 3b). g. Recrystallized grains of protomylonitic layer (high-strain domain, sample 3b). h. Recrystallized grains of mylonitic layer (high-strain domain, sample 3b). i. recrystallized grains in ultramylonitic layer (high-strain domain, sample 3b).

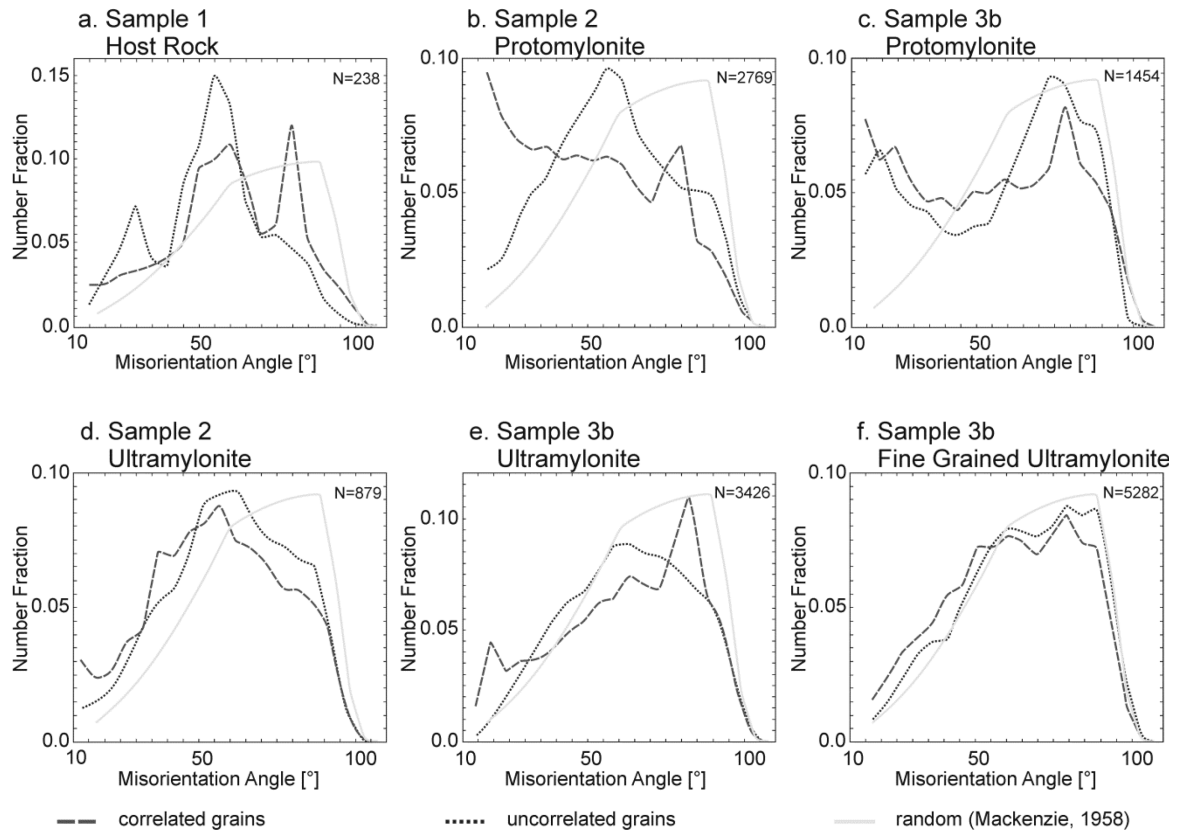


Figure 2.9

Misorientation angle distribution plots of dominant microstructures in low- (a.), intermediate-(b., d.) and high-strain domains (c., e., f.). N represent the total number of analysed grains.

2.5. Discussion

2.5.1 Relative timing of microstructure development

The observed microstructures can be linked to the two different metamorphic events that affected Syros. On the one hand, within the low strain domain, the observed coarse calcite grains are likely the result of grain growth at elevated temperatures (Barnhoorn et al., 2004) during the blueschist or eclogite facies evolution of Syros metamorphic rocks (at 400-550 °C). Smaller grain sizes in this strain domain, are always correlated to the presence of greater amounts of dolomite grains. Therefore, we assume that the presence of the second phase inhibits grain growth, causing a smaller calcite grain size (Olgaard and Evans, 1986; 1988; Tullis and Yund, 1982).

On the other hand, features related to ductile deformation within all three strain domains like curved grain boundaries, undulatory extinction, development of core-mantle structures and mylonitization are likely to be related to Miocene-greenschist-facies deformation. If these structures had formed during early blueschist-eclogite-facies metamorphism, they would have been annealed, producing straight grain boundaries and absence of undulatory extinction. A second source of evidence for development during greenschist-facies metamorphism is that experimental study of calcite annealing shows a switch in the r axes alignment, producing a preferential orientation of one r pole maxima in the shear plane and another one normal to the shear direction if annealing occurs (Barnhoorn et al., 2005). Such a texture is absent, so we infer that the crystallographic texture of these structures was not annealed, and postdated the earlier metamorphism. Another factor supporting deformation during greenschist-facies metamorphism is that the orientation of the recrystallized grain long axes within the host rock display top-to-the-east sense of shear observed on Syros during the later metamorphism (Keiter et al., 2004). The orientation deviation of the SPO as well as the CPO of the grains next to the CE is apparently caused by the passive rotation of the host rock foliation during flanking structure development (Grasemann et al., 2005). The observed angle of 40° to 50° is identical to the structural field measurements, texture and SPO indicating that the observed SPO and CPO preceded flanking-structure formation.

2.5.2 Strain-rate dependent calcite deformation and recrystallization mechanisms

Within the low-strain domain, the microfabric is characterized by preferentially orientated, coarse-grained calcite marble. The strong SPO with grain long axis orientated at 40° to the foliation can result from top-to-the-E shearing during crystal plastic-deformation. The observed undulose extinction indicates the presence of geometrical necessary dislocations which may cause the development of a CPO (Hirth and Tullis, 1992). Although dissolution precipitation creep and stress-directed grain growth may also lead to the formation of a weak CPO (Bons and den Brok, 2000), these processes are not considered to be responsible for the observed SPO because crystal-plastic

deformation can be directly linked with undulose extinction and presence of subgrains. Slightly curved grain boundaries are probably the result of grain-boundary migration (GBM) indicating that the deformation took place within the dislocation-creep regime. Temperatures above 200 °C, which have most likely prevailed in the investigated rocks, already activate dynamic recrystallization in calcite (Herwegh and Pfiffner, 2005), which is therefore likely to deform by GBM at moderate temperatures as observed by Spacek et al. (2001) and Kennedy and White (2001).

With increasing strain and strain rate, deformation results in further intracrystalline deformation of the grains and formation of small recrystallized grains along the boundaries of pre-existing grains. These protomylonitic zones are characterized by a core-mantle structure where host grains are surrounded by recrystallized grains. The fact that subgrains within the host grains and recrystallized grains show almost the same size indicates that SGR was the dominant recrystallization mechanism. Similar core-mantle structures occur already at low shear strains in naturally deformed calcite (Bestmann et al., 2000) and experimentally at shear strains between $2 < \gamma < 5$ (Schmid et al., 1987).

The surrounding recrystallized grains show a reorientation of the c axis perpendicular to the foliation whereas the a and -a axes form a girdle within the foliation plane. The strong difference in misorientation angle distribution curves for correlated and uncorrelated grains indicates a dependence of neighbouring grains, emphasizing that SGR was the dominant deformation mechanism (Bestmann et al. 2000; Wheeler et al., 2001). With progressive deformation, further recrystallization occurs resulting in the formation of ultramylonitic layers with more than 90 % recrystallized grains. Due to grain-boundary alignment of the new recrystallized grains, a secondary foliation oblique to the CE-boundary develops (Barnhoorn et al., 2004). The change in texture symmetry from monoclinic to orthorhombic is most likely caused by activation of a different slip system.

Deformation at greater strain and strain rate results in similar microstructures as within the intermediate strain domain such as core-mantle structures and the development of ultramylonitic layers. Also in the high-strain domain, subgrains of host grains and

surrounding recrystallized grains show a similar grain size, indicating that SGR was the dominant recrystallization mechanism implying that dislocation creep was active.

The greater amount of wedge-shaped deformation twins, within the host grains in the high-strain domain is accompanied by an increased frequency at 80° for misorientation angles of correlated grains (Bestmann et al., 2000; Burkhard, 1993).

The microstructure of the fine grained ultramylonite is characterized by (1) an extremely small grain size, (2) grain boundary triple junctions with nearly 120° angles (Fig.2.5k, l), (3) a weak CPO with very low texture index ($J = 1.4$) and (4) a random misorientation distribution curve. The preferential location of small grains next to the ultramylonitic layer (average 13 μm) showing a greater amount of small bulges, indicates that the fine-grained ultramylonite developed at the expense of the ultramylonite. These observations can result from two different deformation behaviours for the development of the fine-grained ultramylonitic layers. The fine grain size could result from brittle grain-size reduction followed by cataclastic flow, leading to the randomization of the misorientation distribution. Subsequent annealing of the microstructure could result in the development of a weak CPO. The second behaviour would be grain-size reduction by bulging (BLG) recrystallization during dislocation creep, followed by a grain-size sensitive (GSS) deformation mechanism, such as grain-boundary sliding (GBS). Again, a random misorientation distribution would be generated and at the same time, minor dislocation creep would have produced the observed weak CPO. Since we do not see any positive evidence for brittle deformation in the microstructure, but small bulges at grain boundaries of ultramylonitic grains, we assume BLG recrystallization to be the more likely mechanism. The greater strain-rate at the location of maximal displacement may have caused the switch from SGR to BLG at the same metamorphic conditions.

The dependence of the dynamic recrystallization mechanism on strain rate and temperature is well described for quartz (Hirth and Tullis, 1992; Stipp et al. 2002; Stipp and Kunze, 2008). Especially, GBM, SGR and BLG are activated in quartz aggregates with increasing strain rate and decreasing temperature (Stipp et al., 2002). For calcite such a clear characterization is missing. Nevertheless an increase in GBM activity occurs with increasing temperature and increasing strain (Schmid et al., 1987, Barnhoorn et al.,

2004). The occurrence of SGR and BLG seems to be more simultaneously although BLG is less common in calcite (Pieri et al., 2001; Barnhoorn et al., 2004). Here, we can directly link the activation of BLG recrystallization to an increase in strain rate.

We infer that the fine grain size and random misorientation distribution curve for fine-grained ultramylonitic layers means that the dominant deformation mechanism was GSS flow where grain-boundary sliding (GBS) was active and probably accommodated most of the strain (Schmid et al., 1987; Fliervoet, 1997; Bestmann and Prior, 2003). Nevertheless, GBS behaviour necessitates at least one more deformation mechanism to avoid overlaps between blocking grains and the formation of voids. In this particular case, we infer that the observed weak CPO indicates that minor dislocation creep was active with GBS.

The deformation behaviour of calcite at greater strain rates is comparable with the one at intermediate strain rates. SGR recrystallization seems to be the most common recrystallization mechanism over a wide strain rate range resulting in the formation of ultramylonitic layers. Nevertheless, different gliding systems can be activated with increasing strain rates leading to the formation of a different texture (Fig.2.8). Additionally, BLG recrystallization became more prevalent at greater strain rates, resulting in a smaller grain size for which GSS mechanisms are activated. The main observations from microstructures, textures, deformation- and recrystallization mechanism are illustrated in Figure 2.10. The microfabrics are linked to estimated strain and strain rates with the potential to act as a reference and standard for natural systems and also, serving as a comparison for experimental deformation results.

2. Strain rate dependent calcite microfabric evolution – an experiment carried out by nature




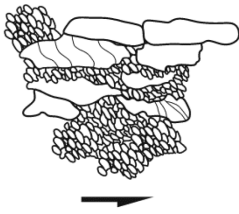






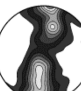


microstructure	average grain size	deformation mechanism	SPO recrystallized grains	c axis orientation	strain rate
	218 μm	dislocation creep (GBM)			$\dot{\gamma}=10^{-12.5} \text{ s}^{-1}$
	52 μm	twinning, dislocation creep			$\dot{\gamma}=10^{-11.5} \text{ s}^{-1}$
	10 μm	dislocation creep (SGR)			$\dot{\gamma}=10^{-11.5} \text{ s}^{-1}$
	68 μm	twinning, dislocation creep			$\dot{\gamma}=10^{-10.5} \text{ s}^{-1}$
	13 μm	dislocation creep (SGR)			$\dot{\gamma}=10^{-10.5} \text{ s}^{-1}$
	3.3 μm	(BLG) GBS			$\dot{\gamma}=10^{-9.5} \text{ s}^{-1}$

Figure 2.10

Table of microfabric characteristics of low-, intermediate- and high strain domains. Data in the first row have been mirrored with respect to the corresponding thin section in order to display all data in the same reference frame.

2. 5.3 Comparison with experimental calibrations

A differential stress-grain size deformation-mechanism map for marble has been calculated using grain-size insensitive (GSI) calcite flow laws for dislocation creep (Renner et al., 2002) and GSS creep (Herwegh et al., 2003), which represents a combination of diffusion creep and GBS (see appendix A2.2). Based on the observed microfabrics and the top-to-the-East shear associated with the second metamorphic event on Syros, a deformation temperature corresponding with lower greenschist-facies conditions is used (300 °C). The boundary between the GSS and the GSI field, which can be considered to correspond to stabilization of the grain size at values balancing GSS and GSI creep (De Bresser et al., 1998; 2001) was calculated and added to the map. Additionally, the paleowattmeter for calcite (Austin and Evans, 2009) and the paleopiezometers (Schmid,

1980; Rutter, 1995) linking stable grain size and differential stress are plotted (Fig.2.11). Further information on used calibrations is given in the appendix A2.2.

The differential stress and strain rate conditions of the different microstructures are determined by assuming that the average grain size of the fine grained ultramylonite represents a stable grain size. At a grain size of about 3 μm , both paleowattmeter and field boundary are consistently indicating a differential stress of 200 MPa. Differential stress conditions suggested by the paleopiezometer of Schmid (1980) are slightly less at around 170 MPa. The differential stress conditions corresponding to the remaining microfabrics are determined using the strain-rate ratios and the grain sizes of the microstructures observed within the different strain domains. For the stable grain size of the intermediate-strain domain (10 μm), the calculated differential stress conditions vary significantly depending on the chosen paleo-piezometer/-wattmeter. The field boundary and the paleopiezometer of Schmid (1980) are consistent with our results, indicating a differential stress of around 45 MPa while the paleowattmeter and the paleopiezometer by Rutter (1995) for SGR suggest greater values of around 75 MPa and 150 MPa, respectively. Differential stresses for the low -strain domain calculated by the paleopiezometer of Rutter (1995) for GBM agree with our values of around 25 MPa.

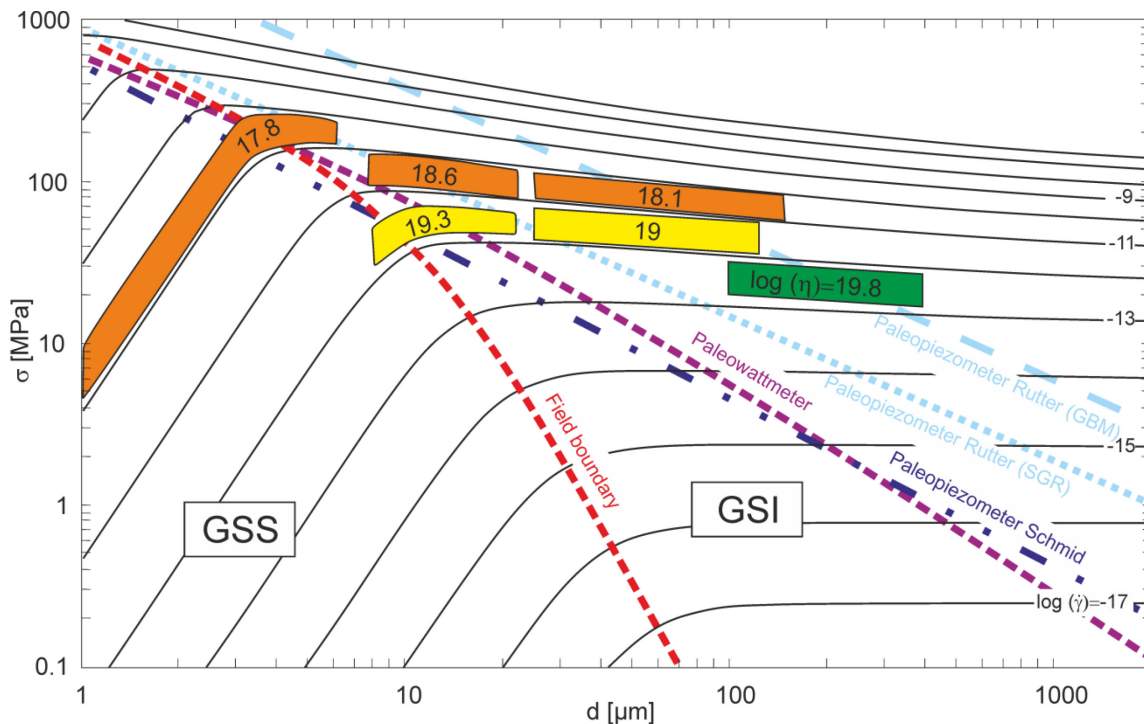


Figure 2.11

Recrystallized grain-size evolution in the low-strain (green), intermediate-strain (yellow) and high-strain (orange) domains plotted in a grain-size- vs. differential-stress deformation-mechanism map for calcite at 300 °C. Additionally the calcite paleowattmeter (Austin and Evans, 2009), the calcite paleopiezometers (Schmid, 1980; Rutter, 1995) and the viscosities for the corresponding mean grain sizes are given with the logarithmic scale. Flow laws by Renner et al. (2002) for GSI and Herwegh et al. (2003) for GSS creep. The isolines represent constant strain rates.

Consistent with our microstructural observations, deformation starts within the dislocation creep field (Fig.2.11; GSI) in all three strain domains. Progressive deformation at constant strain rates, decreases grain size, shifting the resulting grain size range closer to the field boundary. Decreasing grain size induces increasing viscosity at about 100.5 Pa s, within the high- and intermediate-strain domains. This changing viscosity for constant strain rates indicates minor strain hardening during the dislocation creep. This evolution is consistent with the observed change from reverse to normal drag next to the CE, where the CE would have been widening during rotation and slip (Means, 1995; Pennacchioni and Mancktelow, 2007). Within the high-strain domain, the grain size decreases even further so that a GSS deformation mechanism is activated. The switch in deformation regime leads to strain softening as indicated decreasing viscosity with increasing strain rate. This softening evolution is consistent with extreme localization of the deformation in the fine-grained ultramylonite (Bestmann et al., 2000).

In the ultramylonite, calculated shear-strain rate values are between $10^{-9.5}$ and 10^{-10} s^{-1} . The calculated strain rate for the background shear, leading to the rotation of the cross-cutting element is around $10^{-12.5} \text{ s}^{-1}$, which lies at the higher bound of typical strain rates in shear zones at crustal levels (Pfiffner and Ramsay, 1982).

These predictions about deformation strain rates and differential stresses are in agreement with a deformation temperature of 300 °C. Deformation at higher temperatures would result in an unexpectedly high background shear-strain rate of around 10^{-11} s^{-1} , a value which is too great considering the small amount of intracrystalline deformation. Lower deformation temperatures would favour deformation in the ductile-brittle transition zone which we do not believe occurred given the preserved microstructures in the study area.

Our observations show that the field boundary theory as well as the calcite paleowattmeter (Austin and Evans, 2009) and the paleopiezometer of Schmid (1980) can be extrapolated to natural examples deformed at strain rates $> 10^{-12} \text{ s}^{-1}$. At lesser strain rates, the paleowattmeter seems to underestimate conditions. In contrast the paleopiezometer of Rutter (1995) for SGR seems to result in slightly overestimated values while the one for GBM is consistent with our observations.

2.6. Conclusions

We used a flanking structure as a natural laboratory for studying the microfabric and effective deformation mechanisms of nearly pure calcite marble for lower greenschist facies conditions ($\sim 300 \text{ °C}$) and different strain rates (10^{-12} to 10^{-9} s^{-1}). Natural strain-rates and grain sizes were compared with experimentally determined flow laws, paleowatt- and paleopiezo-meters, resulting to the following conclusions.

(1) The recrystallization mechanism of calcite changed with increasing strain rate from grain-boundary migration (GBM) to subgrain rotation (SGR) and finally bulging (BLG) recrystallization. SGR seems to be, however, the dominant recrystallization mechanism over a wide range of strain rates. The switch in recrystallization mechanism is accompanied by a decrease in grain size.

(2) Strain progressively localizes along fine-grained layers. Ultramylonitic layers evolve from mature core-mantle structures by SGR while fine-grained ultramylonitic layers developed from ultramylonitic layers by BLG recrystallization.

(3) The change of calcite textures indicate that activation of different gliding systems depends on different strain rates.

(4) Laboratory-determined flow laws for GSI creep (Renner et al., 2002) and GSS creep (Herwegh et al., 2003) are consistent with our observations regarding the activity of different creep regimes and the predictions for the evolution of hardening and softening at constant strain rates.

(5) Paleostress calculated with the paleowattmeter of Austin and Evans (2009) and the paleopiezometer of Schmid (1980) give reliable results for calcite deformed at strain rates faster 10^{-12} s^{-1} . In contrast, the paleopiezometer of Rutter (1995) for SGR recrystallization seems to predict overestimated values.

(6) The results of this study are only valid for the lower greenschist facies and high strain rates (10^{-12} to 10^{-9} s^{-1}). More work using well constrained natural high-strain calcite rocks at higher grade is needed to extend the validity of experimental calibrations at natural strain rates.

Appendix 2

A2.1 Background shear-strain calculation

In this appendix, we derive a relationship between the amount of finite strain and the kinematic vorticity number for the outcrop. Isovolumetric plane strain is assumed so that the finite strain tensor within the shear zone reference framework can be written as a function of two positive unknown parameters: the longitudinal strain along the shear zone, k , and the shear strain along the shear zone, Γ

$$D = \begin{bmatrix} k & \Gamma \\ 0 & 1/k \end{bmatrix}. \quad (\text{Eq. 2.3})$$

The crosscutting element formed as a crack initially perpendicular to the foliation plane, which is assumed to be parallel to the stretching eigenvector of finite strain (Fig.A2.1a). In the Mohr space, the initial direction the crack corresponds to the point CE and the direction of the stretching eigenvector corresponds to the point A_1 . Since these directions were initially perpendicular, A_1 and CE are opposite points on the same diameter of the finite-strain Mohr circle of second kind (De Paor and Means, 1984; Fig.A2.1b). Their coordinates are respectively $A_1: (0, k)$ and CE: $(\Gamma, 1/k)$.

The crosscutting element has rotated by an angle β that we can deduce from field measurements of the angle between the rotated crosscutting element and the foliation plane. Therefore, the point CE is at the intersection between the finite strain Mohr circle and the line $x = y \tan \beta$ (Fig.2.A1b). This gives us a relationship between k and Γ :

$$\Gamma = \tan \beta / k, \quad (\text{Eq. 2.4})$$

so that the coordinates of point CE are $(\tan \beta / k, 1/k)$. They are used for calculating the diameter of the finite-strain Mohr circle as the distance between points A_1 and CE:

$$d = \frac{\sqrt{\tan^2 \beta + (k^2 - 1)^2}}{k}. \quad (\text{Eq. 2.5})$$

The diameter of the finite-strain Mohr circle is used as a proxy for strain in general shear since it is exactly equal to Γ in simple shear and it is equal to $k - 1/k$ in pure shear.

Using geometry of the finite-strain Mohr circle, we can determine the coordinates of the center of the Mohr circle C: $(\tan \beta / 2k, (k^2 + 1) / 2k)$ and the point corresponding to the shortening finite strain eigenvector A2 : $(0, 1/k)$. The angle between the two eigenvectors in the Mohr space is 2α , where α is the angle between the two eigenvectors in the physical space. The value of $\cos 2\alpha$ can be calculated using a scalar product in the Mohr space between the vectors

CA_1 and CA_2 divided by their norms:

$$\cos 2\alpha = \frac{\tan^2 \beta - (k^2 - 1)^2}{\tan^2 \beta + (k^2 - 1)^2}, \quad (\text{Eq. 2.6})$$

where equation 5 has been used for calculating the norms of the vectors. The kinematic vorticity W_k is then calculated following Bobyarchick (1986):

$$\begin{aligned} W_k &= \cos \alpha = \sqrt{\frac{1 + \cos 2\alpha}{2}}, \\ &= \sqrt{\frac{\tan^2 \beta}{\tan^2 \beta + (k^2 - 1)^2}}. \end{aligned} \quad (\text{Eq. 2.7})$$

Finally, even though the value of k remains unknown (i.e. the Mohr circle is not scaled), it is possible to plot the diameter of the finite-strain Mohr circle in an equation as a function of the kinematic vorticity. Equation 2.7 is used for calculating:

$$(k^2 - 1)^2 = \frac{\tan^2 \beta}{W_k^2} - \tan^2 \beta, \quad (\text{Eq. 2.8})$$

and

$$k = \sqrt{1 + \tan \beta \sqrt{1/W_k^2 - 1}}. \quad (\text{Eq. 2.9})$$

Equations 2.7 and 2.8 are introduced into equation 2.5:

$$d = \frac{\tan \beta}{W_k \sqrt{1 + \tan \beta \sqrt{1/W_k^2 - 1}}}. \quad (\text{Eq. 2.10})$$

Figure A1c represents the graph of d as a function of W_k using the average value of the cross-cutting element rotation: $\beta = 70^\circ$. It shows that the bulk strain in the shear was less than 3, if the kinematic vorticity number was larger than 0.29. Therefore, even if the pure shear component responsible for the observed deformation was large, the amount of bulk strain was most likely limited to values comprised between 2 and 3. Larger values of bulk strain would have “erased” the flanking structure.

2. Strain rate dependent calcite microfabric evolution – an experiment carried out by nature

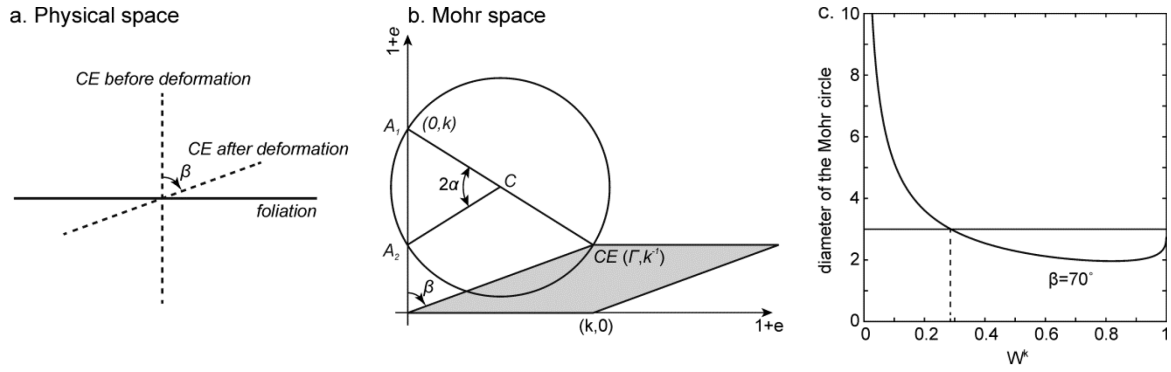


Figure A2.1

a. Orientation of the crosscutting element (CE) with respect to the foliation before and after deformation, in the physical space. b. Mohr circle of the second kind showing the orientation of the finite strain eigenvectors (A_1 and A_2) and the crosscutting element. c. Diameter of the finite strain Mohr circle as a function of the kinematic vorticity W^k .

A2.2 Experimental calibrations

For the calculation of the deformation mechanism map, we used the composite flow law after Ter Heege et al. (2004). The diffusion creep field was calculated applying the flow law by Herwegh et al. (2003) that represents a combination of diffusion creep and grain-boundary sliding

$$\dot{\gamma}_{GSS} = A \sigma^n d^{-m} \exp(-Q/R/T), \quad (\text{Eq. 2.11})$$

with $n=1.1$, $m=3.3$, an activation energy $Q=200$ kJ/mol and $A= 4.3 \times 10^7$.

For the dislocation creep field, we used the flow law by Renner et al. (2002) that is well suited for low-temperature data (De Bresser et al., 2002).

$$\dot{\gamma}_{GSI} = A \sigma^n \exp(\sigma/\sigma_0) \exp(-Q/R/T), \quad (\text{Eq. 2.12})$$

with $n=2$, $Q= 200$ kJ/mol and $A= 270$. σ_0 calculated by the formula

$$\sigma_0 = (\sigma + 115 d^{0.5}) (T_m - T) / 1000, \quad (\text{Eq. 2.13})$$

where T_m is the melting temperature and d the grain size.

Stresses were calculated with the paleopiezometer of Rutter (1995) for subgrain rotation recrystallization

$$\sigma = 10^{2.91} * d^{-0.88}, \quad (\text{Eq. 2.14})$$

and for grain-boundary migration recrystallization

$$\sigma = 10^{3.43} * d^{-0.89}, \quad (\text{Eq. 2.15})$$

and the paleopiezometer of Schmid (1980)

$$\sigma = 10^{2.69} * d^{-1.02}, \quad (\text{Eq. 2.16})$$

In all equations, σ is the differential stress and $\dot{\gamma}$ the strain rate, R represents the gas constant and T the deformation temperature in K.

3. Strain localization in ultramylonitic marbles by dislocation activity accommodated grain boundary sliding (Syros, Greece)

Abstract

We observed extreme strain localization in the center of the cross-cutting element of a flanking structure, developed in almost pure calcite marbles. At the maximum displacement along the cross-cutting element (120 cm) evidence of grain size sensitive deformation mechanisms can be found in the ultramylonitic marbles, which are characterized by (1) an extremely small grain size (3 μm), (2) grain boundary triple junctions with nearly 120° angles, (3) a weak CPO with very low texture index ($J = 1.4$), (4) a random misorientation angle distribution curve and (5) the presence of small cavities at triple junctions. We performed high resolution analyses via transmission electron microscopy and observed recrystallization by bulging resulting in the development of the fine grained ultramylonite. High dislocation densities and abundant Frank-Read sources indicate high dislocation activity. The arrangement of dislocations in the extremely fine grain sized calcite differs from the one created by classical dislocation creep mediated by combined glide and thermally activated climb or cataclastic flow. It rather exhibits grain boundary sliding accommodated by cross-slip and network assisted dislocation movement without formation of idealized subgrain walls. The switch from dislocation creep to grain boundary sliding results in strain softening and can be an important strain localization process in calcite rocks, even at high strain rate (10^{-9} s^{-1}) and low temperature (300 °C).

Chapter 3. is based on:

Rogowitz, A., Grasemann, B. and White J.C. Strain localization in ultramylonitic marbles by dislocation activity accommodated grain boundary sliding (Syros, Greece). Manuscript in preparation.

3.1 Introduction

Strain localization in monomineralic rocks is often associated with brittle precursors, resulting in stress and strain concentration, followed by grain size reduction and activation of grain size sensitive deformation mechanism like diffusion creep, cataclastic flow and grain boundary sliding (Schmid, 1976; Schmid et al., 1977; Etheridge and Wilkie, 1979; Pennacchioni and Mancktelow, 2007; Menegon et al., 2013). The aforementioned mechanisms typically tend to result in a random crystallographic orientation or decrease in intensity of a pre-existing texture. However, reports of fine grained polycrystalline materials showing a preferred crystallographic orientation indicate that subsequent static annealing or the activation of additional deformation mechanisms during grain boundary sliding (GBS; Gifkins, 1976; Schmid et al., 1977; Rutter et al., 1994; Sundberg and Cooper; 2008; Wang et al., 2010).

In order to maintain strain compatibility during GBS a different mechanism has to operate simultaneously (Fig.3.1). Beside Coble creep, dislocation glide and climb within the grain boundary and the grain boundary region have been observed (Gifkins, 1976). More recently the simultaneous activity of dislocation creep and GBS has been reported to be active in ultramylonites deformed at high temperatures (Wang et al., 2010).

In this contribution, we present observations from an almost pure calcite marble layer from Syros (Cyclades, Greece) deformed under lower greenschist facies conditions (Rogowitz et al., 2014). The presence of a crack (i.e. cross-cutting element) that rotated during shear resulted in the formation of a flanking structure. At location of maximum displacement along the cross-cutting element (120 cm) the marble is extremely fine grained (3 μm) supporting deformation by grain size sensitive mechanisms. The observed grain size has been plotted in a differential stress-strain rate deformation mechanism map for calcite at 300 °C showing that maximum strain rates of 10^{-9} s^{-1} have been reached. At such fast strain rates and low temperatures the activation of brittle deformation rather than ductile flow would be expected.

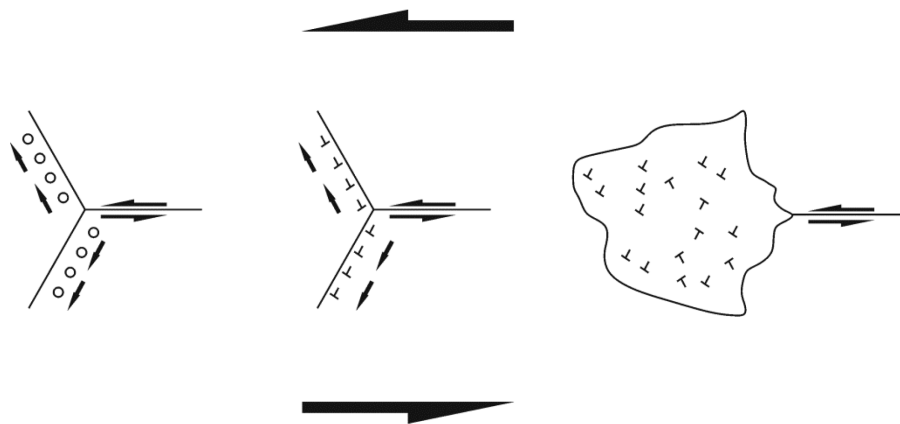


Figure 3.1

Sketch showing additional strain accommodating mechanism active during grain boundary sliding (modified after Gifkins, 1974; Ree, 1994). From left to right: coble creep, dislocation movement in grain boundaries and grain boundary area, dislocation creep.

In the following we are going to present and discuss the microstructure of the investigated ultramylonite. Detailed analysis have been performed using optical microscopy, secondary electron microscopy (SEM), electron backscatter diffraction (EBSD) mapping and transmission electron microscopy (TEM) in order to get an accurate idea of deformation mechanism active at the given temperature, stress and strain rate conditions.

3.2 Geological setting and Outcrop description

The analyzed ultramylonite is the result of the development of an a-type flanking structure in an almost pure calcite marble situated on Syros, which is one of the Cycladic Islands that are located in the back arc of the Hellenic subduction zone (Papanikolaou, 1987; Wortel et al., 1993). In general the Cycladic area has been affected by 2 main metamorphic events: (1) an Eocene eclogite-blueschist metamorphic event and (2) an Oligo-Miocene greenschist-facies event (Jolivet and Brun, 2010). The exposed rocks on Syros are mainly belonging to the cycladic blueschist unit (CBU), which is dominated by metagabbros, metabasites, metasediments and schists. Numerous petrological studies have been performed on the rocks of Syros in order to get constraints on the P-T evolution of Syros, resulting in peak conditions of around 18 kbar and 550 °C (Trotet et

al., 2001b; Keiter et al., 2004). The greenschist facies overprint is assumed to take part at conditions around 300 °C and 2 to 4 kbar (Trotet et al., 2001b; Keiter et al., 2004; Schumacher et al., 2008). In general an increase in greenschist facies overprint towards the SW of Syros can be observed attended by a NE-SW stretching lineation and a top-East sense of shear (Keiter et al., 2004; Philippon et al., 2011).

Due to the rotation of a crack, initially orientated at an angle of 90° to the main foliation, during greenschist facies overprinting, an antithetic shear zone developed. In its center the cross-cutting element has a maximum displacement of 120 cm and the initially coarse grained, almost pure calcite marble is recrystallized to an extremely fine grained ultramylonite (Fig.3.2) with a porcelain-like macroscopic appearance. The ultramylonitic layers have a total thickness of 0.12-0.48 cm and border the cross-cutting element that is built up of alternating protomylonitic and ultramylonitic calcite layers, having a total thickness of 1.5 cm (Rogowitz et al., 2014). Assuming that the marble deformed under simple shear conditions the total strain at this locality is at least 80. If we assume furthermore, that most of the strain was accommodated by the fine grained ultramylonite, we reach a shear strain up to 1000. This high value is clearly an upper limit but not unrealistic taking the extremely fine grain size into account.

3.3 Methods

3.3.1 Sample preparation

The sample was cut perpendicular to the shear-zone boundary and parallel to the stretching lineation (xz plane). Mechanically polished thin-sections with a thickness between 20 and 30 µm were prepared for microstructure analysis. Samples of special interest have been selected for SEM and EBSD analysis and been chemo-mechanically polished with an alkaline colloidal silica suspension (Köstrosol 3530; pH 9.2-10). To establish electric conductivity the samples were carbon coated.

Specimens for TEM have been prepared by the focused ion beam technique (FIB) and the precision ion polishing system (PIPS).

In order to characterize dislocation development and behavior during progressive deformation of the fine-grained ultramylonitic layer, FIB-foils showing a profile across small calcite grains within the transition zone between coarser grained marble and the

fine grained ultramylonite, have been made. This allows us to compare the dislocation structure within new developed grains and once that have been further deformed within the layer of focus. For analysis of dislocation structures within the ultramylonitic calcite FIB-foils showing a profile over at least two grains have been prepared. Additionally PIPS was used to prepare specimens in order to get an overview across a larger area.

3.3.2 Microfabric analysis

A Leica DM4500 P optical microscope has been used for selecting appropriate samples for detailed microfabric analysis. In order to visualize the presence of cracks and cavities secondary electron microscopy has been performed on a FEI Quanta 3D FEG instrument equipped with an EDAX Pegasus Apex 4 system consisting of a Digiview IV EBSD camera and an Apollo XV silicon drift detector for EDX-spectrometry at the University of Vienna, department of lithospheric research (Fig.3.3). Crystallographic orientations have been measured by combined electron backscatter diffraction (EBSD) mapping and EDX-spectrometry. The instrument has been operated with a 10 kV accelerating voltage, a 4nA probe current at working distances between 10 and 14 mm. For EBSD analysis the sample has been tilted up to an angle of 70°.

The MATLAB toolbox for quantitative texture analysis MTEX (Bachmann et al., 2010) has been used for processing the EBSD data. Orientation distribution functions (ODFs) were calculated after Bunge (1982). The orientation of the c (0001), -a <11-20>, r {10-14}, f {01-12}, e {01-18} and m {10-10} poles were derived from the ODF and plotted as equal area lower hemisphere projections (Fig.3.4a). Additionally the misorientation-angle distributions for neighbour-pair and random-pair grains have been detected and are represented together with the calculated theoretical, random misorientation-angle distribution for trigonal crystal symmetry (Fig.3.4b; Mackenzie and Thompson, 1957).

Transmission electron microscopy (TEM) has been performed at a JEOL 2011 equipped with a double-tilt analytical holder and a Gatan MSC digital camera for imaging at the University of New Brunswick, department for earth science. The TEM has been operated at an accelerating voltage was set at 200 keV in bright- and dark-filed mode (Fig.3.5, 3.6).

3.3.3 Dislocation density estimation

Dislocation densities have been measured by use of the line-cut method. The number of intersections between dislocations and a prescribed grid of traverse lines has been counted. The dislocation density ρ was then determined using:

$$\rho = 2N/Lt, \quad (\text{Eq. 3.1})$$

with t being the specimen thickness, N the number of counted intersections and L the total length of the used grid.

32 random chosen TEM bright field images have been used in order to get a representative result. Dislocation densities have been calculated for an average, maximum and minimum specimen thickness (Fig.3.7).

3.3.4 Stress calculation

The theoretical relation between dislocation density and stress has been used to get estimation on flow stress conditions σ (Kohlstedt and Weathers, 1980):

$$\sigma = \alpha \mu b \rho^{0.5}, \quad (\text{Eq. 3.2})$$

Where α is a constant depending on the type of dislocation, μ is the shear modulus and b is the burgers vector length. Calculations have been done with $\alpha = 1$ and $\mu = 28.9$ GPa (for calcite at 300 °C; Dandekar, 1968). Values for the burgers vector length vary depending on the chosen slip plane (4.98 Å, 6.37 Å, and 8.09 Å) depending on the chosen glide system (Goetze and Kohlstedt, 1977). Flow stresses have been calculated using dislocation densities ρ calculated for maximum, minimum and average specimen thickness. Additionally the experimental calibration of De Bresser (1996) linking flow stress and dislocation density has been used:

$$\sigma = 10^{-6.21} \rho^{0.62}. \quad (\text{Eq. 3.3})$$

Although this equation is based on results from single crystals it is assumed to fit for polycrystalline material deformed at higher differential stresses (> 40 MPa). The results obtained for average specimen thickness have been plotted against the dislocation density in a logarithmic plot (Fig.3.8).

3.4 Results

3.4.1 Microfabric

The analyzed ultramylonitic marble is characterized by extremely fine grained, almost equigranular calcite with an average grain size of $3\ \mu\text{m}$ (Fig.3.2a). Locally triple junctions and five-to six-grain junctions with a small round grain located in the center occur. Minor coarser left over grains appear to have more curved grain boundaries (Fig.3.2b), especially at the boundary towards a coarser grained layer a higher amount of small bulges can be observed.

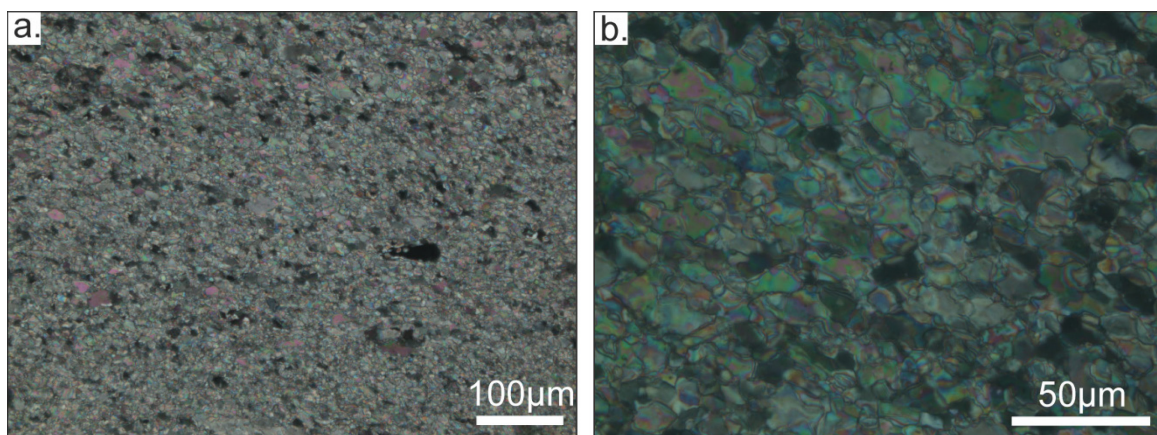


Figure 3.2

a. Optical micrograph (crossed polarizers) showing fine-grained ultramylonite. b. Optical micrograph (crossed polarizers) showing close up of fine grained ultramylonite. Note that grain boundaries of coarser grains are strongly curved compared to smaller grains.

Small cavities with a size up to $1\ \mu\text{m}$ are located at grain-triple and four-grain junctions (Fig.3.3a-d). Additionally small, elongated grain boundary openings preferentially orientated at grain boundaries in extension can be observed (Fig.3.3e, f). Small cracks orientated at approximately the same angle are piling up at grain boundaries orientated

with a high angle to the foliation (Fig.3.3g, h). Such structures also known as Zener-Stroh cracks are assumed to be the result of dislocation pile up (Yoo and Trinkaus, 1983; Kassner and Hayes, 2003).

The ultramylonitic calcite grains show a weak crystallographic preferred orientation (Fig.3.4a; max. J-Index 1.4) with a c-axis orientation at the periphery of the pole figure and a point maximum orientated oblique to the foliation plane. The poles of e-planes follow the trace of the c-axis showing a similar preferred orientation. a-axes and poles of m-planes are preferentially orientated in a slightly oblique girdle within the foliation plane, orientated almost perpendicular to the c-axis point maximum, showing one point maximum in the center of the pole figure. The poles of r-planes show 4 extremely weakly defined point maxima of which one is almost perpendicular to the foliation plane.

Misorientation angle distributions of neighbour-pair and random-pair grains are almost identical and follow the calculated curve of an ideal random misorientation-angle distribution calculated for trigonal crystal symmetry (Fig.3.4b).

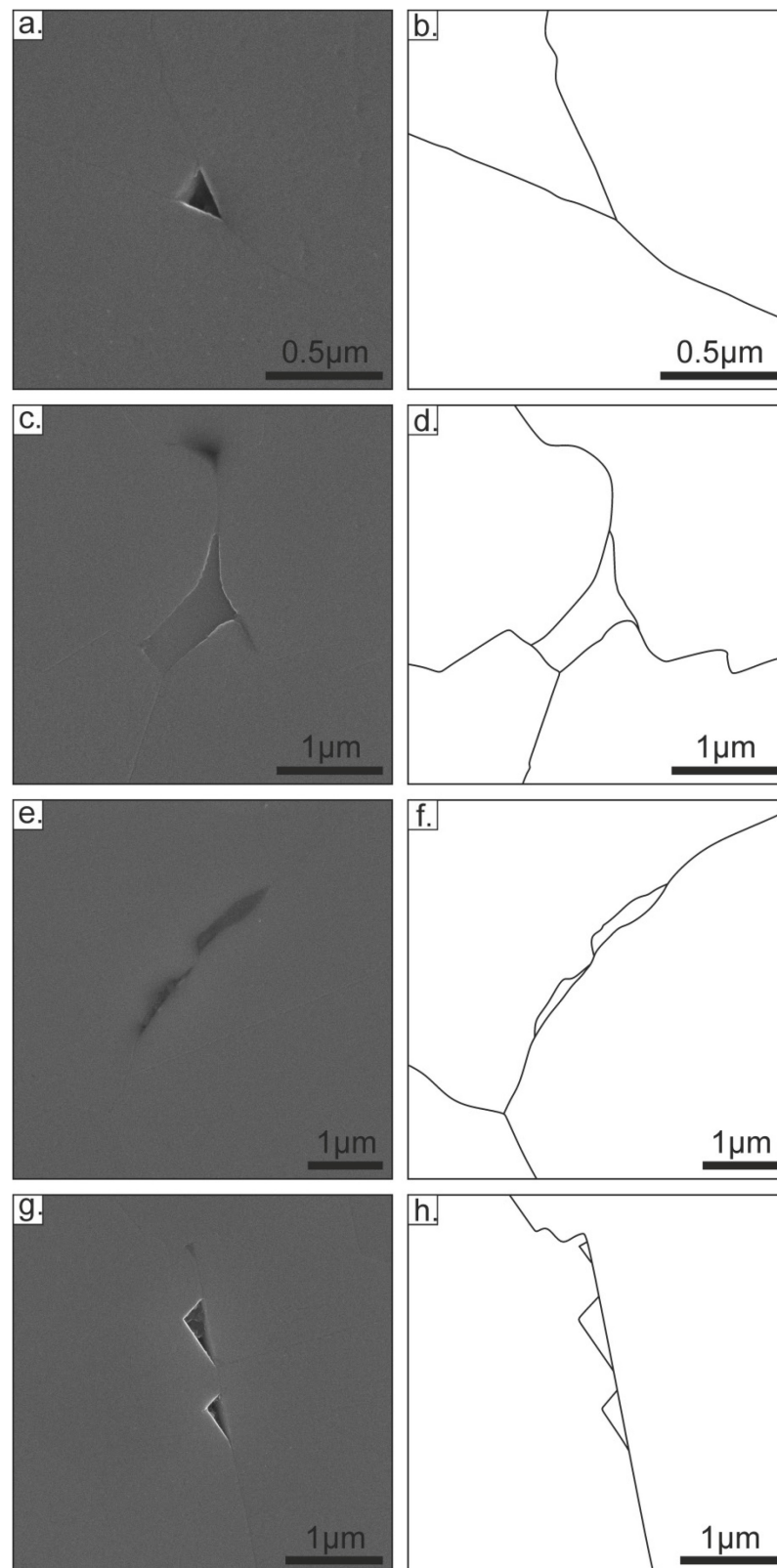


Figure 3.3

Secondary electron images showing preferred locality of cavities in fine grained ultramylonite (a, c, e, g). The sketches represent grain boundary drawings of the areas respectively (b, d, f, h). a, b. Small cavity at grain boundary triple junction. c, d. Cavity located at four-grain junction. e, f. Grain boundary opening at grain boundary in extension. g, h. Zener-Stroh cracks due to dislocation pile up at the grain boundary. Note that the three small cracks show the same orientation.

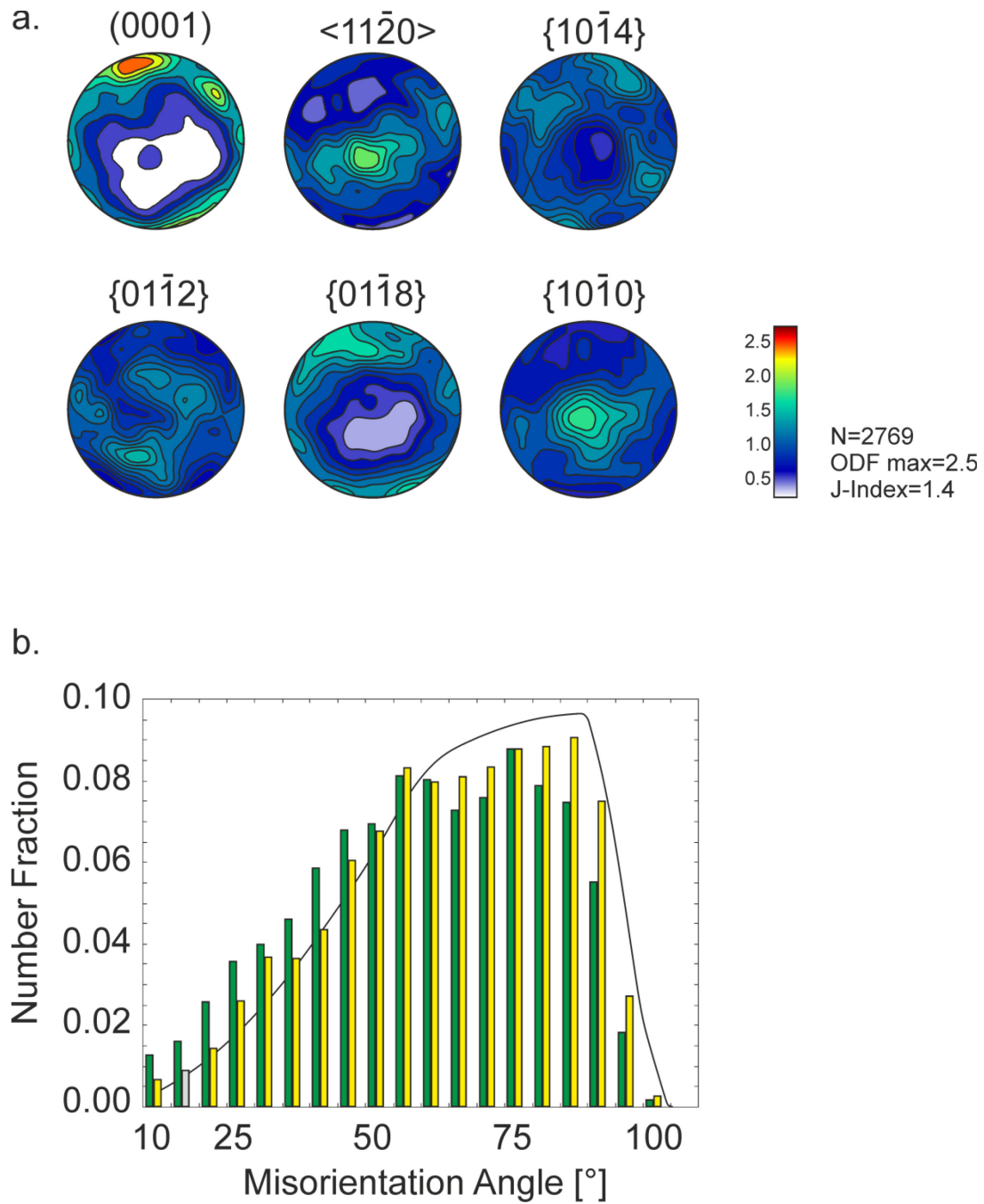


Figure 3.4

a. Stereographic equal area lower hemisphere projection of c (0001) and $-a$ $\langle 11\bar{2}0 \rangle$ axes and poles of r $\{10\bar{1}4\}$, f $\{01\bar{1}2\}$, e $\{01\bar{1}8\}$ and m $\{10\bar{1}0\}$ planes. N represents the number of analyzed grains. Texture strength is represented by the intensity of the orientation distribution function (ODF), additionally information on J-Index are given. b. Histogram showing the misorientation angle distribution of neighbor-pair (green) and random-pair grains (yellow). The curve represents the calculated theoretical curve for a perfectly random misorientation angle distribution for trigonal crystal symmetry.

3.4.2 Dislocation microstructure

Small grains located in the transition zone of coarser and fine grained ultramylonitic layer, are almost free of dislocations (Fig.3.5c, d), showing a sharp, convex high angle grain boundary (Fig.3.5b-d) towards the highly strained coarser calcite grains. The dislocation structure within the coarser grained calcite is characterized by a high amount of low angle grain boundaries defined by well-arranged dislocations walls and minor free dislocations (Fig.3.5c, d).

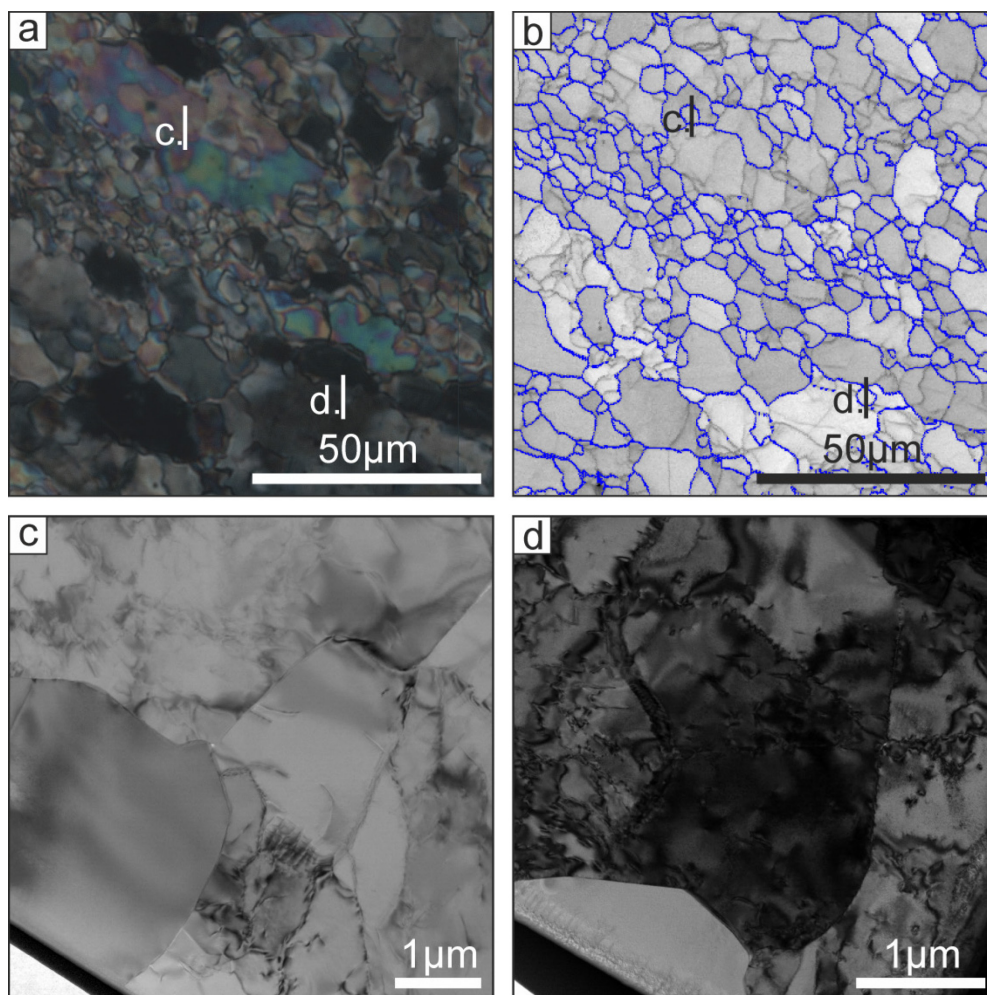


Figure 3.5

a. Optical micrograph (crossed polarizer) showing the transition zone between coarse and fine grained ultramylonite. c. and d. represent the locality of FIB foils. b. Electron backscatter diffraction (EBSD) map showing transition zone between coarse and fine grained ultramylonite. High angle boundaries ($>15^\circ$) are plotted in blue. c. and d. show the locality of FIB foils. Note that the foils represent a profile across fine grained ultramylonitic grains adjacent to a coarse grain. c. TEM bright field image showing an almost dislocation free calcite grain next to coarser grains showing free dislocations and low angle grain boundaries. d. TEM bright field image showing an almost dislocation free calcite grain next to coarser grains showing a high amount of free dislocations and dislocations arranged to low angle grain boundaries.

Different to the coarser grained calcite there are almost no low angle grain boundaries present within the fine-grained ultramylonite, instead a high amount of free dislocations can be observed (Fig.3.6). An abundant number of Frank-Read sources located at both grain boundaries and within the center of grains can be found resulting in dislocation multiplication (Fig.3.6a, b). Locally dislocations are arranged in zigzagging lines and networks resulting in the development of small cells of around 0.2 μm in size, showing partly a hexagonal shape (Fig.3.6c, d). Locally long parallel traces of dislocations indicate activity of dislocation glide (Fig.3.6e). Nevertheless, in most cases the dislocations are arranged random without any visible preferred alignment (Fig.3.6f).

Almost all calculated dislocation densities are in an order of 10^{13} m^{-2} . The estimated densities for average specimen thicknesses are almost bell-shaped distributed with a maximum at around $5 \times 10^{13} \text{ m}^{-2}$ (Fig.3.7).

3. Strain localization in ultramylonitic marbles by dislocation activity accommodated grain boundary sliding (Syros, Greece)

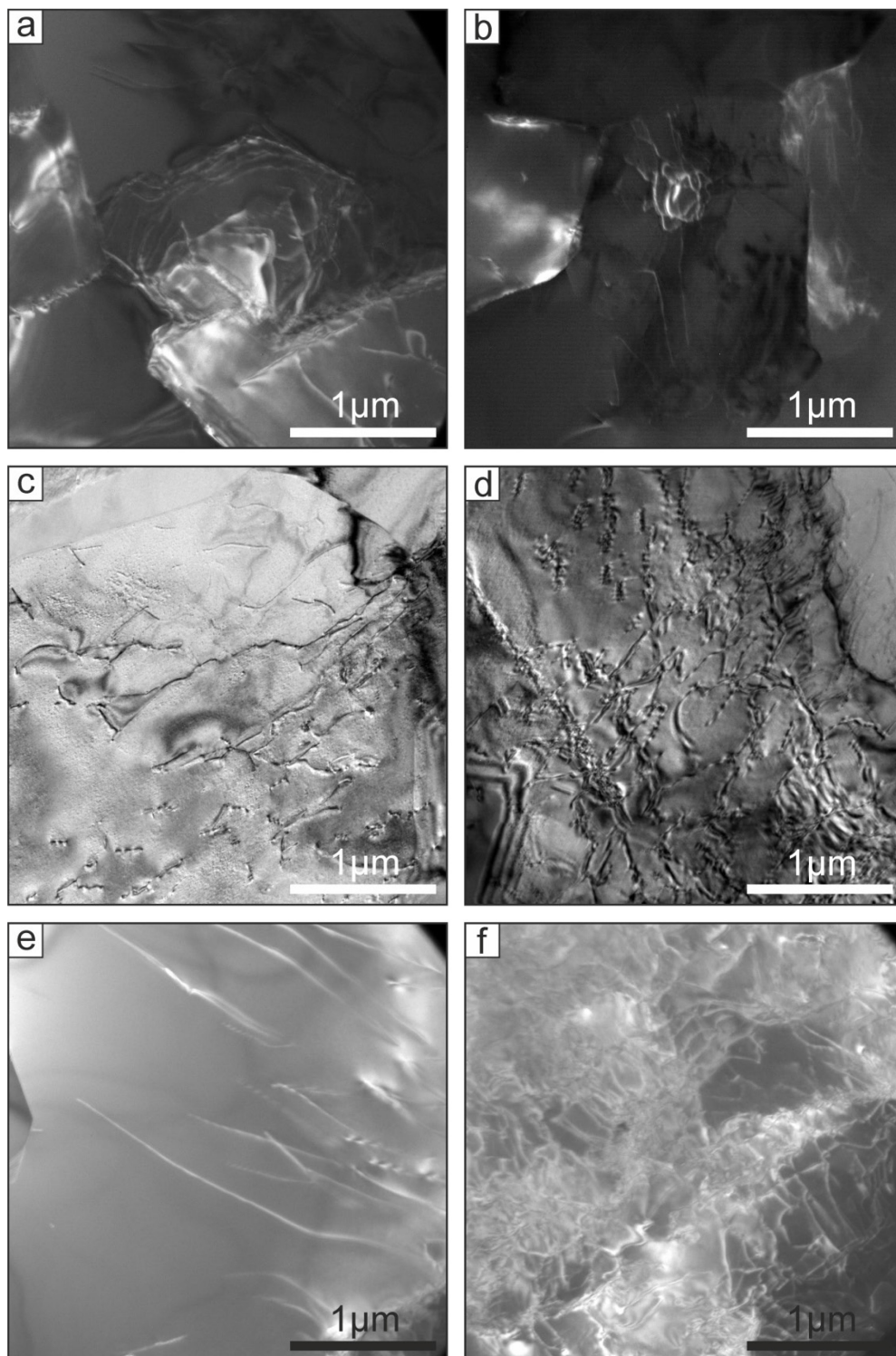


Figure 3.6

TEM bright (c, d) and dark (a, b, e, f) micrographs showing typical dislocation structures within the fine grained ultramylonite. a. Frank-Read source located next to a grain boundary. Note the great amount of free dislocations and low angle grain boundaries adjacent to the Frank-Read source. b. Frank-Read source located in the grain center. c. Free dislocations and dislocation networks arranged in small zigzagging lines. d. Dislocation networks arranged in small cells. e. Long, almost parallel arranged dislocation. f. Great amount of random arranged dislocations.

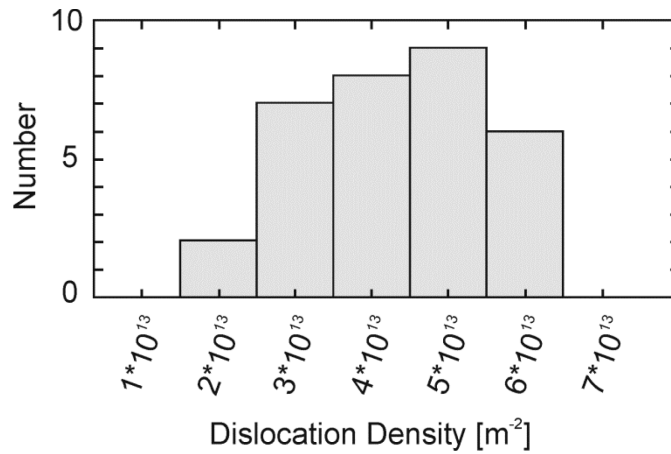


Figure 3.7

Calculated dislocation densities for an average specimen thickness represented in a histogram.

3.4.3 Stress and strain rate calculation

The calculated differential stress varies depending on the chosen active glide system and therefore the burgers vector length (Table A3.1, Fig.3.8a). Assuming that basal slip is the dominant glide system the differential stress for an average specimen thickness varies between 64 and 110 MPa, for preferred f-slip differential stresses reach values between 82 and 140 MPa, burgers vector length observed to be active for r- and f-slip results in differential stresses between 104 and 178 MPa. Using the experimental ρ – σ calibration of De Bresser (1996) even higher differential stresses are reached ranging between 133 and 260 MPa (Table A3.1, Fig.3.8b).

Differential stress calculated with the paleowattmeter (Austin and Evans, 2009) and paleopiezometer of Schmid (1980) lie in a range between 200 and 170 MPa (Fig.3.8, 3.9). These values are close to the average stresses calculated for r- and f-slip as well as average stresses calculated with the equation of De Bresser (1996; Fig.3.8b).

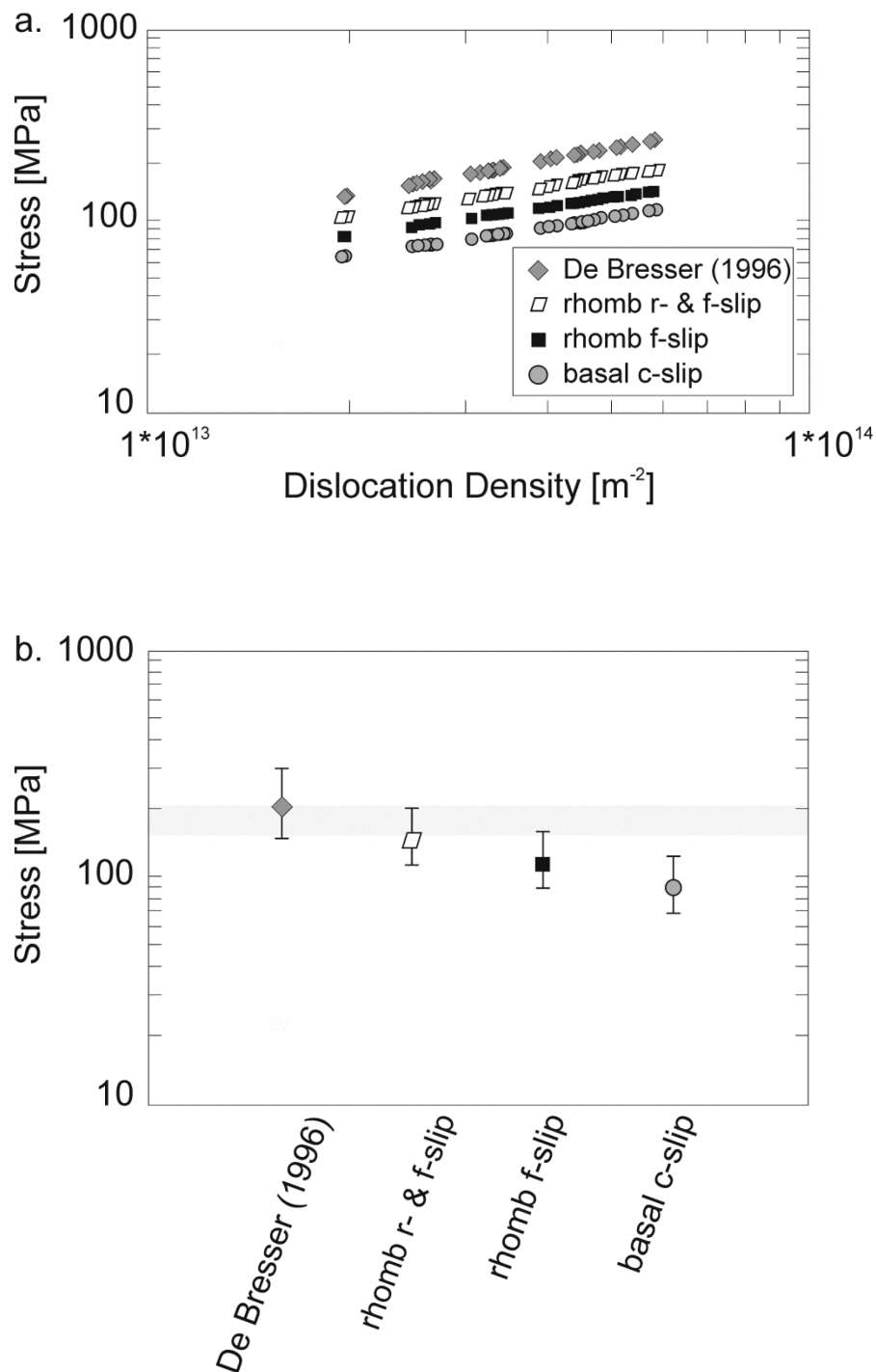


Figure 3.8

a. Logarithmic plot of calculated stress by the relation of De Bresser (1996) and for different possible burgers vector lengths versus the estimated dislocation densities. b. Logarithmic plot showing the calculated average stress values for the different used equations and glide systems. The bars represent the stress range for an average dislocation density. Gray shaded area displays the calculated stress by paleowattmeter (Austin and Evans, 2009) and paleopiezometer (Schmid et al., 1980).

In order to quantify deformation strain rates a deformation mechanism map for calcite at 300 °C has been calculated using flow laws of Herwegh et al. (2003) and Renner et al. (2002). The average grain size has been plotted with respect to the corresponding differential stress calculated by paleowattmeter and paleopiezometer (Fig.3.9) indicating active strain rates of around $10^{-9} - 10^{-10} \text{ s}^{-1}$. The observed average grain size plots exactly at the boundary between grain size sensitive (GSS) and grain size insensitive (GSI) creep consistent with the field boundary hypothesis (De Bresser et al., 1998; 2001) which is assumed to represent the balancing stable grain size between grain growth active during GSS creep and grain size reduction during GSI creep.

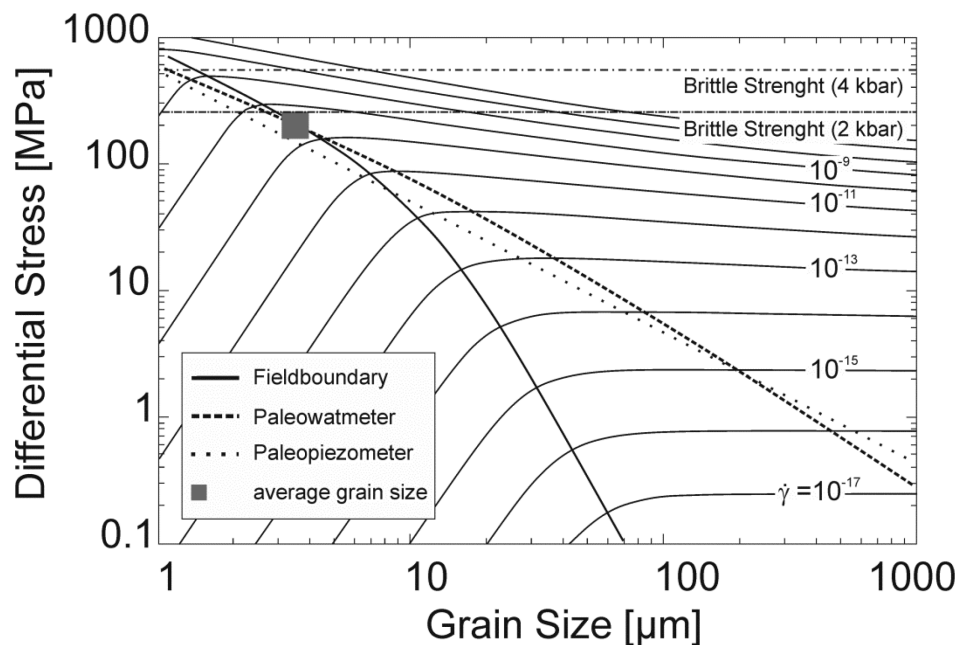


Figure 3.9

Deformation mechanism map for calcite at 300°C in the differential stress versus grain size space. Used flow laws are by Renner et al. (2002) for the dislocation creep field and Herwegh et al. (2003) for grain size sensitive creep. Additionally paleowattmeter (Austin and Evans, 2009), paleopiezometer (Schmid et al., 1980), the field boundary after De Bresser et al. (1998, 2001) and the brittle strength (Byerlee, 1978) are plotted. The rectangle represents the average grain size.

3.5 Discussion

3.5.1 Grain size reduction

Two main mechanisms are widely accepted to result in strong grain size reduction: 1. brittle deformation and 2. dynamic recrystallization by subgrain rotation (SGR) or bulging (BLG) (Etheridge and Wilkie, 1979; Handy et al., 2007). Since no positive evidence of brittle deformation has been found in the marble ultramylonites, we assume recrystallization to be the grain size reducing mechanism (Rogowitz et al., 2014). TEM analysis of small calcite grains within the transition zone between the two different sized ultramylonitic layers show an extreme low amount of free dislocations compared to adjacent coarser calcite grains. The convex curvature of the grain boundary towards highly strained grains indicates grain boundary movement from the small grain towards the coarser grain. Such a structure is typical for BLG recrystallization where the driving force for grain boundary movement is the internal strain energy (Sakai and Jonas, 1984; Platt and Behr, 2011). During grain boundary migration of the recrystallized grain, the dislocation rich grain is consumed resulting in a decrease in strain energy. The developed small grain size thus allows further strain accommodation by activation of GSS deformation mechanisms (Etheridge and Wilkie, 1979).

3.5.2 Deformation mechanism

It is known that small equigranular grains favor GSS deformation by diffusion along grain boundaries (coble creep), mass diffusion through the crystal lattice (Nabarro-Herring creep) or GBS (Raj and Ashby, 1971; Ashby and Verrall, 1973; Gifkins, 1976; Schmid, 1976; Rutter, 1994). These mechanisms are associated with strain localization and strain softening in naturally deformed rocks. Usually the activation of GSS deformation mechanism tends to result in a randomization or loss in texture intensity, however, we observe the development of a primary texture (Fig.3.4a). It has been observed that deformation of polyphase materials by Coble creep in combination of GBS might result in the development of a texture due to reorientation of grains towards a preferred alignment for interface reactions (Heidebach et al., 2000; Sundberg and Cooper, 2008). Such an explanation can be ruled out in this case since the calcite marble is almost pure

with only minor amounts of quartz, dolomite and mica, being stable over a wide range of P-T conditions along the P-T path of Syros (Rogowitz et al. under review) making any mineral reactions almost impossible. Texture development by stress directed growth as suggested by Schmid et al. (1977) and Bons and den Brok (2000) is rather unlikely due to the lack of evidence for abundant grain growth. Another conceivable mechanism resulting in texture development during GSS creep might be strain accommodation by a combination of GBS and dislocation creep as observed by Rutter et al., 1994 in fine grained calcite aggregates deformed at temperatures around 700 °C and by Schmid et al. (1977) in Solnhofen limestone deformed at temperatures above 800 °C. The activity of GBS would be consistent with the observed random misorientation angle distribution (Fig.3.4b) indicating that no relation between neighbouring grains exists, being a typical pattern observed for grains deformed by GBS (Wheeler et al., 2001; Bestmann and Prior, 2003). The arrangement of grains into triple and four-grain junctions is often observed in rocks deformed by GBS (Ashby and Verrall, 1973; Etheridge and Wilkie, 1979). The occurrence of small rounded grains in the center of four- to six-grain junctions is probably caused by rearrangement of sliding grains from neighboring layers during GBS (Gifkins, 1978). Observed curved grain boundaries of larger grains might be due to activation of dislocation creep processes as the grains might be too large to slide past each other, resulting in strain accommodation by grain boundary migration recrystallization.

The observed high dislocation density within small grains (Fig.3.6, 3.7) is consistent with the idea that GBS was accommodated by dislocation creep. Presence of Frank-Read sources is indicating that a large amount of strain had to be accommodated by crystal plasticity, requiring a high density of geometrical necessary dislocations. The activation of Frank-Read sources requires high stresses which might explain the preferred location at grain boundaries since especially during GBS a stress concentration at boundaries between sliding and blocking grains occurs. The absence of low angle grain boundaries rules out the possibility of strain energy reduction by classical thermal activated dislocation creep (Molli et al., 2011). Instead the observed networks and hexagonal cells indicate the activation of cross-slip. Similar dislocation networks have been observed by others and related to low temperature deformation of calcite by cross slip (Kennedy and

White, 2002; Molli et al., 2011). Cross slip is a mechanism that allows dislocations to overcome obstacles by gliding from one plane to a symmetrically related plane containing the same burgers vector (De Bresser and Spiers, 1990), resulting in a rearrangement of screw dislocations without thermal diffusion induced climb. Typical observed slip planes appropriate for cross slip are r- and f-planes in calcite having the same burgers vector (De Bresser et al., 2002). The observed texture showing an alignment of one of the r-poles almost perpendicular to the foliation plane and an oblique, slightly rotated towards the shear direction maximum of c-axis has been observed to occur during r-slip activity (Oesterling et al., 2007) indicating that r- slip might be a possible active slip system in the investigated layer. Nevertheless the extreme low texture index j indicates that most of the strain has to be accommodated by GBS.

3.5.3 Cavitation process

The process of cavitation is still not fully understood, different mechanisms have been associated with the nucleation of cavities in polycrystalline material some of the most common ones are related to vacancy condensation at a high stress region, presence of second particles, dislocation pile up at grain boundaries or grain boundary sliding (Kassner and Hayes, 2003; Füsseis et al., 2009; Rybacki et al., 2010). The preferential location of grain boundary openings orientated at a low angle to the shortening direction has already been observed by others in fine grained polycrystalline material (Ree, 1994; Mancktelow et al., 1998) and has been associated to the activity of GBS. Comparing the shape and location of cavities to the schematic drawing in Figure 3.10 we can clearly relate the occurrence of cavities to the model by Ree (1994) who observed cavitation during grain neighbor switching. Opening of cavities occurs parallel to the shortening direction which are during further deformation partly closed due to further sliding of the grains, resulting in a small cavity at grain-triple junctions (Fig.3.10b). Therefore the observed cavities at four-grain and triple junctions (Fig.3.3a-d) are most likely related to GBS.

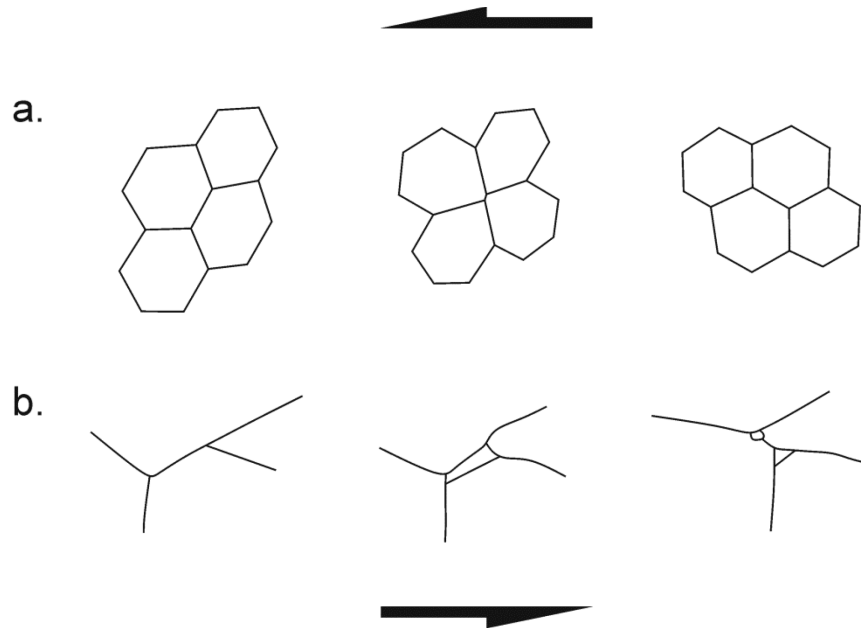


Figure 3.10

a. Sketch showing the movement of grains during grain boundary sliding resulting in grain neighbor-switching, creating four-grain and triple junctions (modified after Ashby and Verrall, 1973). b. Sketch showing the preferred location of cavities developed during grain boundary sliding (modified after Ree, 1994).

3.5.4 Comparison of different stress calculations

Differential stress values calculated by the different methods (paleowattmeter, paleopiezometer, dislocation density) result in different values that nevertheless all lie in the same order of magnitude. Differential stresses obtained by relations between grain size and stress range between 170 and 200 MPa and seem to be the most accurate ones, taking into account that at these conditions both the paleowattmeter and paleopiezometer are consistent with the field boundary theory. For stresses calculated in relation to the dislocation density we are only going to discuss values corresponding to an average specimen thickness. Using the relation by Kohlstedt and Weathers (1980) we get three different average values, depending on the burgers vector length. The stress calculated for a burgers vector with a length of 4.98 \AA , as observed for basal slip is in average 88 MPa. This relatively small value would correspond to deformation at lower strain rates and plot in the deformation mechanism map completely within the GSS creep field what seems unlikely taking the observed simultaneous activation of GBS and

dislocation movement into account. Also the preferred crystallographic orientation of c-axis alignment does not correspond to dominant slip by basal $\langle a \rangle$. Average values calculated for a burgers vector length of 6.37 Å typical for f-slip, results in similar low values of 112 MPa. Such values would again suggest deformation dominated by GSS creep mechanism and are therefore rather unlikely. Assuming a burgers vector length of 8.09 Å we reach average differential stress values of around 142 MPa, plotting close to the field boundary indicating that a high amount of dislocation activity might be active. The used burgers vector has been observed to operate during slip on r- and f-planes (Goetze and Kohlstedt, 1977). Assuming that the idea of rather cross slip being active than dislocation creep is valid, this burgers vector seems to be the best fitting one. Differential stresses calculated by the more recent equation suggested by De Bresser (1996) are almost identic with the ones calculated by paleowattmeter with an average of 197 MPa. It is important to note that all of the calculated differential stresses lie below the calculated brittle stress applying the Byerlee law (Byerlee, 1978) for suggested pressure conditions of around 2 and 4 kbar consistent with microstructural observation indicating that the deformation was ductile.

3.6 Conclusion

Detailed microstructural analysis of a highly strained ($80 < \gamma < 1000$) calcite ultramylonite shows that at strain rates of around $10^{-9} - 10^{-10} \text{ s}^{-1}$ recrystallization by bulging results in strain free, small grains. The change in grain size results in activation of grain boundary sliding as indicated by a random misorientation angle distribution and preferred alignment of grains in triple- and four-grain junctions. The presence of Frank-Read sources and high dislocation density in addition to a weak primary CPO indicates that grain boundary sliding was accommodated by dislocation activity. This is also in agreement with the stable grain size plotting exactly at the boundary between GSS and GSI creep. Nevertheless the absences of features typical for dislocation creep like low angle grain boundaries and the presence of small dislocation networks indicates that rather dislocation glide, cross slip and network assisted dislocation movement are active

combining activity on r- and f-planes. Our study shows that the switch from dislocation creep to grain boundary sliding accommodated by dislocation activity results in strain softening and can be an important strain localization process in calcite rocks, even at high strain rate ($\sim 10^{-9} \text{ s}^{-1}$) and low temperature (300 °C), where you could expect brittle deformation.

Appendix 3

Table A3.1 Dislocation Densities and corresponding Stress

ρ [m^{-2}]	ρ_{init} [m^{-2}]	σ DB [MPa]	σ DB ρ_{init} [MPa]	σ DB ρ_{init} [MPa]	σ f [MPa]	σ f ρ_{init} [MPa]	σ f ρ_{init} [MPa]	σ c [MPa]	σ c ρ_{init} [MPa]	σ c ρ_{init} [MPa]	σ f [MPa]	σ f ρ_{init} [MPa]	σ r [MPa]	σ r ρ_{init} [MPa]
$4.5 \cdot 10^{13}$	$6.4 \cdot 10^{13}$	221.20	274.27	164.51	123.47	146.85	97.24	96.52	114.81	76.02	156.80	186.50	123.50	
$4.4 \cdot 10^{13}$	$5.3 \cdot 10^{13}$	219.34	271.97	163.13	123.63	145.85	96.58	95.87	114.03	75.51	155.74	185.24	122.66	
$5.8 \cdot 10^{13}$	$8.2 \cdot 10^{13}$	259.78	322.11	193.21	140.56	167.18	109.39	109.89	130.70	86.55	178.51	212.32	140.60	
$3.4 \cdot 10^{13}$	$4.9 \cdot 10^{13}$	187.12	232.02	139.17	107.88	128.32	84.97	84.34	100.32	66.43	137.01	162.96	107.91	
$5.1 \cdot 10^{13}$	$7.2 \cdot 10^{13}$	238.28	296.69	177.96	131.54	156.46	103.61	102.84	122.32	81.00	167.06	198.70	131.58	
$2.7 \cdot 10^{13}$	$3.8 \cdot 10^{13}$	160.25	198.70	119.18	95.20	113.24	74.98	74.43	88.53	58.62	120.91	143.81	95.23	
$3.9 \cdot 10^{13}$	$5.5 \cdot 10^{13}$	203.13	251.87	151.08	115.27	137.10	90.79	90.12	107.18	70.98	146.39	174.12	115.30	
$4.8 \cdot 10^{13}$	$6.8 \cdot 10^{13}$	230.35	285.62	171.32	127.57	151.73	100.47	99.73	118.62	78.55	162.02	192.70	127.60	
$3.3 \cdot 10^{13}$	$4.6 \cdot 10^{13}$	181.94	225.60	135.32	105.47	125.44	83.07	82.46	98.07	64.94	133.95	159.32	105.50	
$3.3 \cdot 10^{13}$	$4.7 \cdot 10^{13}$	182.99	226.89	136.10	105.96	126.02	83.45	82.84	98.52	65.24	134.57	160.05	105.99	
$4.4 \cdot 10^{13}$	$6.2 \cdot 10^{13}$	218.77	271.26	162.71	122.37	145.55	96.38	95.67	113.79	75.35	155.41	184.85	122.40	
$2.6 \cdot 10^{13}$	$3.7 \cdot 10^{13}$	157.98	195.89	117.50	94.12	111.94	74.13	73.58	87.51	57.95	119.53	142.17	94.14	
$3.3 \cdot 10^{13}$	$4.6 \cdot 10^{13}$	180.90	224.30	134.54	104.98	124.86	82.68	82.07	97.62	64.64	133.33	158.58	105.01	
$4.0 \cdot 10^{13}$	$5.7 \cdot 10^{13}$	207.18	256.89	154.09	117.12	139.30	92.24	91.56	108.90	72.11	148.74	176.91	117.15	
$4.1 \cdot 10^{13}$	$5.8 \cdot 10^{13}$	209.53	259.80	155.84	118.19	140.57	93.08	92.40	109.90	72.77	150.10	178.53	118.22	
$4.7 \cdot 10^{13}$	$6.7 \cdot 10^{13}$	227.77	282.42	169.40	126.42	150.36	99.57	98.83	117.55	77.84	160.55	190.96	126.45	
$4.5 \cdot 10^{13}$	$1.2 \cdot 10^{14}$	221.31	398.61	164.54	123.52	198.53	97.26	96.56	155.21	76.04	156.87	252.13	123.52	
$5.1 \cdot 10^{13}$	$1.3 \cdot 10^{14}$	239.49	431.36	181.64	131.64	211.58	103.65	102.91	165.41	81.03	167.18	288.71	131.64	
$4.7 \cdot 10^{13}$	$1.4 \cdot 10^{14}$	247.48	445.75	184.00	135.17	217.25	106.43	105.67	169.84	83.21	171.66	275.91	135.17	
$5.1 \cdot 10^{13}$	$1.3 \cdot 10^{14}$	240.30	432.81	178.66	131.99	212.15	103.93	103.19	165.86	81.25	167.64	269.44	132.00	
$5.8 \cdot 10^{13}$	$1.5 \cdot 10^{14}$	257.63	464.04	191.55	139.62	224.41	109.94	109.16	175.44	85.95	177.32	285.01	138.62	
$2.5 \cdot 10^{13}$	$6.5 \cdot 10^{13}$	154.32	277.96	114.74	92.36	148.44	72.72	72.20	116.05	56.85	117.29	188.52	92.36	
$2.0 \cdot 10^{13}$	$5.2 \cdot 10^{13}$	133.77	240.94	99.46	82.30	132.28	64.80	64.34	103.42	50.66	104.52	168.00	82.30	
$3.4 \cdot 10^{13}$	$8.8 \cdot 10^{13}$	186.13	335.25	138.39	107.42	172.66	84.59	83.98	134.98	66.13	136.43	219.28	107.43	
$4.7 \cdot 10^{13}$	$1.2 \cdot 10^{14}$	227.55	409.85	169.18	126.32	203.03	99.46	98.75	158.73	77.76	160.43	257.85	126.32	
$3.3 \cdot 10^{13}$	$8.6 \cdot 10^{13}$	183.65	330.79	136.55	106.27	170.80	83.68	83.08	133.53	65.42	134.96	216.92	106.27	
$2.7 \cdot 10^{13}$	$7.0 \cdot 10^{13}$	161.03	290.04	119.72	95.58	153.62	75.26	74.72	120.10	58.84	121.39	195.10	95.58	
$2.0 \cdot 10^{13}$	$5.1 \cdot 10^{13}$	133.00	239.56	98.89	81.92	131.67	64.50	64.04	102.94	50.43	104.04	167.22	81.92	
$2.5 \cdot 10^{13}$	$6.5 \cdot 10^{13}$	154.62	278.50	114.96	92.50	148.67	72.83	72.32	116.23	56.94	117.48	188.82	92.50	
$2.7 \cdot 10^{13}$	$6.9 \cdot 10^{13}$	159.75	287.74	118.78	94.97	152.64	74.78	74.24	119.33	58.46	120.61	193.85	94.97	
$3.1 \cdot 10^{13}$	$7.9 \cdot 10^{13}$	174.62	314.52	129.83	102.03	164.00	80.34	79.77	128.21	62.81	129.59	208.28	102.04	
$2.5 \cdot 10^{13}$	$6.5 \cdot 10^{13}$	153.72	276.88	114.29	92.06	147.97	72.49	71.98	115.68	56.67	116.92	187.93	92.07	

4. $^{40}\text{Ar}/^{39}\text{Ar}$ mica ages from marble mylonites: a cautionary tale

Abstract

Microstructural, geochemical and isotopic analyses have been performed on a mylonitic shear zone and its calcite marble host rock from Syros (Cyclades, Greece). Microstructures and kinematics of the shear zone are consistent with a well-documented Miocene low-grade metamorphic event whereas the coarse-grained host rock likely records a regional Eocene high-grade event. Laser-heating $^{40}\text{Ar}/^{39}\text{Ar}$ analysis on white mica yielded a ca. 40 Ma age for the host rock and a ca. 37 Ma age for the shear zone. Both ages are statistically indistinguishable, suggesting instead the regional Eocene event, and not the Miocene deformation event, is responsible for the formation of the shear zone. Thermodynamic modelling indicates that the observed mineral assemblage is stable without compositional change along the pressure-temperature path followed by the rocks of Syros. Although the marble within the shear zone was deformed at extremely fast strain rates, we observe no intracrystalline deformation of white mica grains and no resetting in the isotopic system. Our study emphasizes that detailed microstructural analysis is necessary when obtaining $^{40}\text{Ar}/^{39}\text{Ar}$ ages from calcite marble since the degree of mica recrystallization is the controlling factor for resetting the K-Ar system and not the amount of strain a rock endured.

Chapter 4. is based on:

Rogowitz, A., Huet, B., Schneider, D. and Grasemann, B. $^{40}\text{Ar}/^{39}\text{Ar}$ mica ages from marble mylonites: a cautionary tale. Submitted to Lithosphere on the 8th of September 2014.

4.1 Introduction

$^{40}\text{Ar}/^{39}\text{Ar}$ geochronology on white mica is a popular method to date deformation under moderate temperature conditions (e.g. Dunlap, 1997; Sigoyer et al., 2000; Bröcker et al., 2004; Cossette et al., in press). In metasedimentary packages under upper greenschist to lower amphibolite metamorphic conditions, deformation tends to localize in calcite marbles resulting in the formation of mylonites and ultramylonites (Bestmann et al., 2000). In such rocks however, little is known about the behaviour of the K/Ar system in mica and the influence of high strain, particularly with reference to potential inefficient removal of ^{40}Ar from the grain boundary (Warren et al., 2012).

Several models invoke deformation-related Ar-loss and therefore may justify the interpretation of mica dates as deformation ages. Some examples include: (1) Due to deformation-related ductile or brittle grain size reduction, the diffusion length scale is reduced and consequently volume diffusion is more efficient (Goodwin and Renne, 1991). (2) Strong intracrystalline deformation is always accompanied by an increase in dislocation density in the crystals resulting in increased pipe-diffusion. Pipe diffusion has a lower activation energy and larger diffusion coefficient than volume diffusion and is therefore more efficient (Kramer et al., 2001; Dunlap and Kronenberg, 2001). (3) Ar loss during mica neocrystallization, resets the K/Ar system and potentially resulting in mixed ages (e.g. Wijbrans and McDougall, 1986; Foster and Lister, 2004; Cossette et al., in press).

Because of possible physiochemical mechanisms leading to Ar loss during deformation, the interpretation of geochronological data requires detailed microstructural and geochemical analyses. In this study we use an outcrop on Syros (Cyclades, Greece) as a case study to assess the extent and nature of K/Ar resetting due to extremely localized deformation in marbles. Our study presents $^{40}\text{Ar}/^{39}\text{Ar}$ ages from two marble samples that followed the same P-T-t path but witnessed contrasting strain intensities at different strain rates resulting in extreme variations in marble microfabrics.

4.2 Geological setting and Outcrop description

Syros Island (Greece) is part of the Cycladic blueschist belt that is situated in the back-arc of the Hellenic subduction zone (Papanikolaou, 1987; Wortel et al., 1993). The Cycladic area is build up of three main units, separated by tectonic contacts, which are, from bottom to top, the para-autochthonous Basement Unit, the Cycladic Blueschist Unit (CBU) and the Upper Unit (e.g. Bonneau, 1984; Jolivet and Brun, 2010).

Syros is mainly dominated by the CBU; only in the south-east of the island is the Upper Unit exposed (Tomaschek et al., 2000; Keiter et al. 2011; Soukis and Stockli, 2013). Two major Cenozoic metamorphic events have affected the Cyclades (Jolivet and Brun, 2010; Ring et al., 2010). Both events, Eocene M1 eclogite-blueschist facies event and Oligo-Miocene M2 greenschist facies event, are well documented on Syros yet the shear sense recorded by the rocks has been ascribed to different kinematic models (Gautier and Brun, 1994; Trotet et al., 2001a; Bond et al., 2007; Keiter et al., 2011; Philippon et al., 2011).

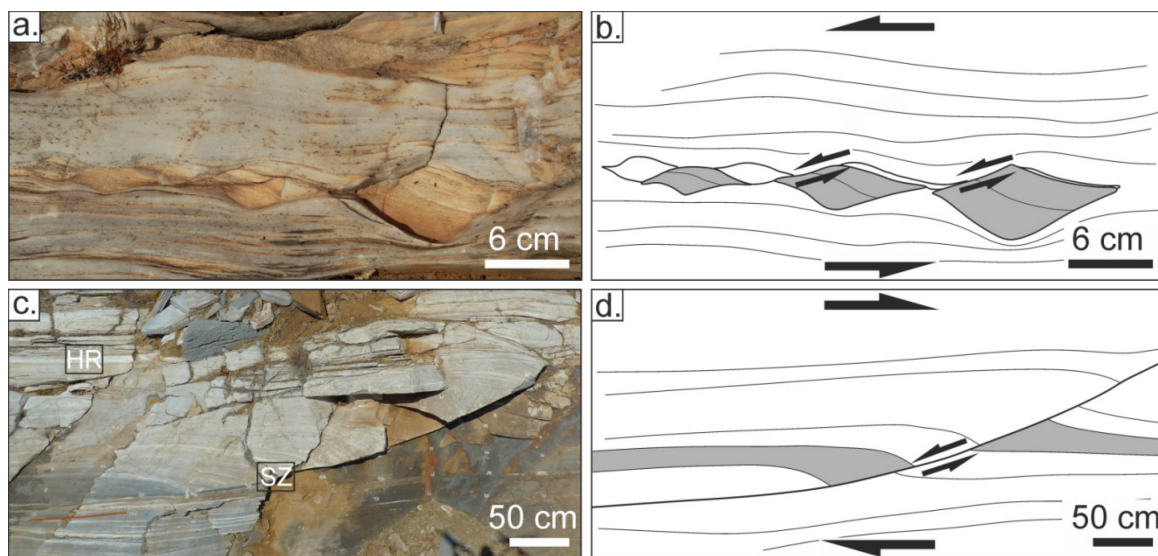


Figure 4.1

Photographs of the investigated outcrop on Syros (UTM35 414840N 313839E), showing two different shear sense indicators (A, C). The sketches show the interpretation (B, D). View is to the north. A, B. Asymmetric boudinaged dolomite layer in marble showing evidence of top-to-west shear. C, D. A-type flanking structure indicating overall top-to-east sense of shear resulting in local antithetic shearing. HR and SZ indicate the location of the sampled host rock and shear zone, respectively.

Our study focuses on an outcrop in the western part of Syros. It exposes a decameter-scale thick calcite marble layer intercalated with quartz and dolomite lenses, preserving an E-W trending lineation and two different shear kinematics. Quartz and dolomite layers are interpreted as asymmetric shearband boudinage indicating top-to-west shearing (Goscombe et al., 2004; Fig.4.1a, b). The higher temperatures required for ductile deformation of dolomite and quartz suggests that these structures are likely related to the Eocene M1 event. Conversely, flanking structures and localized shear zones in calcite marble show top-to-east shearing (Fig.4.1c, d). These overprinting structures, which formed under lower metamorphic conditions, are interpreted to be related to the Oligo-Miocene M2 greenschist facies event. We collected samples from a 5 m-long a-type flanking structure (Grasemann and Stüwe, 2001; Passchier, 2001). It developed due to the rotation of a crack at the same rates as a passive marker line (cross-cutting element) during top-to-east shearing, resulting in antithetic slip along the cross-cutting element and the formation of a secondary shear zone with a maximum displacement of 120 cm. As a consequence of overall top-to-east shearing, a local antithetic top-to-west sense of shear within the secondary shear zone can be observed (Rogowitz et al., 2014). Numerical models have shown that flanking structures develop at relatively low strain ($\gamma < 3$; Kocher and Mancktelow, 2005). We therefore assume that the host rock experienced a shear strain of $\gamma < 3$ during the formation of the flanking structure. However, the rocks within the shear zone experienced a much higher shear deformation, having a maximum displacement of 120 cm at the centre of the shear zone where the width is only 1.5 cm. This corresponds to a shear strain of $\gamma \sim 80$. Note that most of the displacement within the shear zone is accommodated by a fine grained (3 μm) ultramylonite layer with a thickness between 120 and 480 μm located at the boundary of the shear zone. If we consider that these layers have accommodated most of the offset, the shear strain would have values in the order of $\gamma \sim 1000$.

4.3 Results

Two samples, from the host rock (HR) and the shear zone (SZ), were collected for detailed microstructural, geochemical and $^{40}\text{Ar}/^{39}\text{Ar}$ analyses. The marble is composed of nearly pure calcite with minor amounts of dolomite (<10%), quartz (<1%) and white mica (<1%). Microstructure of the host rock is characterized by coarse calcite grains with an average grain size of 280 μm . Minor undulatory extinction and slightly curved grain boundaries indicate that minor deformation took place within the dislocation creep field. The relatively coarse grain size is interpreted as result of grain growth at high temperatures during M1. Within the shear zone, strong intracrystalline deformation, subgrain formation and subsequent recrystallization lead to the formation of alternating mylonitic and ultramylonitic calcite layers.

In both samples, mica (long axis <400 μm) is preferentially orientated parallel to the foliation (Fig.4.2) defining the lineation together with the shape-preferred orientation of calcite. In both samples, mica grains behave brittlely rather than ductilely, and experience minor grain size reduction by splitting and breaking preferentially along the cleavage resulting in prismatic or columnar shapes (Fig.4.2c, d). In ultrafine grained (3 μm) layers within the shear zone fracturing perpendicular to the mica cleavage plane can be observed (Fig.4.2b). We therefore consider that white mica was stronger than calcite during shearing, which fostered strain partitioning between the phases.

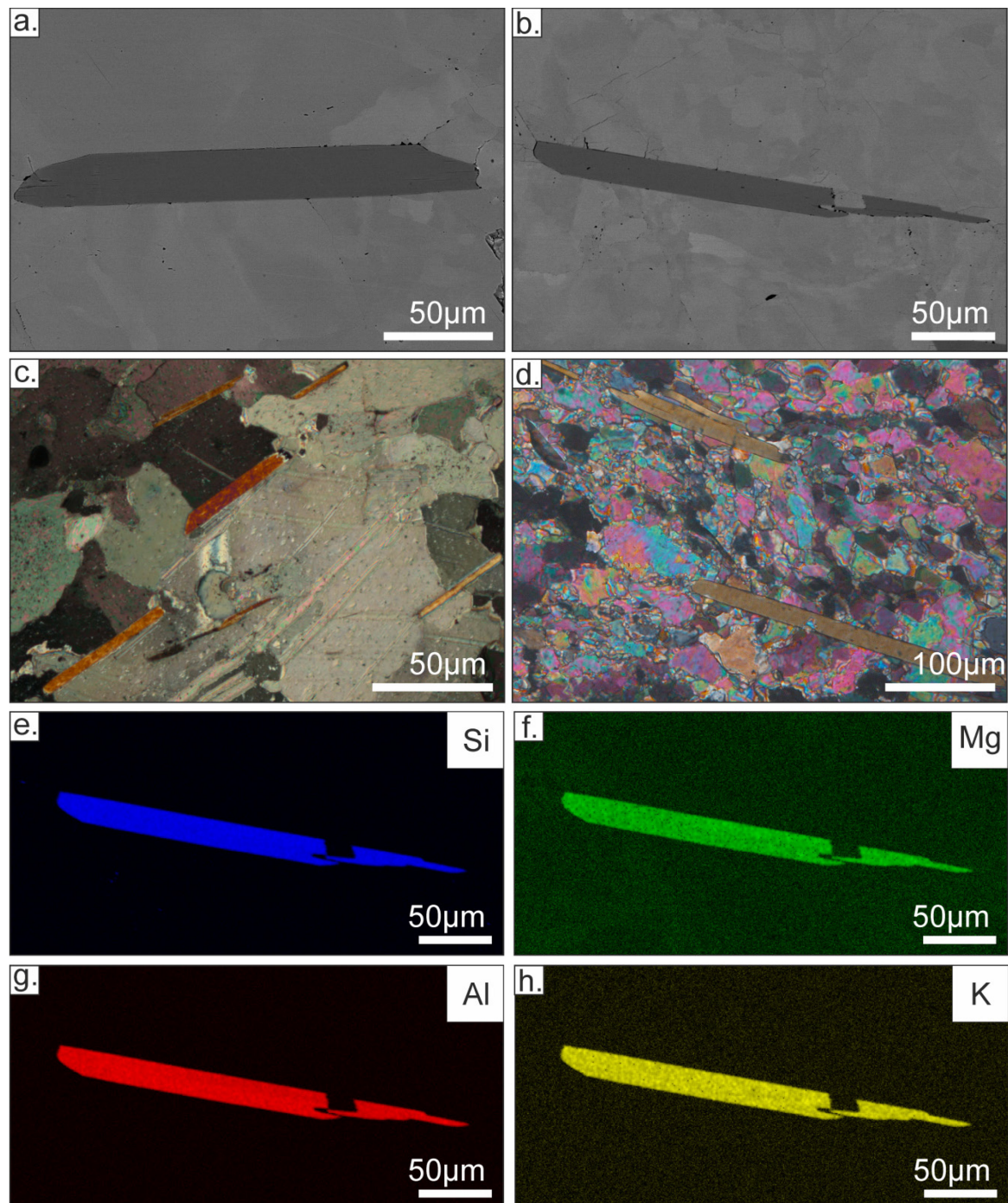


Figure 4.2

a. BSE-image of prismatic white mica in host rock marble. Note that a lack of grey shade variation is an indication of no chemical zoning. b. BSE-image of brittily deformed white mica within the shear zone marble. c. Optical photomicrograph (crossed-polarizers) of the host rock marble showing preferred alignment of mica grains consistent with top-to-east shear. d. Optical photomicrograph (crossed-polarizers) of the shear zone showing locally brittily deformed mica surrounded by recrystallized calcite. e-h. EDX-maps of brittily deformed white mica of the shear zone showing homogeneous distribution of Si, Mg, Al, and K.

Electron microprobe analyses (EMP) have been performed on a Cameca SX-100 (University of Vienna, Austria) at an accelerating voltage of 15 kV and a current of 20 nA with a defocused beam up to 7 μm in diameter. The analyses reveal that in both samples the white mica has a relatively high Si content (3.4-3.6; Fig.4.3a). The scattering in Si content can be attributed to EMP uncertainties, as shown by a Monte Carlo analysis (Table A4.3 in the appendix). The Fe content is almost below the detection limit resulting in an X_{Mg} greater than 0.97 (Fig.4.3a). Nevertheless a trend towards a systematically higher Fe content (X_{Mg} =0.98-0.99) in the shear zone mica can be observed compared to the micas in the host rock (X_{Mg} =0.99-1.00). The end-member composition of the mica in both samples is around 50% muscovite, 45% celadonite and smaller amounts of paragonite and pyrophyllite (Fig.4.3b). Chlorine and fluorine concentrations are below the detection limit. Except for the slight Fe content variance, there is no distinct difference in chemical composition of mica located in the host rock and the shear zone. We do not observe any chemical zonation in the mica, which is consistent with SEM-BSE images and EDX-maps displaying homogeneous mica composition (Fig.4.2a, b, and e-h).

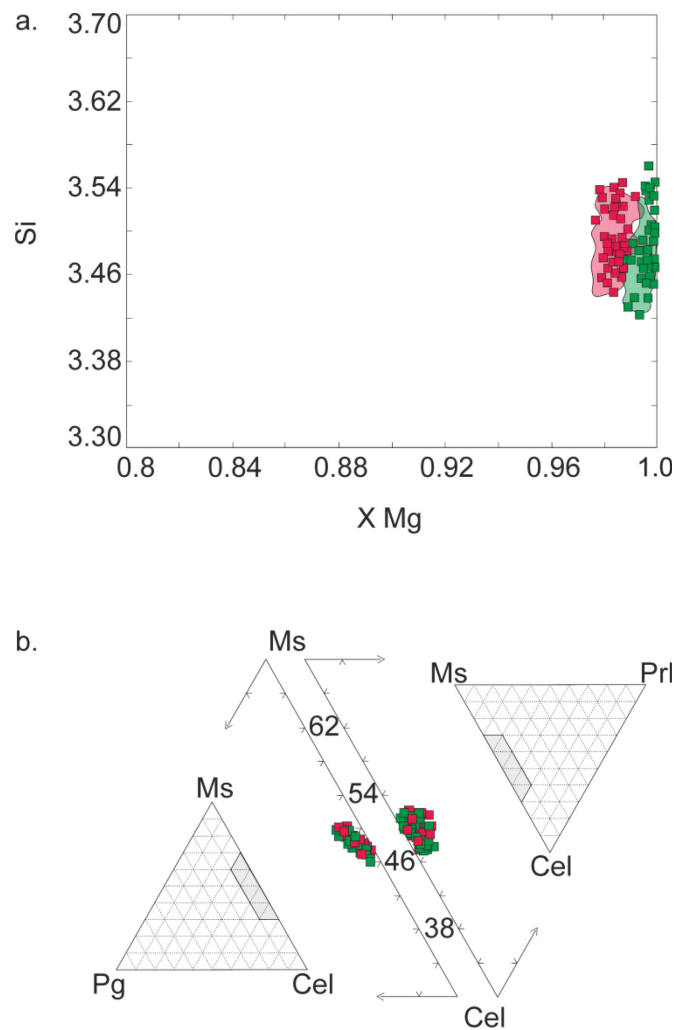


Figure 4.3

a. X_{Mg} vs. Si plot of mica from within the host rock (light grey) and the shear zone (dark grey) illustrating high Si and extremely low Fe content in mica. Shaded areas represent the range of compositions generated with Monte Carlo simulations. b. Ternary diagrams of white mica composition. Note that there is no compositional difference between host rock and shear zone mica (See Table A4.3 in the supplementary for analytical results). End-member abbreviations: Ms: muscovite, Cel: celadonite, Prl: pyrophyllite and Pg: paragonite.

Incrementally step-heated $^{40}\text{Ar}/^{39}\text{Ar}$ geochronology on mica separates has been performed with a Photon Machines CO_2 laser coupled to a Nu Instruments Noblesse multicollector mass spectrometer operated at the Geological Survey of Canada (Ottawa, Canada). Grain size ranges between 106 and 250 μm , and 3-4 grain aliquots were used for the analysis following the protocol of Kellett and Joyce (2014; see data repository for

complete methodology). The mica dates from both the host rock and shear zone are statistically undistinguishable (Fig.4.4a), and total gas ages are concordant to preferred ages. The age spectrum for mica located within the host rock is somewhat erratic varying between 32 and 41 Ma yielding a preferred $^{40}\text{Ar}/^{39}\text{Ar}$ age of 40.2 ± 1.6 Ma. The spectrum for mica located within the shear zone is less disturbed, with little variation in age between 36 and 40 Ma, yielding a preferred $^{40}\text{Ar}/^{39}\text{Ar}$ age of 37.4 ± 1.3 Ma. A $^{38}\text{Ar}/^{39}\text{Ar}$ versus $^{37}\text{Ar}/^{39}\text{Ar}$ diagram shows a clear data cluster for the shear zone mica, indicating an isochemical Ar population whereas data for the host rock are variable, consistent with the more disturbed age spectra for host rock mica (Fig.4.4b).

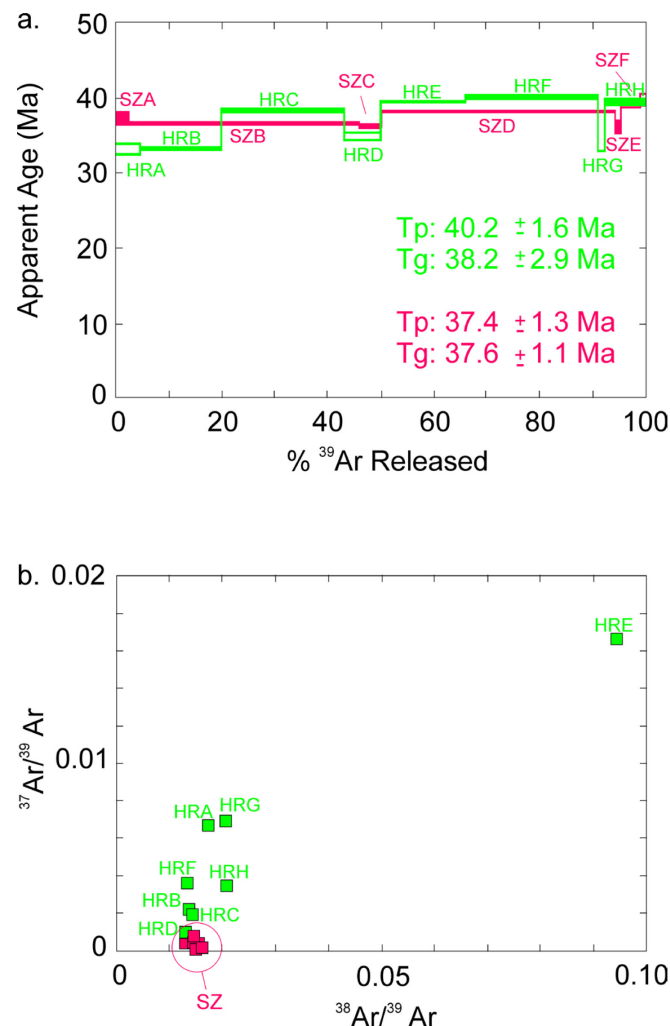


Figure 4.4

$^{40}\text{Ar}/^{39}\text{Ar}$ age step-heated release spectra for white mica located within the host rock (light grey) and shear zone (dark grey) on Syros. Note that both spectra yield concordant ages. Tg: total-gas age. Tp: preferred age (See Table A4.4 in the supplementary for analytical results). B. $^{38}\text{Ar}/^{39}\text{Ar}$ vs. $^{37}\text{Ar}/^{39}\text{Ar}$ graph illustrating a potential isochemical population for the shear zone mica analyses and a more heterogeneous chemical population for host rock mica. The individual steps are labelled, and correspond to the steps on the spectra (Table A4.4).

4.4 Discussion

The marble microstructures we describe from the outcrop on Syros are consistent with calcite deformation at $\sim 300^\circ\text{C}$ (Bestmann et al. 2000). A differential stress-grain size deformation mechanism map for calcite has been calculated using flow laws of Renner et al. (2002) for the dislocation creep and of Herwegh et al. (2003) for the diffusion creep field. The observed grain size evolution within the shear zone has been plotted using a stable grain size of $3\text{ }\mu\text{m}$ for the final state. Differential stress and corresponding strain rates have been calculated with the paleowattmeter of Austin and Evans (2009). The map shows that the host rock has been deformed at strain rates of around 10^{-12} s^{-1} whereas within the shear zone, strain rates reached $\sim 10^{-9}\text{ s}^{-1}$ (Fig.4.5). Based on our strain and strain rate data, the interval of deformation is estimated to have lasted ca. 25 kyr.

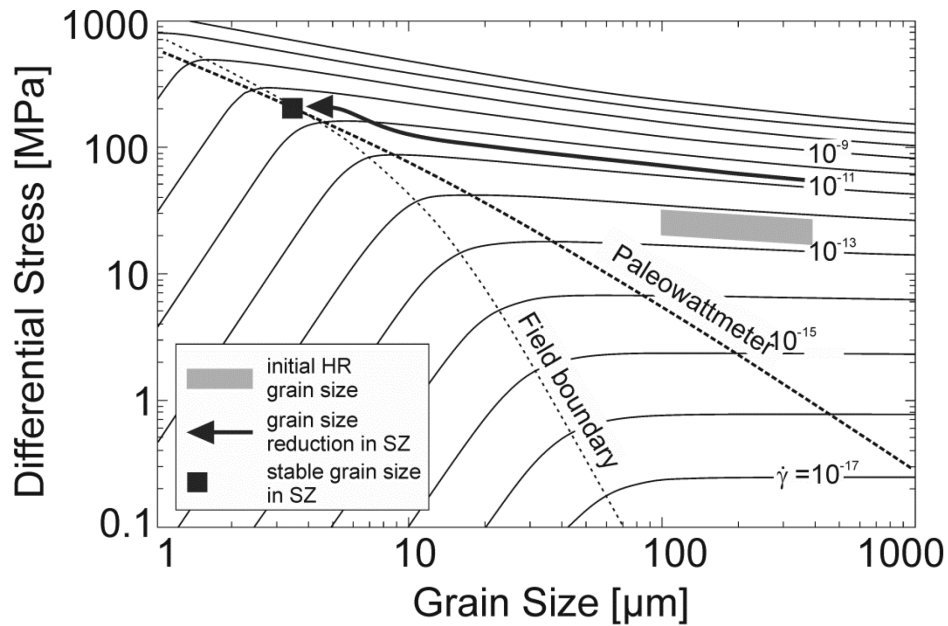


Figure 4.5

Deformation mechanism map for calcite in the grain size - differential stress space at 300°C . Flow laws for grain size insensitive creep (Renner et al., 2002) and grain size sensitive creep (Herwegh et al., 2003) have been used. Additionally the field boundary which is considered to correspond to the stabilization of the grain size at values balancing diffusion and dislocation creep (De Bresser et al., 2001) and the paleowattmeter linking stable grain size and differential stress (Austin and Evans, 2009) are plotted. The map shows grain size evolution via deformation induced grain size reduction until a stable grain size of $\sim 3\text{ }\mu\text{m}$ is attained.

Qualitative temperature estimates together with the top-to-east kinematics of the structure indicates that the flanking structure developed during Oligo-Miocene greenschist facies deformation. However, the $^{40}\text{Ar}/^{39}\text{Ar}$ mica ages for the host rock and shear zone of ca. 37-40 Ma correlate to the regional high pressure event (Bröcker et al., 2013), indicating that the mica preserve the age of the older M1 event and not the formation of the Miocene flanking structure. Apparently there was no resetting of the K/Ar system during deformation associated with shear zone formation. Although we have documented strain rates up to $\sim 10^{-9} \text{ s}^{-1}$, we do not observe any mica recrystallization that would have led to geochemically distinct zones nor loss of radiogenic Ar. The observed strain partitioning between weak calcite and strong muscovite is consistent with experiments on calcite-muscovite aggregates showing that once mica is rotated in the shear direction it behaves rather rigidly (Delle Piane et al., 2009). The only deformation mechanism recorded in the mica is therefore minor brittle deformation preferentially along the cleavage, which has been proved to be negligible for Ar loss at low temperatures (Dunlap and Kronenberg, 2001). Due to the short deformation interval (ca. 25 kyr) at low temperatures ($\sim 300^\circ\text{C}$), which is below muscovite $^{40}\text{Ar}/^{39}\text{Ar}$ closure temperature (Hames and Bowring, 1994; Harrison et al., 2009), evidence for enhanced effective volume diffusion, due to reduced diffusion path lengths by brittle deformation perpendicular to the cleavage, can be excluded for our samples.

In addition to potassium, Ca and Cl concentrations are important factors when interpreting $^{40}\text{Ar}/^{39}\text{Ar}$ spectra since ^{37}Ar and ^{38}Ar can be derived from these elements, respectively (McDougall and Harrison, 1999), and may shed light on the homogeneity of a sample. The shear zone mica is clearly isochemical, tightly clustering into a single population (Fig.4.4b), indicating a single Ar reservoir. The host rock mica is comparatively scattered, particularly with respect to ^{37}Ar . The somewhat heterogeneous $^{37}\text{Ar}/^{39}\text{Ar}$ versus $^{38}\text{Ar}/^{39}\text{Ar}$ distribution for host rock mica may be explained by the presence of different Ar reservoirs (e.g. Foster and Lister, 2004) or is a result of minor Ca (as ^{37}Ar) contamination of calcite intergrown within or on the mica. Interestingly, although the $^{40}\text{Ar}/^{39}\text{Ar}$ analysis reveals two distinct chemical behaviours in Ar-isotope space, our EMP and EDX mineral chemistry data illustrate that neither mica sample

exhibit chemical zoning and both samples are chemically homogeneous with respect to the major element chemistry.

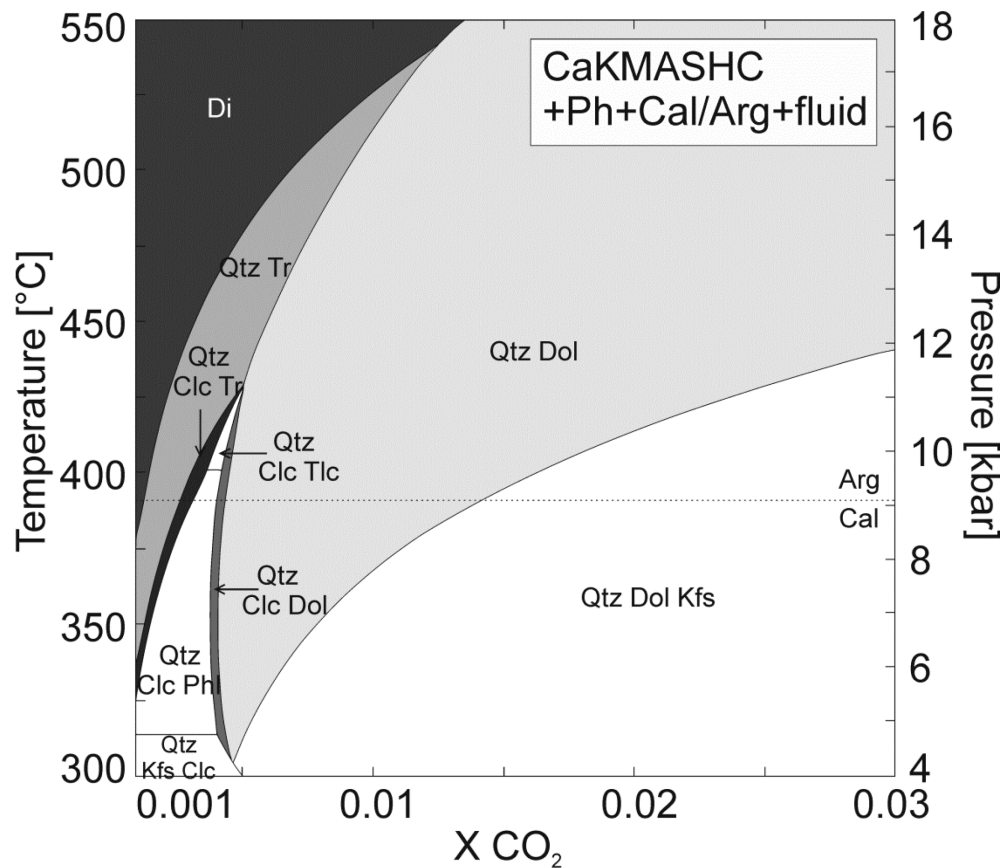


Figure 4.6

Phase equilibrium diagram in the CaKMASHC system demonstrating the stability field of the observed mineral assemblage (Ph + Cal + Qtz + Dol). Calculation was done with the PERPLEX 6.6.6 package using the Holland and Powell (1998) database. Bulk rock composition was calculated using mineral fractions and EMP analyses. Pressure-temperature and fluid composition are likely to have varied during the metamorphic evolution of the studied rocks. The phase diagram was therefore calculated along variable H₂O-CO₂ fluid composition (x-axis) and a linear gradient (from 550 °C, 18 kbar to 300 °C, 4 kbar; y-axis) that approximates the P-T path of Syros (Trotet et al., 2001b; Keiter et al., 2004). Mineral abbreviations: Qtz: quartz, Dol: dolomite, Clc: clinocllore, Phl: phlogopite, Ph: phengite, Tr: tremolite, Kfs: potassium feldspar, Di: diopside, Tlc: talc, Arg: aragonite and Cal: calcite.

The apparent homogeneous chemical composition of mica for the host rock and shear zone can be explained by thermodynamic modelling (Fig.4.6). An equilibrium phase diagram calculated for the rock composition suggests that the documented mineral assemblage (calcite/aragonite + quartz + dolomite + phengite) is stable over a wide

range of fluid compositions and P-T conditions along the PT-path of Syros (Trotet et al., 2001b; Schumacher et al., 2008). The parameters of the model include information on fluid composition, demonstrating that the mineral assemblage is also stable for CO_2 fractions between 0.005 and 0.03. Similar fluid compositions ($\text{XCO}_2 < 0.03$) have been reported for glaucophane-bearing marbles of Syros (Schumacher et al., 2008). With mica being the only stable K- and Al-bearing phase over a wide range of P-T conditions, a change in mica chemical composition by Tschermak and pyrophyllite substitution is not probable. The mica chemistry is therefore stable within the marble's mineral assemblage and is not required to reequilibrate through prograde and retrograde conditions. If chlorite would have been present, the activation of these substitutions might have been possible resulting in potential resetting of K/Ar system.

4.5 Conclusion

Step-heated $^{40}\text{Ar}/^{39}\text{Ar}$ geochronology performed on white mica from host rock and shear zone marbles collected on Syros result in indistinguishable ages of ca. 40 Ma. Although marbles were deformed during the Miocene at extremely fast strain rates ($\sim 10^{-9} \text{ s}^{-1}$), calcite accommodated most of the strain, thus inhibiting mica recrystallization. In addition metamorphic conditions modelled from the preserved mineral assemblage do not require muscovite reequilibration during the Miocene thermal event. Neither mechanical nor chemical processes caused any recrystallization of the white mica crystal lattice in our samples, therefore the K/Ar system remained closed during the duration of the deformation event, even though strain and strain rates are extremely high. These conclusions imply that our $^{40}\text{Ar}/^{39}\text{Ar}$ mica ages record an older high grade (M1) event and not the Oligo-Miocene M2 flanking structure from which they were sampled. This study underscores that calcite marble may not be an ideal host for resolving deformation ages. Moreover, it is the degree of mica recrystallization and not the amount of strain the rock has witnessed in controlling the resetting of K/Ar systems at low temperatures.

Appendix 4

A4.1 $^{40}\text{Ar}/^{39}\text{Ar}$ sample preparation

After mechanical mineral separation from the host rock to achieve 99% purity, white mica with grain size between 106 and 250 μm was picked and washed with dilute HCl. Individual mineral separates were loaded into 2-3 mm-deep aluminum foil packets, which were subsequently stacked vertically into 35-mm long foil tubes and placed into the tubular holes of an aluminum cylinder. Several flux monitor grains of Fish Canyon tuff sanidine (FCT-SAN) (28.02 ± 0.16 1σ Ma; Renne et al., 1998, ^{40}K decay = $5.543\text{e-}10/\text{a}$, Steiger and Jäger, 1977) were loaded into each sample packet. The vessel was irradiated for 160 MWH in medium flux position 8A at the research nuclear reactor of McMaster University (MNR) in Hamilton, Canada. Neutron fluence was approximately 1.08×10^{13} neutrons/ cm^2 operating at a 2.5 MW power level. Correction factors for typical interference species produced by thermal neutrons during irradiation are 0.058 ($^{40}\text{Ar}/^{39}\text{Ar}_{\text{K}}$), 0.000743 ($^{39}\text{Ar}/^{37}\text{Ar}_{\text{Ca}}$) and 0.000258 ($^{36}\text{Ar}/^{37}\text{Ar}_{\text{Ca}}$).

A4.2 $^{40}\text{Ar}/^{39}\text{Ar}$ analyses

Analytical conditions follow the protocol of Kellet and Joyce (2014). Small aliquots (3-4 grains) and monitors were loaded into separate 1.5 mm diameter pits in a copper planchet and placed under vacuum. Individual grains were progressively heated and analyzed using a Photon Machines Ltd. Fusion 10.6 55W CO_2 laser coupled to the all-metal extraction line and a Nu Instruments Noblesse multicollector mass spectrometer operated at the Geological Survey of Canada, Ottawa, Canada. Laser heating was homogenized over a beam radius of 2 mm for a total of 40 sec, after which the released gas was exposed to SAESTM NP-10 ($\sim 400^\circ\text{C}$) and HY-STOR[®] 201 (25°C) getters in the extraction line for three minutes. Following gettering, sample gas was expanded into the mass spectrometer. The Nu Noblesse is a single-focussing, Nier-source, magnetic sector multicollector noble gas spectrometer equipped with two quadrupole lens arrays. Argon ions were measured with a fixed array of three ETP[®] discrete dynode ion-counting multipliers (IC0, IC1, IC2). Data collection occurred in two multicollection cycles: cycle 1 =

$^{40}\text{Ar}_{\text{IC0}}$, $^{38}\text{Ar}_{\text{IC1}}$ and cycle 2 = $^{39}\text{Ar}_{\text{IC0}}$, $^{37}\text{Ar}_{\text{IC1}}$, $^{36}\text{Ar}_{\text{IC2}}$. Blanks were run every 5 analyses, in an identical manner to unknowns. Air shots were analyzed every 10 analyses to monitor efficiency and mass fractionation. Relative collector efficiency and mass bias corrections were made for IC1 and IC2 collectors relative to IC0 using $^{40}\text{Ar}_{\text{IC0}}/^{36}\text{Ar}_{\text{IC1}}$ and $^{40}\text{Ar}_{\text{IC0}}/^{36}\text{Ar}_{\text{IC2}}$ measurements of air. Mass bias in IC0 was not corrected as it would be equally applied to the $^{40}\text{Ar}/^{39}\text{Ar}$ ratio in unknowns and J-factors determined from monitors in the age calculation, thereby cancelling out (e.g. Brumm et al., 2010). Error in J-factor values are conservatively estimated at $\pm 0.6\%$ (2σ). Sensitivity of the Nu Noblesse at the time of analyses was 7.1-7.5 Amps/mol. Data collection, reduction, error propagation, age calculation and plotting were performed using the software MassSpec (version 7.93; Deino, 2001).

Analytical results are presented in Table A4.4; Figure 4.4 presents the data as spectra where the width of each bar (thermal increment) represents the proportion of evolved gas, and the height represents the uncertainty associated with the apparent age. The integrated (or total gas: Tg) age is an average age for the sample calculated by summing the isotopic measurements of all steps with an uncertainty calculated by quadratically combining errors of isotopic measurements of all steps. Plateau ages are conventionally defined as the portion of an age spectrum composed of contiguous increments representing >70% of gas released which result in concordant ages (Mahon, 1996). A preferred age (Tp), on the other hand, is calculated as the weighted mean of a selection of mostly contiguous increments which represent >50% of ^{39}Ar gas released and result in concordant ages. The calculated age uncertainties are relatively small because analytical precision in the age of each heating step is high. In our samples, both Tg and Tp are relatively similar in age, and both host rock marble and shear zone are within error of each other, suggesting the ages are robust.

4. $^{40}\text{Ar}/^{39}\text{Ar}$ mica ages from marble mylonites: a cautionary tale

Table A4.3 white mica analysis

	Host rock			Shear zone		
	Measured		Generated [†]	Measured		Generated [†]
	Analysis	Avg. \pm Std [†]	Avg. \pm Std [†]	Analysis	Avg. \pm Std [†]	Avg. \pm Std [†]
	#27	N=44	N=50	#62	N=48	N=50
SiO ₂	52.936	52.781 \pm 0.580	52.624 \pm 0.527	52.697	52.857 \pm 0.404	52.785 \pm 0.508
TiO ₂	0.071	0.094 \pm 0.019	0.102 \pm 0.053	0.140	0.112 \pm 0.026	0.120 \pm 0.049
Al ₂ O ₃	25.202	25.517 \pm 0.765	25.624 \pm 0.476	25.737	25.495 \pm 0.635	25.421 \pm 0.527
Cr ₂ O ₃	0.091	0.162 \pm 0.132	0.164 \pm 0.056	0.024	0.055 \pm 0.067	0.043 \pm 0.036
FeO	0.013	0.039 \pm 0.030	0.046 \pm 0.039	0.173	0.158 \pm 0.034	0.152 \pm 0.051
MnO	5.657	0.006 \pm 0.007	0.020 \pm 0.030	0.001	0.007 \pm 0.010	0.028 \pm 0.031
MgO	0.174	5.430 \pm 0.314	5.427 \pm 0.070	5.275	5.342 \pm 0.209	5.336 \pm 0.074
CaO	0.000	0.244 \pm 0.071	0.247 \pm 0.050	0.117	0.221 \pm 0.087	0.208 \pm 0.052
Na ₂ O	0.294	0.260 \pm 0.093	0.250 \pm 0.055	0.261	0.257 \pm 0.093	0.266 \pm 0.047
K ₂ O	11.095	10.956 \pm 0.193	10.945 \pm 0.254	10.886	10.836 \pm 0.223	10.844 \pm 0.212
Total	95.533	95.489 \pm 0.290	95.450 \pm 0.735	95.311	95.339 \pm 0.295	95.202 \pm 0.814
Structural formula based on 11 oxygens and end-member calculation after Schliestedt (1986)						
Si	3.494	3.484 \pm 0.034	3.476 \pm 0.022	3.482	3.492 \pm 0.027	3.493 \pm 0.024
Al	0.506	0.516 \pm 0.034	0.524 \pm 0.022	0.518	0.508 \pm 0.027	0.507 \pm 0.024
Sites IV	4.000	4.000 \pm 0.000	4.000 \pm 0.000	4.000	4.000 \pm 0.000	4.000 \pm 0.000
Al	1.455	1.469 \pm 0.029	1.471 \pm 0.013	1.487	1.477 \pm 0.023	1.475 \pm 0.011
Ti	0.004	0.005 \pm 0.001	0.005 \pm 0.003	0.007	0.006 \pm 0.001	0.006 \pm 0.003
Cr	0.005	0.008 \pm 0.007	0.009 \pm 0.003	0.001	0.003 \pm 0.004	0.002 \pm 0.002
Mg	0.536	0.518 \pm 0.030	0.516 \pm 0.012	0.505	0.515 \pm 0.022	0.516 \pm 0.010
Fe ^{2+§}	0.000	0.000 \pm 0.000	0.000 \pm 0.000	0.000	0.000 \pm 0.000	0.001 \pm 0.003
Mn	0.000	0.000 \pm 0.000	0.000 \pm 0.000	0.000	0.000 \pm 0.000	0.000 \pm 0.000
Sites M2	2.000	2.000 \pm 0.000	2.000 \pm 0.000	2.000	2.000 \pm 0.000	2.000 \pm 0.000
Mg	0.020	0.017 \pm 0.007	0.019 \pm 0.011	0.015	0.011 \pm 0.007	0.011 \pm 0.008
Fe ^{2+§}	0.001	0.002 \pm 0.002	0.003 \pm 0.002	0.010	0.009 \pm 0.002	0.008 \pm 0.003
Mn	0.000	0.000 \pm 0.001	0.001 \pm 0.002	0.000	0.000 \pm 0.001	0.002 \pm 0.002
Site M1	0.021	0.019 \pm 0.007	0.023 \pm 0.011	0.024	0.020 \pm 0.007	0.020 \pm 0.011
Ca	0.012	0.017 \pm 0.005	0.018 \pm 0.004	0.008	0.016 \pm 0.006	0.015 \pm 0.004
Na	0.038	0.033 \pm 0.012	0.032 \pm 0.007	0.033	0.033 \pm 0.012	0.034 \pm 0.006
K	0.934	0.923 \pm 0.016	0.922 \pm 0.022	0.918	0.913 \pm 0.019	0.915 \pm 0.017
Site A	0.984	0.973 \pm 0.013	0.972 \pm 0.024	0.959	0.962 \pm 0.014	0.964 \pm 0.017
XMg	0.999	0.996 \pm 0.003	0.995 \pm 0.004	0.982	0.984 \pm 0.003	0.984 \pm 0.005
Tri	0.024	0.023 \pm 0.007	0.026 \pm 0.011	0.027	0.024 \pm 0.007	0.023 \pm 0.011
PrI	0.014	0.024 \pm 0.013	0.025 \pm 0.024	0.039	0.036 \pm 0.014	0.034 \pm 0.017
Mu	0.424	0.432 \pm 0.022	0.437 \pm 0.016	0.443	0.427 \pm 0.016	0.427 \pm 0.019
Cel	0.486	0.468 \pm 0.033	0.460 \pm 0.032	0.448	0.462 \pm 0.030	0.466 \pm 0.029
Pg	0.038	0.033 \pm 0.012	0.032 \pm 0.007	0.033	0.033 \pm 0.012	0.034 \pm 0.006
Mar	0.012	0.017 \pm 0.005	0.018 \pm 0.004	0.008	0.016 \pm 0.006	0.015 \pm 0.004
Total	0.998	0.997 \pm 0.001	0.997 \pm 0.001	0.998	0.998 \pm 0.001	0.998 \pm 0.001

[†] Analyses were generated using a relative uncorrelated standard deviation in oxide wt% of 1% for most oxides and of 2% for Al₂O₃, K₂O, Na₂O, following the method of Parra and Vidal (2002).

[†] Avg.: average analysis, Std.: standard deviation.

[§] All iron is considered as divalent.

Table A4.4 $^{40}\text{Ar}/^{39}\text{Ar}$ isotopic data for white mica, Syros, Greece

	Watts	^{40}Ar	$\pm 1\text{s}$	^{39}Ar	$\pm 1\text{s}$	^{38}Ar	$\pm 1\text{s}$	^{37}Ar	$\pm 1\text{s}$	^{36}Ar	$\pm 1\text{s}$	^{39}Ar Molt	$^{36}\text{Ar}/^{39}\text{Ar} \dagger\dagger$	$\pm 1\text{s}$	$\%(^{36}\text{Ar})/\text{Ca}$	$^{37}\text{Ar}/^{39}\text{Ar}$
SYB4 marble ($J: 1.971 \times 10^{-3} \pm 0.010$)																
A	0.25	101561.60	4885.79	7742.78	15.13	131.16	3.36	51.06	4.57	84.23	3.46	0.03	1086.95	44.76	0.2	0.0590
B	0.27	263828.40	4966.60	25648.26	51.62	339.20	4.92	54.73	4.24	37.82	2.22	0.09	147.33	8.66	0.4	0.0191
C*	0.30	484492.10	5051.84	39306.62	56.65	531.51	5.96	71.96	4.41	85.99	3.15	0.14	218.60	8.00	0.2	0.0164
D	0.45	167124.50	5787.72	11623.60	21.42	147.55	3.47	10.17	3.79	25.37	3.05	0.04	218.11	26.19	0.1	0.0078
E*	0.55	321279.70	3882.19	25387.08	28.97	2391.49	15.25	421.29	6.91	88.00	3.21	0.09	346.39	12.66	1.0	0.1290
F*	0.85	475754.50	3895.03	38974.44	27.72	507.64	6.35	137.77	4.55	52.13	3.84	0.14	133.66	9.85	0.6	0.0275
G	1.00	22097.65	3998.68	1952.79	7.76	39.40	3.51	13.43	4.33	7.00	2.97	0.01	358.45	151.84	0.4	0.0535
H*	6.00	142761.50	3936.54	11823.26	17.66	243.36	4.96	40.01	3.92	15.54	3.08	0.04	131.37	26.02	0.6	0.0263
SYB2/1 mylonite ($J: 1.967 \times 10^{-3} \pm 0.010$)																
A*	0.25	112386.70	3790.64	9239.68	18.91	142.46	3.75	0.46	4.07	39.57	3.76	0.03	427.96	40.69	0.0	0.0004
B*	0.27	192523.33	13491.39	165615.5	146.94	2177.45	25.50	47.92	17.14	97.11	11.85	0.58	58.59	7.15	0.1	0.0022
C*	0.30	163292.90	4025.69	14767.66	16.40	199.12	4.33	5.97	3.87	25.03	2.55	0.05	169.37	17.24	0.1	0.0031
D*	0.55	3321160	20972.84	258546.2	281.62	3696.59	32.02	79.09	22.00	986.40	20.97	0.91	381.24	8.11	0.0	0.0024
E*	0.85	89935.93	2973.16	7292.94	15.14	104.86	3.85	0.00	5.24	11.04	3.20	0.03	151.30	43.79	0.0	0.0000
F	1.00	235736.80	3940.48	19993.99	23.93	279.41	4.98	7.35	4.00	31.55	3.22	0.07	157.67	16.11	0.1	0.0029
G	6.00	66520.77	4200.40	5339.17	11.99	74.56	3.83	3.39	4.50	17.70	2.55	0.02	331.36	47.80	0.0	0.0050

* steps used to calculate Tp

† $\times 10^{-14}$, †† $\times 10^{-5}$

Table A4.4 continued

$\pm 1\text{s}$	Ca/K	$^{38}\text{Ar}/^{39}\text{Ar}$	$\pm 1\text{s}$	$^{40}\text{Ar}/^{39}\text{Ar}$	$\pm 1\text{s}$	$^{40}\text{Ar}/^{39}\text{Ar}$	$\pm 1\text{s}$	$\%^{40}\text{Ar}^*$	$^{39}\text{Ar} \%$	Age (Ma)	$\pm 1\text{s}$
0.0053	0.115569	0.010346	0.0169	0.00044	12.5641	0.0267	9.2994	0.135153	74.2	32.77	0.47
0.0015	0.037403	0.002902	0.0132	0.00019	9.8204	0.0205	9.3573	0.032567	95.5	32.98	0.11
0.0010	0.032103	0.001969	0.0135	0.00015	11.7972	0.0188	11.1212	0.029981	94.5	39.13	0.10
0.0029	0.015362	0.005729	0.0127	0.00030	10.5597	0.0203	9.8843	0.080562	93.8	34.82	0.28
0.0021	0.252875	0.004160	0.0941	0.00061	12.5376	0.0157	11.4954	0.04073	91.9	40.43	0.14
0.0009	0.053874	0.001780	0.0130	0.00016	12.1299	0.0099	11.7085	0.031076	96.7	41.17	0.11
0.0173	0.104821	0.033812	0.0202	0.00180	11.2616	0.0507	10.1718	0.455799	90.5	35.82	1.59
0.0026	0.051597	0.005052	0.0206	0.00042	11.8982	0.0191	11.4840	0.079932	96.7	40.39	0.28
0.0034	0.000755	0.006702	0.0154	0.00041	11.9504	0.0260	10.6480	0.123767	89.3	37.40	0.43
0.0008	0.004400	0.001573	0.0131	0.00015	10.6650	0.0110	10.4654	0.024072	98.4	36.76	0.08
0.0020	0.006161	0.003989	0.0135	0.00029	10.8725	0.0143	10.3423	0.053366	95.3	36.33	0.19
0.0007	0.004668	0.001298	0.0143	0.00012	12.1478	0.0151	10.9850	0.028097	90.6	38.57	0.10
0.0056	0.000000	0.010964	0.0144	0.00053	10.7682	0.0242	10.2911	0.132833	95.8	36.16	0.46
0.0016	0.005618	0.003057	0.0140	0.00025	11.7463	0.0163	11.2509	0.050699	96.0	39.49	0.18
0.0066	0.009720	0.012891	0.0140	0.00072	12.5459	0.0313	11.5322	0.145688	92.1	40.47	0.51

5. Synthesis

This Ph.D. thesis demonstrates how appropriate flanking structures in monomineralic rocks are as natural laboratories, giving great opportunity to study strain and strain-rate dependent deformation behaviour of a specific mineral, deformed at identical P-T conditions. It allows us to link observed microfabrics to particular strain rates. By comparison of these microstructures to experimental results, we can further on identify which deformation mechanisms are active. The consistency of theoretical and experimental determined calibrations can be tested down to nm scale. Nevertheless the observations in this thesis are only valid for marble deformed at lower greenschist facies conditions. Further work on rocks deformed at higher grade needs to be done to test the validity of calibrations at natural strain rates. In the following the key results of this thesis are listed:

- (1) The investigated flanking structure on Syros (Cyclades, Greece) developed during Miocene greenschist-facies metamorphism at deformation temperature of around 300 °C.
- (2) The observed marble mineral assemblage is stable over a wider range of P-T conditions and fluid compositions along the P-T path of Syros.
- (3) With increasing strain rate the dominant recrystallization mechanism in calcite changes from grain-boundary migration (GBM) to subgrain rotation (SGR) and bulging (BLG) recrystallization. While GBM and SGR have often been observed in experimentally deformed calcite rocks, BLG seems to be less common. This might be due to the lower achieved strain rates in the laboratory when compared to nature.
- (4) Variation in calcite textures with deformation strain rate indicates activation of different gliding systems.
- (5) The switch in recrystallization mechanism is accompanied by a decrease in grain size resulting in a switch in dominant deformation mechanism from grain size insensitive to grain size sensitive deformation mechanisms resulting in major strain softening.

(6) Grain boundary sliding supported by dislocation activity is an important strain localization mechanism in calcite marbles at low temperatures (300 °C) and high strain rates ($\sim 10^{-9} \text{ s}^{-1}$).

(7) Differential stresses calculated with the paleowattmeter (Austin and Evans, 2009) and paleopiezometer (Schmid, 1980) are consistent with the field boundary theory (De Bresser et al., 1998; 2001). The results lie in reliable range for calcite deformed at strain rates faster than 10^{-12} s^{-1} . Such high strain rates are somehow close to the ones used in laboratory experiments ($> 10^{-8} \text{ s}^{-1}$).

(8) The experimental calibration of De Bresser (1996) linking flow stress and dislocation density results in reliable values as of around 190 MPa, being almost identical with the calculated paleostresses (paleowattmeter, paleopiezometer).

(9) Laboratory determined flow laws of Renner et al. (2002) and Herwegh et al. (2003) are consistent with our microstructure observations regarding the activity of different creep regimes.

(10) The interconnected calcite matrix is at 300 °C weaker than white mica, accommodating most of the strain and inhibiting mica recrystallization. Therefore marble might not be ideal for resolving deformation ages.

.

References

- Austin, N., Evans, B., 2009.** The kinetics of microstructural evolution during deformation of calcite. *Journal of Geophysical Research* 114.
- Austin, N., Evans, B., Herwegh, M., Ebert, A., 2008.** Strain localization in the Morcles nappe (Helvetic Alps, Switzerland). *Swiss Journal of Geosciences* 101, 341-360.
- Ashby, M.F., Verrall, R.A., 1973.** Diffusion-accommodated flow and superplasticity. *Acta Metallurgica* 21, 149-163.
- Bachmann, F., Hielscher, R., Schaeben, H., 2010.** Texture Analysis with MTEX – Free and Open Source Software Toolbox. *Solid State Phenomena* 160, 63-68.
- Barber, D.J., Wenk, H.R., Gomez-Barreiro, J., Rybacki, E., Dresen, G., 2007.** Basal slip and texture development in calcite: new results from torsion experiments. *Physics and Chemistry of Minerals* 34, 73-84.
- Barnhoorn, A., Bystricky, M., Burlini, L., Kunze, K., 2004.** The role of recrystallisation on the deformation behaviour of calcite rocks: large strain torsion experiments on Carrara marble. *Journal of Structural Geology* 26, 885–903.
- Barnhoorn, A., Bystricky, M., Burlini, L., Kunze, K., 2005.** Post-deformational annealing of calcite rocks. *Tectonophysics* 403, 167–191.
- Bestmann, M., Prior, D.J., Grasemann, B., 2006.** Characterisation of deformation and flow mechanics around porphyroclasts in a calcite marble ultramylonite by means of EBSD analysis. *Tectonophysics* 413, 185-200.
- Bestmann, M., Prior, D.J., 2003.** Intragranular dynamic recrystallization in naturally deformed calcite marble: diffusion accommodated grain boundary sliding as a result of subgrain rotation recrystallization. *Journal of Structural Geology* 25, 1597-1613.
- Bestmann, M., Kunze, K., Matthews, A., 2000.** Evolution of a calcite marble shear zone complex on Thassos Island, Greece: microstructural and textural fabrics and their kinematic significance. *Journal of Structural Geology* 22, 1789-1807.

- Bobyarchick, A.R.**, 1986. The eigenvalues of steady flow in Mohr space. *Tectonophysics* 122, 35-51.
- Bons, P.D., den Brok, B.**, 2000. Crystallographic preferred orientation development by dissolution--precipitation creep. *Journal of Structural Geology* 22, 1713-1722.
- Bond, C.E., Butler, R.W.H., and Dixon, J.E.**, 2007. Co-axial horizontal stretching within extending orogens: the exhumation of HP rocks on Syros (Cyclades) revisited. *The Geological Society, London, Special Publications* 272, 203-222.
- Bonneau, M.**, 1984. Correlation of the Hellenide nappes in the south-east Aegean and their tectonic reconstruction. *The Geological Society, London, Special Publications* 17, 517-527.
- Bunge, H. J.**, 1982. *Texture Analysis in Materials Science: Mathematical Models*. Butterworths, London.
- Burkhard, M.**, 1990. Ductile deformation mechanisms in micritic limestones naturally deformed at low temperatures (150-350 °C). *Geological Society London. Special Publications* 54, 241-257.
- Burkhard, M.**, 1993. Calcite twins, their geometry, appearance and significance as stress-strain markers and indicators of tectonic regime: a review. *Journal of Structural Geology* 15, 351-368.
- Burlini, L., Bruhn, D.**, 2005. High-strain zones: laboratory perspectives on strain softening during ductile deformation. *Geological Society, London. Special Publications* 245, 1-24.
- Busch, J.P., Van Der Pluum, B.A.**, 1995. Calcite textures, microstructures and rheological properties of marble mylonites in the Bancroft shear zone, Ontario, Canada. *Journal of Structural Geology* 17, 677-688.
- Bröcker, M., Baldwin, S., Arkudas, R.**, 2013. The geological significance of $^{40}\text{Ar}/^{39}\text{Ar}$ and Rb-Sr white mica ages from Syros and Sifnos, Greece: a record of continuous (re)crystallization during exhumation? *Journal of Metamorphic Geology* 31, 629–646.

- Bröcker**, M., Bieling, D., Hacker, B., Gans, P., 2004. High-Si phengite records the time of greenschist facies overprinting: implications for models suggesting mega-detachments in the Aegean Sea. *Journal of Metamorphic Geology* 22, 427–442.
- Brun**, J.P., Cobbold, P.R., 1980. Shear heating and thermal softening in continental shear zones: a review. *Journal of Structural Geology* 2, 149-158.
- Byerlee**, J.D., 1978. Friction of rock. *Pure and Applied Geophysics* 116, 615-626.
- Cossette**, É., Schneider, D.A., Warren, C., and Grasemann, B., 2014. Lithological, rheological and fluid infiltration control on $^{40}\text{Ar}/^{39}\text{Ar}$ ages in polydeformed rocks from the West Cycladic Detachment System, Greece. *Journal of The Geological Society*, London, in press.
- De Bresser**, J. H. P., Evans, B., Renner, J., 2002. On estimating the strength of calcite rocks under natural conditions. *Deformation Mechanisms, Rheology and Tectonics: Current Status and Future Perspectives*. Geological Society, London. Special Publications 200, 309-329.
- De Bresser**, J. H. P., Ter Heege, J., Spiers, C., 2001. Grain size reduction by dynamic recrystallization: Can it result in major rheological weakening? *International Journal of Earth Sciences* 90, 28-45.
- De Bresser**, J.H.P., Peach, C.J., Reijs, J.P.J., Spiers, C.J., 1998. On dynamic recrystallization during solid state flow: Effects of stress and temperature. *Geophysical Research Letters* 25, 3457-3460.
- De Bresser**, J.H.P., Spiers, C.J., 1997. Strength characteristics of the r, f, and c slip systems in calcite. *Tectonophysics* 272, 1–23.
- De Bresser**, J.H.P., Spiers, C.J., 1990. High temperature deformation of calcite single crystals by r+ and f+ slip. *Deformation Mechanisms, Rheology and Tectonics*, Geological Society London Special Publications 54, 285-298.
- De Paor**, D.G., Means, W.D., 1984. Mohr circles of the First and Second Kind and their use to represent tensor operations. *Journal of Structural Geology* 6, 693-701.

Delle Piane, C., Wilson, C.J.L., Burlini, L., 2009. Dilatant plasticity in high-strain experiments on calcite–muscovite aggregates. *Journal of Structural Geology* 31, 1084–1099.

Dunlap, W.J., 1997. Neocrystallization or cooling? $^{40}\text{Ar}/^{39}\text{Ar}$ ages of white micas from low-grade mylonites. *Chemical Geology* 143, 181-203.

Dunlap, W.J., Kronenberg, A.K., 2001. Argon loss during deformation of micas: constraints from laboratory deformation experiments. *Contributions of Mineralogy and Petrology* 141, 174-185.

Etherdige, M.A., Wilkie, J.C., 1979. Grain size reduction, grain boundary sliding and flow strength of mylonites. *Tectonophysics* 58, 159-178.

Exner, U., Mancktelow, N.S., Grasemann, B., 2004. Progressive development of s-type flanking folds in simple shear. *Journal of Structural Geology* 26, 2191–2201.

Exner, U., Grasemann, B., 2010. Deformation bands in gravels: displacement gradients and heterogeneous strain. *Journal of the Geological Society* 167, 905-913.

Faulkner, D.R., Jackson, C.A.L., Lunn, R.J., Schlische, R.W., Shipton, Z.K., Wibberley, C.A.J., Withjack, M.O., 2010. A review of recent developments concerning the structure, mechanics and fluid flow properties of fault zones. *Journal of Structural Geology* 32, 1557-1575.

Fernández, F.J., Brown, D., Álvarez-Marrón, J., Prior, D.J., Pérez-Estaún, A., 2004. Microstructure and lattice preferred orientation of calcite mylonites at the base of the southern Urals accretionary prism. *Journal of the Geological Society* 161, 67-79.

Ferrill, D. a., Morris, A.P., Evans, M. a., Burkhard, M., Groshong, R.H., Onasch, C.M., 2004. Calcite twin morphology: a low-temperature deformation geothermometer. *Journal of Structural Geology* 26, 1521–1529.

Fliervoet, T. F., White, S. H., Drury, M. R., 1997. Evidence for dominant grain-boundary sliding deformation in greenschist- and amphibolite-grade polymineralic ultramylonites

from the Redbank Deformed Zone, Central Australia. *Journal of Structural Geology* 19, 1495-1520.

Gautier, P., Brun, J.P., Jolivet, L., 1993. Structure and kinematics of Upper Cenozoic extensional detachment on Naxos and Paros (Cyclades Islands, Greece). *Tectonics* 12, 1180-1194.

Gautier, P., Brun, J.P., 1994. Crustal-scale geometry and kinematics of late-orogenic extension in the central Aegean (Cyclades and Evia Island): *Tectonophysics* 238, 399-424.

Gifkins, R.C., 1976. Grain-boundary sliding and its accommodation during creep and superplasticity. *Metallurgical Transactions A* 7, 1225–1232.

Gifkins, R.C., 1978. Grain rearrangements during superplastic deformation. *Journal of Materials Science* 13, 1926-1936.

Goscombe, B.D., Passchier, C.W., Hand, M., 2004. Boudinage classification: end-member boudin types and modified boudin structures. *Journal of Structural Geology* 26, 739-763.

Goodwin, L.B., and Renne, P.R., 1991. Effects of progressive mylonitization on Ar retention in biotite from the Santa Rosa Mylonite Zone, California, and thermochronological implications: *Contributions to Mineralogy and Petrology* 108, 283-297.

Grasemann, B. and Tschegg, C., 2012. Localization of deformation triggered by chemo-mechanical feedback processes. *Geological Society of American Bulletin* 124, 737-745.

Grasemann, B., Exner, U., Tschegg, C., 2011. Displacement–length scaling of brittle faults in ductile shear. *Journal of Structural Geology* 33, 1650–1661.

Grasemann, B., Martel, S., Passchier, C., 2005. Reverse and normal drag along a fault. *Journal of Structural Geology* 27, 999–1010.

Grasemann, B., and Stüwe, K., 2001. The development of flanking folds during simple shear and their use as kinematic indicators. *Journal of Structural Geology* 23, 715-724.

Griggs, D., 1967. Hydrolytic Weakening of Quartz and Other Silicates*. *Geophysical Journal International* 14, 19-31

Halfpenny, A., Prior, D.J., Wheeler, J., 2012. Electron backscatter diffraction analysis to determine the mechanisms that operated during dynamic recrystallisation of quartz-rich rocks. *Journal of Structural Geology* 36, 2-15.

Hames, W.E., and Bowring, S.A., 1994. An empirical evaluation of the argon diffusion geometry in muscovite. *Earth and Planetary Science Letters* 108, 161-167.

Handy, M.R., 1990. The Solid-State Flow of Polymineralic Rocks. *Journal of Geophysical Research* 95, 8647-8661.

Harrison, T.M., Célérier, J., Aikman, A.B., Hermann, J., Heizler, M.T., 2009. Diffusion of ⁴⁰Ar in muscovite. *Geochimica et Cosmochimica Acta* 73, 1039–1051.

Hartmann, J., Moosdorf, N., 2012. The new global lithological map database GLiM: A representation of rock properties at the Earth surface. *Geochemistry, Geophysics, Geosystems* 13.

Hartz, E.H., Podladchikov, Y.Y., 2008. Toasting the jelly sandwich: The effect of shear heating on lithospheric geotherms and strength. *Geology* 36, 331-334.

Herwegh, M., Xiao, X., and Evans, B., 2003. The effect of dissolved magnesium on diffusion creep in calcite. *Earth and Planetary Science Letters* 212, 457-470.

Herwegh, M., Pfiffner, O.A., 2005. Tectono-metamorphic evolution of a nappe stack: A case study of the Swiss Alps. *Tectonophysics* 404, 55-76.

Hirth, G., Tullis, J., 1992. Dislocation creep regimes in quartz aggregates. *Journal of Structural Geology* 14, 145-159.

Holland, T.J.B., Powell, R., 1998. An internally-consistent thermodynamic dataset for phases of petrological interest. *Journal of Metamorphic Geology* 16, 309-344.

Ji, S., Jiang, Z., Rybacki, E., Wirth, R., Prior, D., Xia, B., 2004. Strain softening and microstructural evolution of anorthite aggregates and quartz-anorthite layered composites deformed in torsion. *Earth and Planetary Science Letters* 222, 377-390.

Jolivet, L., and Brun, J.P., 2010. Cenozoic geodynamic evolution of the Aegean. *International Journal of Earth Sciences* 99, 109-138.

- Jones**, M.E., 1975. Water weakening of quartz, and its application to natural rock deformation. *Journal of the Geological Society of London* 131, 429-432.
- Kaus**, B.J.P., Podladchikov, Y.Y., 2006. Initiation of localized shear zones in viscoplastic rocks. *Journal of Geophysical Research* 111.
- Kassner**, M.E., Hayes, T.A., 2003. Creep cavitation in metals. *International Journal of Plasticity* 19, 1715–1748.
- Keiter**, M., Piepjohn, K., Ballhaus, C., Lagos, M., Bode, M., 2004. Structural development of high-pressure metamorphic rocks on Syros island (Cyclades, Greece). *Journal of Structural Geology* 26, 1433–1445.
- Keiter**, M., Ballhaus, C., Tomaschek, F., 2011. A new geological map of the Island of Syros (Aegean Sea, Greece): Implications for lithostratigraphy and structural history of the Cycladic Blueschist Unit. *The Geological Society of America, Special Paper* 481.
- Kellet**, D., Joyce, N., 2014. Single- and multi-collection $^{40}\text{Ar}/^{39}\text{Ar}$ measurements for conventional step-heating and total fusion age calculation using the Nu Noblesse at the Geological Survey of Canada: analytical details. *Geological Survey of Canada Technical Note* (in press).
- Kenkmann**, T., Dresen, G., 1998. Stress gradients around porphyroclasts: palaeopiezometric estimates and numerical modelling. *Journal of Structural Geology* 20, 163-173.
- Kennedy**, L. a., White, J.C., 2001. Low-temperature recrystallization in calcite: Mechanisms and consequences. *Geology* 29, 1027.
- Kocher**, T., Mancktelow, N.S., 2005. Dynamic reverse modelling of flanking structures: a source of quantitative kinematic information. *Journal of Structural Geology* 27, 1346–1354.
- Kohlstedt**, D.L., Evans, B., Mackwell, S.J., 1995. Strength of the lithosphere: Constraints imposed by laboratory experiments. *Journal of Geophysical Research* 100, 587-602.

- Kohlstedt**, D.L., Weathers, M.S., 1980. Deformation induced microstructures, paleopiezometers and differential stresses in deeply eroded fault zones. *Journal of Geophysical Research* 85, 6269-6285.
- Kurz**, W., Neubauer, F., Unzog, W., Genser, J., Wang, X., 2000. Microstructural and textural development of calcite marbles during polyphase deformation of Penninic units within the Tauern Window (Eastern Alps). *Tectonophysics* 316, 327-342.
- Kramar**, N., Cosca, M.A., Hunziker, J.C., 2001. Heterogeneous ^{40}Ar * distributions in naturally deformed muscovite : in situ UV-laser ablation evidence for microstructurally controlled intragrain diffusion. *Earth and Planetary Science Letters* 192, 377–388.
- Liteanu**, E., Niemeijer, A., Spiers, C.J., Peach, C.J., de Bresser, J.H.P., 2012. The effect of CO_2 on creep of wet calcite aggregates. *Journal of Geophysical Research* 117, B03211.
- Llana-Fúnez**, S., Rutter, E.H., 2008. Strain localization in direct shear experiments on Solnhofen limestone at high temperature – Effects of transpression. *Journal of Structural Geology* 30, 1372–1382.
- Mackenzie**, J. K., Thompson, M. J., 1957. Some statistics associated with the random disorientation of cubes. *Biometrika* 44, 205-210.
- Mair**, K., Marone, C., 2000. Shear Heating in Granular Layers. *Pure and Applied Geophysics* 157, 1847-1866.
- McDougall**, I., Harrison, T.M., 1999. *Geochronology and Thermochronology by the $^{40}\text{Ar}/^{39}\text{Ar}$ Method*, 2nd ed.: Oxford University Press, New York, 288 p.
- Means**, W.D., 1995. Shear zones and rock history. *Tectonophysics* 247, 157–160.
- Menegon**, L., Stünitz, H., Nasipuri, P., Heilbronner, R., Svahnberg, H., 2013. Transition from fracturing to viscous flow in granulite facies perthitic feldspar (Lofoten, Norway). *Journal of Structural Geology* 48, 95–112.
- Molli**, G., White, J.C., Kennedy, L., Taini, V., 2011. Low-temperature deformation of limestone, Isola Palmaria, northern Apennine, Italy – The role of primary textures,

precursory veins and intracrystalline deformation in localization. *Journal of Structural Geology* 33, 255-270.

Oesterling, N., Heilbronner, R., Stünitz, H., Barnhoorn, A., Molli, G., 2007. Strain dependent variation of microstructure and texture in naturally deformed Carrara marble. *Journal of Structural Geology* 29, 681–696.

Olgaard, D. L., Evans, B., 1986. Effects of Second-Phase Particles on Grain Growth in Calcite. *Journal of the American Ceramic Society* 69, C-272-C-277.

Olgaard, D. L., Evans, B., 1988. Grain growth in synthetic marbles with added mica and water. *Contributions to Mineralogy and Petrology* 100, 246-260.

Papanikolaou, D.J., 1987. Tectonic evolution of the Cycladic Blueschist Belt (Aegean Sea, Greece). *H.C. Helgeson, Chemical Transport in Metasomatic Processes*, 429-450.

Passchier, C., 2001. Flanking structures. *Journal of Structural Geology* 23, 951–962.

Pennacchioni, G., Mancktelow, N.S., 2007. Nucleation and initial growth of a shear zone network within compositionally and structurally heterogeneous granitoids under amphibolite facies conditions. *Journal of Structural Geology* 29, 1757-1780.

Pennacchioni, G., 2005. Control of the geometry of precursor brittle structures on the type of ductile shear zones in the Adamello tonalities, Southern Alps, (Italy). *Journal of Structural Geology* 27, 627-644.

Pfiffner, O. A., Ramsay, J. G., 1982. Constraints on geological strain rates: arguments from finite strain rates of naturally deformed rocks. *Journal of Geophysical Research* 87, 311-321.

Philippon, M., Brun, J.P., Gueydan, F., 2011. Tectonics of the Syros blueschists (Cyclades, Greece): From subduction to Aegean extension. *Tectonics* 30, TC4001.

Philippon, M., Brun, J.P., Gueydan, F., 2012. Deciphering subduction from exhumation in the segmented Cycladic Blueschist Unit (Central Aegean, Greece). *Tectonophysics* 524-525, 116–134.

Pieri, M., Burlini, L., Kunze, K., Stretton, I., Olgaard, D.L., 2001. Rheological and microstructural evolution of Carrara marble with high shear strain: results from high temperature torsion experiments. *Journal of Structural Geology* 23, 1393–1413.

Platt, J.P., Behr, W.M., 2011. Grainsize evolution in ductile shear zones: Implications for strain localization and the strength of the lithosphere. *Journal of Structural Geology* 33, 537–550.

Raj, R., Ashby, M.F. 1971. On Grain Boundary Sliding and Diffusional Creep. *Metallurgical Transactions* 2, 1113-1127.

Ramsay, J.G., Huber, M.I., 1983. The Techniques of Modern Structural Geology. Volume 1: Strain Analysis. Academic Press, London.

Ratschbacher, L., Wenk, H.R., Sintubin, M., 1991. Calcite textures: examples from nappes with strain-path partitioning. *Journal of Structural Geology* 13, 369-384.

Reber, J.E., Dabrowski, M., Schmid, D.W., 2012. Sheath fold formation around slip surfaces. *Terra Nova* 24, 417–421.

Reches, Z., Eidelman, A., 1995. Drag along faults. *Tectonophysics* 247, 145-156.

Renner, J., Evans, B., and Siddiqi, G., 2002, Dislocation Creep of Calcite. *Journal of Geophysical Research* 107, ECV6-1-ECV6-16.

Ring, U., Glodny, J., Will, T., Thomson, S., 2010. The Hellenic Subduction System: High-Pressure Metamorphism, Exhumation, Normal Faulting, and Large-Scale Extension. *Annual Review of Earth and Planetary Sciences* 38, 45–76.

Ring, U., Thomson, S.N., Brcker, M., 2003. Fast extension but little exhumation: the Vari detachment in the Cyclades, Greece. *Geological Magazine* 140, 245–252.

Robertson, A.H., Dixon, J.E., 1984. Introduction: aspects of the geological evolution of the Eastern Mediterranean, in: Dixon, J.E., Robertson, A.H. (Eds.), *The Geological Evolution of the Eastern Mediterranean*. Geological Society, London, Special Publications, London, 1-74.

- Rogowitz, A.,** Grasemann, B., Huet, B., Habler, G., 2014. Strain rate dependent calcite microfabric evolution – An experiment carried out by nature. *Journal of Structural Geology* 69, Part A, 1–17.
- Romeo, I.,** Capote, R., Lunar, R., 2007. Crystallographic preferred orientations and microstructure of the Variscan marble mylonite in the Ossa-Morena Zone (SW Iberia). *Journal of Structural Geology* 29, 1353-1368.
- Rutter, E.H.,** Casey, M., Burlini, L., 1994. Preferred crystallographic orientation development during the plastic and superplastic flow of calcite rocks. *Journal of Structural Geology* 16, 1431–1446.
- Rutter, E.H.,** 1995. Experimental study of the influence of stress, temperature, strain on the dynamic recrystallization of Carrara marble. *Journal of Geophysical Research* 100, 24651-24663.
- Rybacki, E.,** Evans, B., Janssen, C., Wirth, R., Dresen, G., 2013. Influence of stress, temperature, and strain on calcite twins constrained by deformation experiments. *Tectonophysics* 601, 20-36.
- Rybacki, E.,** Wirth, R., Dresen, G., 2010. Superplasticity and ductile fracture of synthetic feldspar deformed to large strain. *Journal of Geophysical Research* 115.
- Sakai, T.,** Jonas, J.J., 1984. Overview no. 35 Dynamic recrystallization: Mechanical and microstructural considerations. *Acta Metallurgica* 32, 189–209.
- Schmid, S. M.,** Panozzo, R., Bauer, S., 1987. Simple shear experiments on calcite rocks: rheology and microfabric. *Journal of Structural Geology* 9, 747-778.
- Schmid, S. M.,** Paterson, M. S., Boland, J. N., 1980. High temperature flow and dynamic recrystallization in Carrara marble. *Tectonophysics* 65, 245-280
- Schmid, S.M.,** Boland, J.N., Paterson, M.S., 1977. Superplastic flow in fine grained limestone. *Tectonophysics* 43, 257-291.
- Schumacher, J.C.,** Brady, J.B., Cheney, J.T., Tonnsen, R.R., 2008. Glaucophane-bearing Marbles on Syros, Greece. *Journal of Petrology* 49, 1667–1686.

- Sibson, R.H.** 1977. Fault rocks and fault mechanisms. Geological Society, London 133, 191-213.
- Sibson, R.H.**, 2000. Fluid involvement in normal faulting. *Journal of Geodynamics* 29, 469-499.
- Sigoyer, J. De, Chavagnac, V., Blichert-toft, J., Villa, I.M., Luais, B., Cosca, M., Mascle, G., Géologie, I. De, Argand, E.**, 2000. Dating the Indian continental subduction and collisional thickening in the northwest Himalaya : Multichronology of the Tso Moriri eclogites. *Geology* 28, 487-490.
- Soukis, K., Stockli, D.F.**, 2013, Structural and thermochronometric evidence for multi-stage exhumation of southern Syros, Cycladic islands, Greece: *Tectonophysics* 595-596, 148-164.
- Spacek, P., Kalvoda, J, Francu, E., Melichar, R.**, 2001. Variation of deformation mechanisms within the progressive-retrogressive mylonitization cycle of limestones: Brunovistulian Sedimentary Cover (The Variscan Orogeny of the southeastern Bohemian Massif). *Geological Carpathica* 52, 263-275.
- Stipp, M., Stünitz, H., Heilbronner, R., Schmid, S. M.**, 2002. The eastern Tonale fault zone: a `natural laboratory` for crystal plastic deformation of quartz over a temperature range from 250 to 700 °C. *Journal of Structural Geology* 14, 1861-1884.
- Stipp, M., Kunze, K.**, 2008. Dynamic recrystallization near the brittle-plastic transition in naturally and experimentally deformed quartz aggregates. *Tectonophysics* 448, 77–97.
- Stünitz, H., Tullis, J.**, 2001. Weakening and strain localization produced by syn-deformational reaction of plagioclase. *International Journal of Earth Sciences* 90, 136-148.
- Sundberg, M., Cooper, R.F.**, 2008. Crystallographic preferred orientation produced by diffusional creep of harzburgite: Effects of chemical interactions among phases during plastic flow. *Journal of Geophysical Research: Solid Earth* 113, B12208.

- Ter Heege**, J.H., De Bresser, J.H.P., Spiers, C.J., 2004. Composite flow laws for crystalline materials with log-normally distributed grain size: theory and application to olivine. *Journal of Structural Geology* 26, 1693–1705.
- Thielmann**, M., Kaus, B.J.P., 2012. Shear heating induced lithospheric-scale localization: does it result in subduction. *Earth and Planetary Science Letters* 359, 1-13.
- Tomaschek**, F., Baumann, A., Villa, I.M., Kennedy, A., and Ballhaus, C., 2000. Geochronological constraints on a Cretaceous metamorphic event from the Vari Unit (Syros, Cyclades, Greece): Beihefte zum *European Journal of Mineralogy* 12, 214.
- Trotet**, F., Jolivet, L., Vidal, O., 2001a. Tectono-metamorphic evolution of Syros and Sifnos islands (Cyclades, Greece). *Tectonophysics* 338, 179-206.
- Trotet**, F., Vidal, O., Jolivet, L., 2001b. Exhumation of Syros and Sifnos metamorphic rocks (Cyclades , Greece). New constraints on the P-T paths. *European Journal of Mineralogy* 13, 901–920.
- Trullenque**, G., Kunze, K., Heilbronner, R., Stünitz, H., Schmid, S.M., 2006. Microfabrics of calcite ultramylonites as records of coaxial and non-coaxial deformation kinematics: Examples from the Rocher de l'Yret shear zone (Western Alps). *Tectonophysics* 424, 69–97.
- Tullis**, J., Yund, R.A., 1982. Grain growth kinematics of quartz and calcite aggregates. *Journal of Geology* 90, 301-318.
- Tullis**, J., Yund, R.A., 1985. Dynamic recrystallization of feldspar: a mechanism for ductile shear zone formation. *Geology* 13, 238-241.
- Ulrich**, S., Schulmann, K., Casey, M., 2002. Microstructural evolution and rheological behaviour of marbles deformed at different crustal levels. *Journal of Structural Geology* 24, 979-995.
- Van Der Pluum**, B.A., 1991. Marble mylonites in the Bancroft shear zone, Ontario, Canada: microstructures and deformation mechanisms. *Journal of Structural Geology* 13, 1125-1135.

- Vernon, R. H.**, 1981. Optical microstructure of partly recrystallized calcite in some naturally deformed marbles. *Tectonophysics* 18, 601-612.
- Wang, Z.**, Zhao, Y., Kohlstedt, D.L., 2010. Dislocation creep accommodated by grain boundary sliding in dunite. *Journal of Earth Science* 21, 541–554.
- Warren, C.J.**, Hanke, F., Kelley, S.P., 2012. When can muscovite $^{40}\text{Ar}/^{39}\text{Ar}$ dating constrain the timing of metamorphic exhumation? *Chemical Geology* 291, 79–86.
- Wheeler, J.**, Prior, D., Jiang, Z., Spiess, R., Trimby, P., 2001. The petrological significance of misorientations between grains. *Contributions to Mineralogy and Petrology* 141, 109–124.
- Wijbrans, J.R.**, McDougall, I., 1986. $^{40}\text{Ar}/^{39}\text{Ar}$ dating of white micas from an Alpine high-pressure metamorphic belt on Naxos (Greece): the resetting of the argon isotopic systems: *Contributions to Mineralogy and Petrology*, 93, 187-194.
- Wortel, M.J.R.**, Goes, S.D.B., Spakman, W., 1993. Structure and seismicity of the Aegean subduction zone: *Terra Nova* 2, 554-562.
- Yoo, M.H.**, Trinkaus, H., 1983. Crack and Cavity Nucleation at Interfaces during Creep. *Metallurgical Transactions* 14, 547-561.

Acknowledgments

I would like to thank my amazing supervisor Bernhard Grasemann who set up the idea for this project (together with Marcel Frehner...so thanks to him as well) and giving me the opportunity to create my own project out of it. I am thankful for his support and openness regarding all my ideas (even the silly ones), helpful discussions and teaching me how to work independently.

Great thanks to my second (even if not officially) supervisor Benjamin Huet for millions of hours of discussion, kicking my ass whenever I needed a kick, always having a beer for me and being the most encouraging person in the last three years. This work wouldn't have been half as much fun as it was if it wasn't for you. Thank you!

I would like to thank David Schneider for performing $^{40}\text{Ar}/^{39}\text{Ar}$ geochronology, teaching me how to pick mica in a fast (and easy) way and his help during my field work on Syros, Joseph White for helping me with the TEM analysis and being such a great host during my stay in Fredericton, Gerlinde Habler for hours of EBSD mapping, Sigrid Hrabe and Claudia Beybl for thin section preparation, Hugh Rice, Michel Bestmann, Claudia Trepmann and Luiz Morales for stimulating discussions and ideas.

I would also like to thank my wonderful colleagues! Especially Anne-Kathrin Schaeffer for helping me with all the computer stuff and keeping me various times from throwing it out of the window, Thomas Griffiths for lovely breakfasts on working-Sundays (so almost every Sunday for the last two years) and Marco Lommatzsch for 'fucking reality' with me.

Thanks to my family and friends for supporting me my whole life in every possible way! Especially thanks to Stefania Hapis, Marieke Rempe and Mirjam Nolz for nice (and lifesaving skype-) chats over the last three years...'aaaaaaaaahhhahahahahahah'...'lalalalalaaaaaa'... and for screaming with me when there was nothing else to say. Great thanks to my splendiferous sister Beate Khoury (still a Rogowitz in heart and her insane mind) for always being there for me!

This study was funded by the University of Vienna (Doctoral School IK052, grant number IK543002) and the Austrian Science Fund (grant number 1471-N19), as part of the research group FOR741-DACH.

To sum up (and in case I forgot someone...sorry you are probably included here)...

THANK YOU

...to everybody I told that I love him/her and/or proposed to in the last 3 years!

Curriculum Vitae

Personal details

Name	Anna Dominika Rogowitz
Date of birth	November 18, 1985
Birth place	Katowice, Poland
Nationality	German, Polish

Education

2011 – 2015	Ph.D. student at the Department for Geodynamics and Sedimentology, University of Vienna, Austria
2009 – 2011	Master of Science student at the Institute of Geology, Mineralogy and Geophysics, Ruhr Universität Bochum, Germany
2005 – 2009	Bachelor of Science student at the Institute of Geology, Mineralogy and Geophysics, Ruhr Universität Bochum, Germany
2005	Abitur (German), Helene-Lange Gymnasium, Dortmund, Germany

Working experience

2011 – 2011	Geologist in the consulting engineering office IMM Maidl & Maidl, Bochum, Germany
2010 – 2011	Assistant geologist in the consulting engineering office IMM Maidl & Maidl, Bochum, Germany
2007 – 2010	Undergraduate assistant in the sediment and isotope geology group at the Institute of Geology, Mineralogy and Geophysics, Ruhr Universität Bochum, Germany

Sometimes a little mystery is more comforting than knowing all the answers.

(The Moomins)

